Surface-Enhanced Raman Spectroscopy (SERS) for Intracellular pH Monitoring at Individual Single Cells

単一細胞内 pH 分析を指向した表面増強ラマン分光法

Qiang Zhang

Graduate School of Information Science and Technology,

Hokkaido University

Supervisor: Hiroshi Uji-i

Table of Contents

Acknowledgments

This doctoral research was carried out under the guidance of professor Hiroshi Uji-i at Hokkaido University in Japan.

First of all, I would like to express my greatest gratitude to professor Hiroshi Uji-i, my supervisor, for allowing me to study in the laboratory of Nanomaterials and Nanoscopy and providing me many helps in both academics and daily life. During the study period of the four years, his rigorous attitudes and meticulously logical thinking toward science have benefited me a lot, which will always have a positive effect on me throughout my whole life, I believe. Professor Hiroshi Uji-i provides a lot of help to my daily life and my family, which immensely helped us adapt here. Herein, I want to say “thank you very much” to my professor Hiroshi Uji-i.

I would like to express my gratitude to associate professor Kenji Hirai for the help in improving my skills not only for the experiments but also for the commutations. Many thanks to him for listening to me, encouraging me, and supporting me always.

I would like to express my gratitude to assistant professor Tomoko Inose for her help in both daily life and experiments. Many thanks for dealing with the admission procedure, renting the house, and measuring the experiments and so on for me.

I would like to express my gratitude to doctor Beatrice Fortuni and Monica Ricci for helping me with the writing and operation.

I would like to express my gratitude to professor Hitoshi Kasai, Susana Rocha, Eduard Fron, Akito Masuhara, Anh Thi Ngoc Dao, and Shuichi Toyouchi for helping me with the writing.

I would like to express my gratitude to my friend Akashi for the help. Many thanks to him for helping me through the tough time.

I would like to express my gratitude to Wen Han, Ya Tian, Jiangtao Li for the help with the measurements. Particular thanks to Wen Han for his help.

I would like to express my gratitude to Kiri, Shuhei, Shintaro, Ibuki, Takuto, Taku, Nakao, Haruka, and Guilin Feng for the great discussions about science and life.

I would like to express my gratitude to all of the professors who have taught me during the four years.

I would like to express my gratitude to the sensei in department office. I could feel they always try their best to help me.

I would like to express my gratitude to the China Scholarship Council (CSC) for the doctoral scholarship and help.

I would like to express my gratitude to Hokkaido University for letting me study here.

I would like to thank my family for their support and company. They always stand behind me and encourage me.

I would like to express my gratitude to all of the people who have ever helped me during these four years.

Thanks to everyone again.

Abstract

The protons play a critical role in bio-reactions in the highly compartmentalized cell which is a dynamic and heterogeneous system undergoing various metabolism. Valuable information of various cellular processes could be reflected through intracellular pH variation. For example, abnormal pH of the lysosomes is often involved in diseases. Furthermore, cancer cells feature a reversed pH gradient, namely intracellular alkalinization and extracellular acidosis. Therefore, studies on the variations of the intracellular pH are crucial for elucidating the interplay with cell functions, gaining insights into both pH-related pathological processes, and developing new therapeutic strategies.

Although several techniques have been proposed for intracellular pH measurements, among them, surface-enhanced Raman spectroscopy (SERS) has been attracted attention increasingly due to the following advantages: (a) no damage for the biological samples; (b) negligible disturbance from the fluorescence of biological matters and the Raman signal of water; (c) no quenching or photobleaching. However, tailored nanosensor highly sensitive for a specific pH range of a biological condition has not been reported. The apparent dissociation constant (pKa) of acid ligands is known to be sensitive to NP curvature. Thus, SERS pH sensitivity should be regulated by NP morphology. However, the dependence of SERS pH sensitivity on NP morphology has been overlooked. Moreover, these NP-based probes are trapped in the endo-lysosomal system, limiting the pH sensing to the inside of these acidic vesicles. And the delivery of the NP remains unspecific. Using SERS-active glass micropipettes or fiber tips have been proposed for pH sensing site-specifically. These techniques, although highly appealing, suffer from the large structure of the probe, which might cause drastic cell deformation and damage. What is more, the pH variations of the nucleus are poorly understood, although the nucleus is the target of most anticancer drugs. In the light of the foregoing, an alternative strategy is required in order to monitor the cytosolic and nuclear pH for a better understanding of the behavior of cells.

To address the first issue, namely developing a method to tailor the pH sensing probe sensitive for a targeted pH range, in this work (chapter 2), we investigated the coupling of the morphology of gold-coated silver nanoparticles to their sensitivity for pH sensing. We synthesized nearly spherical and flower-like silver nanoparticles and coated them with thin gold layers (AuAgNPs and AuAgNFs, respectively) to reduce the cytotoxicity of silver and

functionalized them with 4-mercaptobenzonic acid (4-MBA), which is the most commonly used probe molecule. We compared pKa behaviors of 4-MBA fixed on AuAgNPs and AuAgNFs and found that the 4-MBA fixed on AuAgNFs with higher curvatures gave a smaller apparent pKa (6.58) than that on AuAgNPs that have smaller curvatures (7.01). By carefully analyzing the SERS peak of COO^-, we found that anisotropic AuAgNFs could provide a more sensitive pH monitoring ability between 5 and 8 compared to nearly spherical AuAgNPs. This result indicated that SERS pH-sensitive range and sensitivity could be controlled by choosing nanoparticles with different curvatures. To exclude any incidence of potential NP toxicity on the pH-sensing results, cytotoxicity tests on human lung carcinoma cell line (A549) were also performed, showing that AuAgNFs possessed very low cytotoxicity compared with AgNFs. By taking advantage of this sensitivity, pH sensing inside endolysosomes was successfully performed in A549 with and without anticancer drug (cisplatin) treatment. In contrast, pH sensing inside endolysosomes performed with 4-MBA modified AuAgNPs in A549 with and without anticancer drug treatment showed large fluctuations, emphasizing the importance of the appropriate selection of the NP.

To address another issue, in this study (chapter 3), we propose an approach based on gold-deposited silver nanowires endoscopy for the study on the cytosolic and nuclear pH variations with high sensitivity. The sensing probe was fabricated by depositing gold nanostructures on silver nanowires (Au-dep-AgNW) via visible laser light induction to enhance the pH sensing sensitivity and modified the surface with 4-MBA. The pH sensing capability was tested by subjecting the probe to different pH solutions, and the related calibration curve gave a slope of 0.1 for the range of pH values between 5.5 and 7.4 approximately, while the calibration curve from our previously reported gold etched silver nanowires via galvanic replacement reaction (Au-etched-AgNW) gave a slope of 0.05, indicating dramatically improved sensitivity for pH sensing, most likely due to the enhanced curvature of the Au nanostructures deposited on the silver nanowire surface. The as-obtained probe was applied for site-specific sensing of the cytosolic and nuclear pH in living Hela cells, and the estimated pH values turned out to be stable over time with a value of ~ 7.3 both for cytosol and for the nucleus. The same experiments were performed on the hypoxia-mimetic agent $CoCl_2$. The trends of pH changes measured by Au-dep AgNW endoscopy are consistent with those monitored by pH-responsive fluorescence dyes. Notably, a large cytosol–nucleus pH gradient was observed in $CoCl_2$-treated cells over time, indicating that the presence of the drug affects nuclear pH regulation. These two intracellular measurements confirmed the excellent capability of the probe for pH sensing.

The probe was finally used to monitor the pH response of cells upon the anticancer drug cisplatin. Notably, a small cytosol–nucleus pH gradient was observed in cisplatin-treated cells over time, most likely due to the spoiling of the regulation of the nucleus. The potential of our endoscopy technique on the cytosolic and nuclear pH sensing over the conventional NP-based pH sensing was highlighted by the comparison with the AuAgNFs-based probe. The results reported clearly show that the Au-dep-AgNW endoscopy is a promising powerful tool for pH-sensing applications in biological systems.

Chapter 1

General Introduction

1.1 Introduction to the intracellular pH

The cell is the fundamental unit of organisms. A eukaryotic cell is composed of a cell membrane that separates the inner cell from the environment, cytoplasm, and membrane-bound nucleus, as shown in Figure 1.1.[1] The cytoplasm located in between the cell membrane and membrane-bound nucleus includes cytoplasmic matrix and organelles, in which organelles are usually isolated from the surrounding cytoplasmic matrix by a membrane, forming a highly compartmentalized structure. Compartmentalization could provide optimal environmental conditions for the metabolism of the cells.[2] Indeed, the intracellular pH varies largely among these different compartments. The intracellular pH plays a very important role in the context, which is involved in the physiological condition of cells and could provide information about various cell processes, such as cell growth, proliferation, cytoskeleton polymerization, enzyme activity, apoptosis, drug resistance and so on.[2-10] Considering the importance of the lysosomal, cytosolic and nuclear pH, in this introduction, we will focus on these three parts.

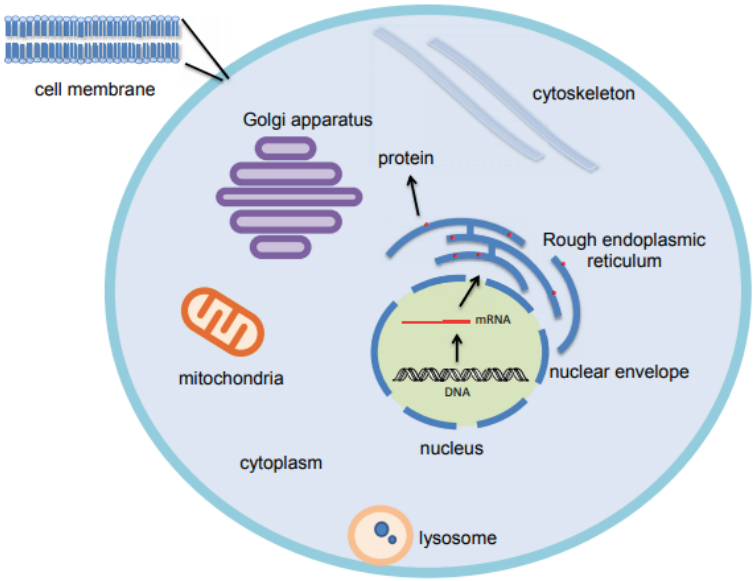

Figure 1.1. The eukaryotic cell. [adapted from[1]]

The pH of the lysosomes

Lysosome was first discovered by centrifugation in 1955 from rat liver cells in the laboratory of Christian de Duve in Louvain.[11] Lysosome is an acidic organelle with a buffering capacity

of 19 ± 6 mM / pH unit covered by a monolayer membrane, containing a variety of enzymes.[12] The vacuolar-type H^+-ATPase located on the membrane is mainly responsible for pumping protons in to maintain the acidic condition.[13-16] Vacuolar-type H^+-ATPase is composed of two domains: integral membrane V_0 domain toward the lysosome and V_1 domain exposed to the cytosol.[13] The structure of the vacuolar-type H^+-ATPase is shown in Figure 1.2. V_0 is composed of six different types of subunits, transporting protons across the membrane by means of formation of the proton translocation pore; V_1, composed of eight subunit types, is responsible for the hydrolysis of adenosine triphosphate (ATP) to gain the energy for proton displacement.[13] These two domains work cooperatively to transport protons into the lysosome for maintaining the acidic environment in order to activate a variety of enzymes to digest and degrade the unwanted substances, including the extracellular material transported into the cell and the metabolic waste in the cell.[13-16] Therefore, the lysosome is viewed as the waste processing center of the cell. Moreover, lysosomes are considered to play key roles in cellular homeostasis, immune functions, nutrient sensing, energy metabolism, as well as autophagy.[12, 17] To exert lysosome functions properly, the lysosomal pH of cells needs to be tightly regulated.[17, 18] A dysregulated lysosomal pH has increasingly shown that it is related to disease, such as neurodegeneration, cancer and so on.

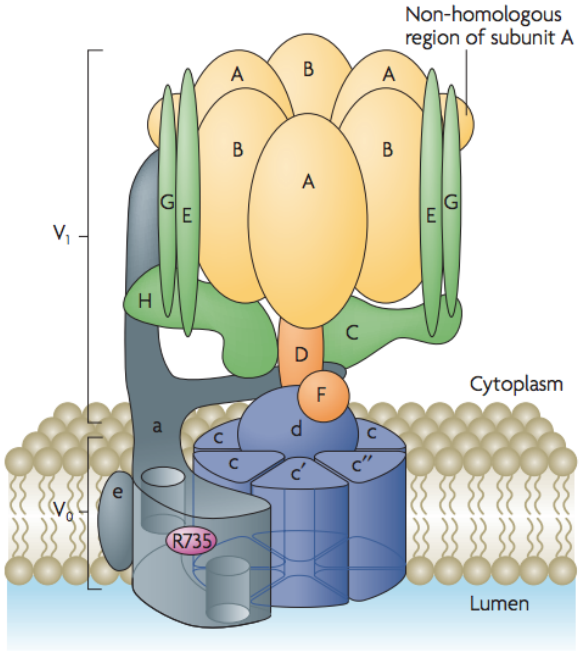

Figure 1.2. Structure of the vacuolar-type H^+-ATPase. [adapted from[13]]

An elevated pH value, for instance, has been found in Alzheimer's disease which is a neurodegenerative disease. The amyloid-β-containing plaques and neurofibrillary tangles (NFTs) formed by the hyperphosphorylated microtubule-associated protein tau are the hallmarks of Alzheimer disease.[19] The pathogenesis of Alzheimer disease still remains unclear. However, increasing studies show the disordered lysosomal pH may be involved in Alzheimer's disease.[20-22] Amyloid-β is transported into lysosome or autolysosome for degradation.[23] However, the disability to degrade the autophagic cargo in lysosomes cause a large number of accumulations of autophagic cargoes, most likely due to the disordered lysosomal pH. The defective lysosomal acidification might be due to the mutation of presenilin 1 which acts as a chaperone essential for vacuolar-type H^+-ATPase or thioesterase deficiency by reducing the proton transport capability of vacuolar-type H^+-ATPase.[24, 25] In contrast, adequate acidification of the lysosome might enable the autolysosome to degrade amyloid-β through the autophagic pathway. It is reported that inactivated microglia that possess weakly acidic lysosomes with averaged pH of 6 could not degrade amyloid-β while the ones that were treated with macrophage colony-stimulating factor (MCSF) or interleukin-6 which can acidify the lysosomes to a pH of 5 was able to degrade amyloid-β, revealing that lysosomal pH might be a key factor for degradation of amyloid-β.[26] All of these findings reveal that the disordered lysosomal pH is involved in neurodegeneration.

For another example, decreased lysosomal pH is observed in cancer. The dramatically increased glucose uptake in most cancer cells are converted into lactic acid in the cytoplasm due to the unique energy-yielding pathway of cancer cells, glycolysis, leading to a large number of protons generated in the cytoplasm of cancer cells.[27, 28] As a result, the protons are intensively pumped out of cells by increasing the expression or activity of plasma membrane ion transporters to avoid the harmfulness originated from the acidification.[29] Besides, lysosomes are viewed to contribute to remove the protons in the cytoplasm in the following two ways.[30] Firstly, the expression and activity of the vacuolar-type H^+-ATPase located on the lysosomal membrane are increased, which might lead to the formation of the more acidic lysosomes. Secondly, the volume of the lysosomes is enlarged, which increases the proton storage capability of lysosomes. These two enhancements greatly increase the capacity to store protons, thus maintaining the cytosolic pH in cancer cells to help cancer cells survive. Accordingly, the lysosome-autophagy pathway is enhanced, which has been increasingly considered to play a critical role in the progression of cancers, contributing to surviving in microenvironmental stress and growth.[12, 31] Based on the characteristics of cancer cells in terms of pH, on the one

hand, some chemicals such as hydroxychloroquine have been exploited to increase lysosomal pH in cancer, resulting in effectively suppressing cancer progression.[32] On the other hand, many drug delivery systems have been proposed to use pH-sensitive materials.[33] In summary, the pH of the lysosome plays a certain role in cancer.

Cytosolic pH

Many important intracellular processes, such as glycolysis, and protein synthesis, take place in the cytosol. Among these reactions, enzymes have an important role. Actually, the structure and activity of the enzymes could be strongly influenced by pH.[34] For instance, the cytosolic enzymes are considered to optimally exert their function at near pH 7.3.[35] In fact, cytosolic pH has been recognized as a factor to regulate cellular physiology and signaling.[36] Accordingly, it is strictly controlled. Since the cytosol is prone to acidify mainly due to the electrical potential across the membrane and the various metabolic reactions generating acids, the protons have to be transported outside the cytosol in order to maintain the cytosolic pH suitable for intracellular reactions.[2] The exchangers or co-transporters play an important role in this process, such as alkali cation–H^+ exchangers, lactate–H^+ co-transporters, bicarbonate transporters, and acid-loading transporters and so on.[2] The Na^+ / H^+ exchanger isoform 1 (NHE1) is considered to mainly regulate the cytosolic pH for pH homeostasis.[37] NHE1, a glycoprotein consisted of 815 amino acids, includes two domains.[38, 39] Figure 1.3 shows the structure model of NHE1.[40] The first domain is the three consensus N-glycosylation sites within the membrane domain within the first 500 residues, which is responsible for the electroneutral exchange of one intracellular proton for one extracellular sodium ion.[38, 40] The second domain within the left 315 residues is the cytoplasmic tail which is responsible for the regulation of the membrane domain.[38, 40] The presence of these exchangers and co-transporters together with organelles guarantees the pH homeostasis in the cytosol for various intracellular processes.

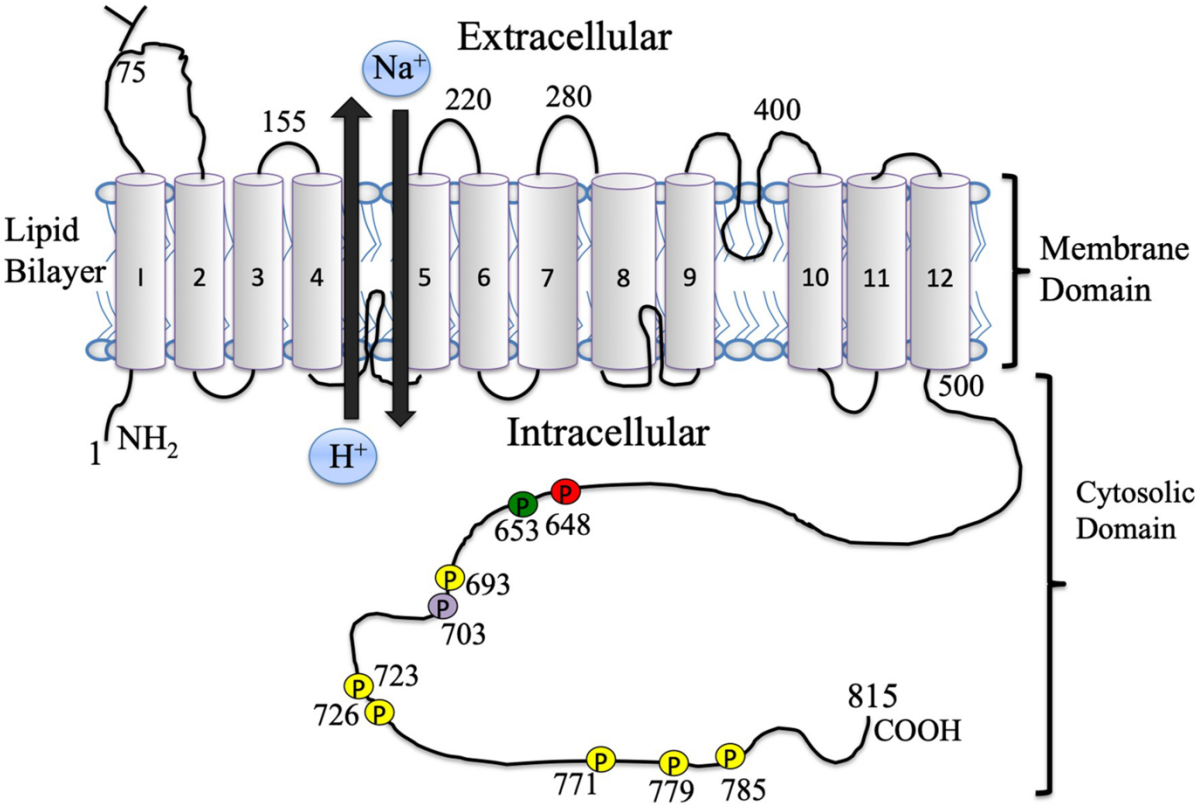

Figure 1.3. Illustration of the general structure of NHE1. [adapted from[40]]

On the other hand, disordered cytosolic pH is increasingly recognized to be involved in pathological cell behaviors. Figure 1.4 illustrates the difference in pH between healthy cells and cancer cells.[41] Cancer cell usually has more high cytosolic pH than the healthy cell, which is most likely due to a hypoxic environment in which cancer cells are considered to grow.[41, 42] In such a situation, the metabolism of the cancer cell is reprogramed to sustain ATP through the anaerobic g glycolysis to support the growth of cancer cells.[43, 44] Compared with that one glucose molecule is converted into 36 ATP by oxidative phosphorylation, that one glucose molecule is only converted into 2 ATP by anaerobic glycolysis is not enough to support the growth of cancer cells.[45] Thereby, the dramatically increased glucose uptake rate in most cancer cells is necessary to obtain the energy for the proliferation of cancer, which leads to the production of plenty of lactic acid in the cytosol.[27] To avoid the tendency of acidification, the intensively pumping H^+ out of cells by increasing the expression or activity of plasma membrane ion transporters results in the more alkaline cytosolic pH.[29, 46] The dysregulated cytosolic pH of cancer cells benefits cellular processes, such as cell proliferation, migration as

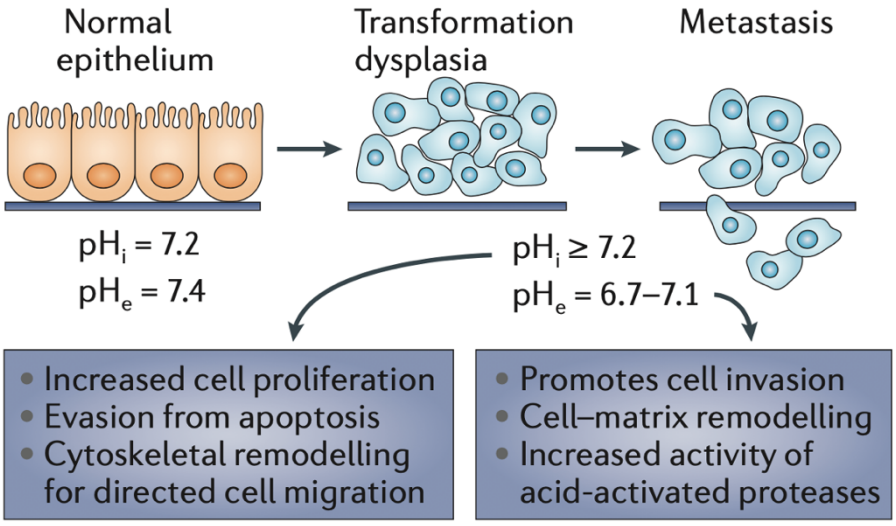

Figure 1.4. Cancer cells have a reversed pH gradient compared with normal differentiated adult cells, higher intracellular pH and a lower extracellular pH, which facilitates the indicated adaptive behaviors. [adapted from[41]]

well as apoptosis. It has shown that the increased cytosolic pH has been recognized to specifically program an E2F-dependent transcription and promotes cyclin D1 expression to enhance proliferation of cells, revealing that the increased cytosolic pH is a critical signal to regulate G1 progression.[3] In addition, the increased cytosolic pH has been identified to contribute to remodeling actin filaments and cell-substrate adhesions, contributing to cell migration.[28] What is more, increased cytosolic pH has also been found to contribute to preventing DNA degradation in HL-60 cells treated with lovastatin, blocking apoptotic signal by the inactivating endonuclease.[47] Conversely, cytosolic acidification has been observed during the mitochondria triggered apoptosis of cells. The decreased cytosolic pH might be the critical factor to activate cytosolic caspases which are necessary to execute the programmed death, since the optimized pH to activate caspases by cytochrome c is viewed to be in acidic pH.[48] In addition, regulating the cellular pH has been proposed as a therapeutic strategy. Decreasing the cytosolic pH has been found to effectively suppress the migration of cells.[49]

The nuclear pH

The nucleus is the administrative and information center of a cell, containing the gene, in which the replication of DNA and transcription occur. Enzymes are involved in these events to speed up these reactions. In addition, some anti-cancer drugs interact with DNA to exert their functions, such as cisplatin, doxorubicin.[50, 51] In the context, as aforementioned, the nuclear pH should have effects on them. Although the nucleus has a decisive effect on the behavior of the cell, by far, the information about the nuclear pH regulation is unclear. Among the limited publications, two contrary viewpoints could be summarized. In the first point of view, the nuclear pH is viewed to be equal to that of the cytosol because of the existence of the abundance of pores of the nuclear envelope that should be permeable to H^+.[2] Indeed, some experiment results revealed the nuclear pH is equal to that of cytosol, which supports this idea.[52] However, a different viewpoint has been come up with, in which they found that the nuclear pH is not equal to that of cytosol.[53, 54] To have a clear understanding, more studies on the nuclear pH are required to clarify it.

Overall, the cellular pH is involved in pathological cell behaviors, as discussed above. Study on cellular pH variation, therefore, will be of great importance not only for gaining the feedback of ongoing events and fully understanding the coupling of cell behaviors to pH,[6, 35] but also for developing new therapeutic strategies and drug delivery systems.

1.2 Introduction to Surface-Enhanced Raman Spectroscopy (SERS)

1.2.1 SERS

When a light (electromagnetic field) interacts with a molecule, a small part of the light is scattered. In these scattering, if the wavelength (frequency) of light does not change before and after scattering, it is elastic scattering (Rayleigh scattering). If the wavelength of light changes before and after scattering, it is inelastic scattering (Raman scattering). The Raman scattering was theoretically proposed by Smekal in 1923, and it was discovered experimentally by Raman and Krishnan in 1928.[55, 56] The Raman scattering is divided into two situations:

Stokes scattering: when the frequency of the scattered light is smaller than the incident light, the scattered light is called Stokes scattering. In the Stokes scattering, the molecule gets the energy from the photon. Therefore, the molecule ends up in a higher vibrational energy state.

Anti-Stokes scattering: the scattered light with a higher frequency than the incident light is called anti-Stokes scattering. In the anti-Stokes scattering, the energy of the molecule is transferred to the photon. Therefore, for the anti-Stokes scattering, the molecule should be in an excited vibrational state at the beginning and end up in a lower vibrational energy state (the ground state).

Raman scattering can be explained by the classical theory using the polarizability of a molecule.[57, 58] When a molecule interacts with the light, its electron cloud is disturbed by the electric field (E), which results in the separation of electrons and nuclei. Consequently, an induced electric dipole moment (μ) forms in the molecule, which characterizes the Raman scattering. Then the induces a dipole moment μ could be expressed as the following equation:

$$\mu = \alpha E \tag{1.1}$$

Here, α is the polarizability of the molecule, which is the tendency to distort the charge distribution of the molecule by an external electric field E. The molecular polarizability α is a function of the instantaneous position of the constituent atoms, and it could be expressed as:

$$\alpha = \alpha_0 + (q - q_e)\frac{\partial \alpha}{\partial q} \tag{1.2}$$

Here, α_0 is the polarizability of the molecule at the equilibrium position; q is bond lengths at any instant position; q_e is bond lengths at the equilibrium position. Assuming that the molecule is in simple harmonic motion, the $q - q_e$ could be expressed as:

$$q - q_e = q_{max} \cos 2\pi\nu_{vib} t \quad 1.3$$

Here, q_{max} is the maximum separation distance between atoms relative to their equilibrium position; ν_{vib} is the vibrational frequency of a molecule. Therefore, equation 1.2 could be written as:

$$\alpha = \alpha_0 + q_{max} \cos 2\pi\nu_{vib} t \frac{\partial_\alpha}{\partial_q} \quad 1.4$$

Accordingly, equation 1.1 could be written as:

$$\mu = E(\alpha_0 + q_{max} \cos 2\pi\nu_{vib} t \frac{\partial_\alpha}{\partial_q}) \quad 1.5$$

If the frequency of the electromagnetic wave is ν, the electric field could be expressed as:

$$E = E_0 \cos 2\pi\nu t \quad 1.6$$

Here E_0 is the amplitude of the electromagnetic wave. Therefore, equation 1.5 could be expressed as:

$$\mu = E_0 \cos 2\pi\nu t \, (\alpha_0 + q_{max} \cos 2\pi\nu_{vib} t \frac{\partial_\alpha}{\partial_q}) \quad 1.7$$

Then the equation 1.7 could be further deduced as:

$$\mu = \alpha_0 E_0 \cos 2\pi\nu t + q_{max} \cos 2\pi\nu_{vib} t \frac{\partial_\alpha}{\partial_q} E_0 \cos 2\pi\nu t \quad 1.8$$

The final equation could be presented as:

$$\mu = \alpha_0 E_0 \cos 2\pi\nu t + q_{max} \frac{E_0}{2} \cos[2\pi(\nu - \nu_{vib})t] \frac{\partial_\alpha}{\partial_q} + q_{max} \frac{E_0}{2} \cos[2\pi(\nu + \nu_{vib})t] \frac{\partial_\alpha}{\partial_q} \quad 1.9$$

Thus, it can be seen that equation 1.9 is consisted of three terms, which are corresponding to Rayleigh scattering with the frequency ν, the Stokes scattering with the frequency $\nu - \nu_{vib}$ and

the anti-Stokes scattering with the frequency $\nu + \nu_{vib}$. The Raman-active molecules must have variational polarizability during a vibration. And the Raman scattering is regulated by the frequency of the vibration.

Raman scattering also can be explained by quantum mechanics.[57,59] The scattering process can be understood as following. Figure 1.5 illustrates the Raman scattering with the Jablonski Diagram.[59] The electron of vibrational level of the electronic ground state in the molecule absorbs the energy and excited to a virtual state of energy, followed by falling back to the same vibrational level of the electronic ground state V_0, emitting a photon of equal energy to that of the incident photon, which is referred to as Rayleigh scattering. If the electron falls back to the excited vibrational level of the electronic ground state V_1, emitting a photon of less energy than that of the incident photon, which is referred to as Stokes scattering. If the molecule is in an excited vibrational level of the electronic ground state V_1, the electron of excited vibrational level of the electronic ground state in the molecule absorbs the photon and excited to a virtual state of energy, followed by falling back to the vibrational level of the electronic ground state V_0, emitting a photon with higher energy to that of the incident photon, which is referred to as anti-Stokes scattering. Since most molecules are in the ground state at room temperature,[60] the probability of occurrence of anti-Stokes scattering is much lower than that of Stokes scattering. Thus, in terms of Raman measurement, it generally refers to Stokes scattering.

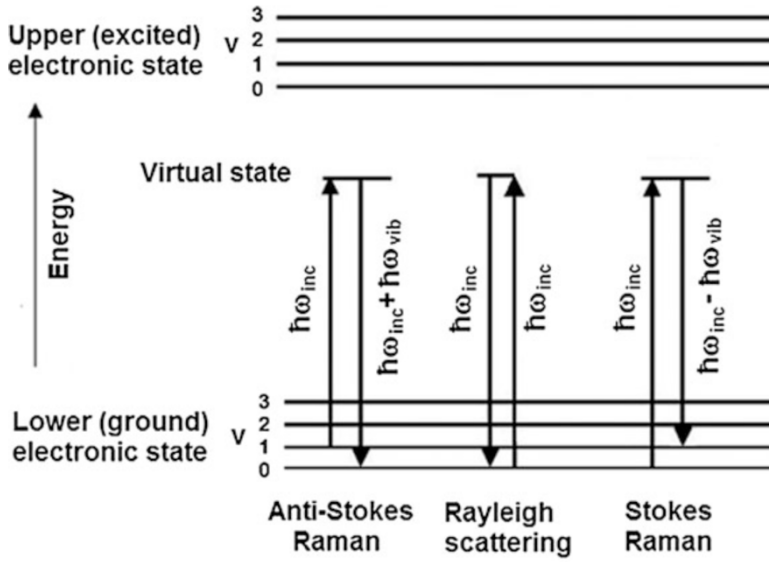

Figure 1.5. The Jablonski diagram to illustrate the Raman scattering. [adapted from[59]]

In Raman scattering, the change of the frequency of light is only related to the vibrational modes of the electronic ground state of a molecule. Thus, each molecule has a unique Raman spectrum. Namely, the Raman spectrum of a molecule could be the molecular fingerprint. Therefore, Raman spectroscopy could be used as a spectroscopic method to precisely analyze the structure of a molecule. In addition to offering the specific molecular fingerprint information, the Raman scattering technique has some advantages, including non-invasive measurement, simple preparation of the sample, ability to measure biological samples and ability to simultaneously detect different analytes and so on.[61, 62] Although being awfully fascinating, the Raman scattering is inherently weak, limiting its further applications.

To overcome this issue, Surface-enhanced Raman spectroscopy (SERS) has been developed to enhance the Raman scattering, combining the aforementioned advantages of Raman scattering with high sensitivity, providing dramatically enhanced intensity of Raman signal. SERS was first discovered from a pyridine-modified rough silver electrode in 1974 by Fleischmann et al.[63] Afterward, the enhancement was confirmed independently by Jeanmaire et al. and by Albrechtand et al. in 1977.[64, 65] Since then, SERS has been extensively studied. By far, it has been sensitive enough to observe a monolayer species on the metal surface, and even single molecules, due to the enormous enhancement.[66] To characterize the SERS enhancement, the SERS enhancement factor (EF) is introduced. The SERS EF is the ratio of signal intensity of a given molecule under SERS and normal Raman scattering, which can be quantificationally estimated with the equation as following:[67]

$$\mathrm{EF} = \frac{(I_{SERS}/N_{SERS})}{(I_{RS}/N_{RS})} \qquad 1.10$$

Here, I_{SERS} is the SERS intensity of the molecules adsorbed on the metal surface; I_{RS} is the normal Raman intensity of molecules; N_{SERS} is the number of molecules in the scattering volume for I_{SERS}; N_{RS} is the number of molecules in the scattering volume for I_{RS}. The enhancement factors even could be up to $10^{14} - 10^{15}$.[68] Although the exact mechanism of the SERS effect is still in the controversy, Raman scattering could be enhanced by either the electromagnetic field E or the molecular polarizability α according to equation 1.1, accordingly, which are corresponding to two commonly accepted mechanisms for the enhancement of SERS: electromagnetic enhancement and chemical enhancement.[59]

1.2.2 Mechanisms of SERS

1.2.2.1 Electromagnetic mechanism

The electromagnetic enhancement is mainly due to the amplification of the electromagnetic field in the vicinity of the surface of the metallic nanostructure, resulting from the excitation of surface plasmon resonance (SPR).[69] SPR refers to the collective oscillations of the conduction electrons at the surface of the nanostructure, including propagating surface plasmon polaritons (SPPs) and localized SPR (LSPR).[70, 71] Figure 1.6 schematically illustrates the surface plasmon polariton and the localized surface plasmon.[72] SPPs are the propagating wave for the order of micrometers, occurring when light is trapped at the interface between a metal and a dielectric.[71,73] When the light interacts with NPs which are much smaller than the incident wavelength, and the frequency of the excitation light matches the frequency of the localized surface plasmon, the LSPR occurs, which could be well modulated by the size, shape, and composition of nanostructure and the surrounding dielectric medium.[70,74] The LSPR contribute to a great enhancement of the localized electromagnetic field, underlying enhancement of SERS effect.[75] The enhancement is approximatively proportional to the fourth power of the strength of the local electromagnetic field.

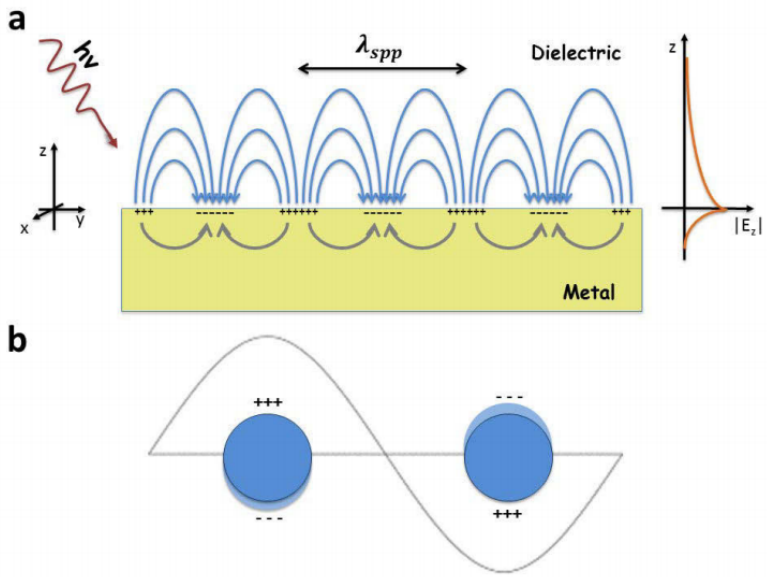

Figure 1.6. Schematic diagrams illustrating a surface plasmon polariton (a) and a localized surface plasmon (b). [adapted from[72]]

The electromagnetic enhancement could be viewed as two distinct processes:[76]

The local field enhancement. The excitation of SPR generates a large amplification of the electromagnetic field in small spatial regions. Accordingly, the molecules in such regions are exposed to the greatly enhanced electromagnetic field.

The radiation enhancement. Since the power radiated by the Raman-active molecule relies on the surrounding environment, the presence of the metallic nanostructure could have an effect on the process.

1.2.2.2 Chemical Mechanism

The chemical mechanism is another way to enhance the Raman scattering by changing molecular polarizability α, in which the photoinduced charge transfer between the molecule and the substrate is usually involved.[59] The transfer of the electrons is from the substrate to the molecule or vice versa under the excitation wavelength, which requires that the Fermi level of the metal substrate should be located in between the ground state of the molecule and the excited state of the molecule.[77] These two models of charge transfer processes are illustrated in Figure 1.7.[78] More specifically,[78, 79] the left one stands for the charge transfer from the ground state of the molecule I to the Fermi state of the metal substrate F. The charge transfer intensity is obtained by μ_{IF} through borrowing intensity from the allowed transition μ_{IK}. The Fermi state of the metal substrate F is coupled with the excited molecular states K through vibronic coupling h_{FK}. The right part stands for the charge transfer from the Fermi state of the metal substrate F to the excited state of molecule I. The charge transfer intensity obtains its intensity via μ_{FK} through borrowing intensity from the allowed transition μ_{IK}. The ground molecular state I is coupled with the Fermi state of the metal substrate F through vibronic coupling h_{IF}. Notably, this chemical mechanism has been wildly exploited in the studies of nonmetal-based enhanced Raman scatting, such as semiconductor, graphene, and metal-organic framework.

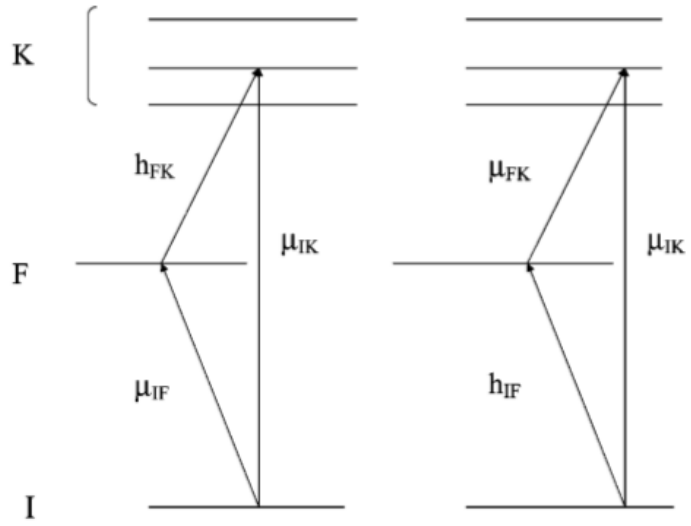

Figure 1.7. Schematic energy level diagram of the metal–molecule system for the charge-transfer processes. Here, I stands for the ground state of the molecule; K represents the excited state of the molecule; M represents the Fermi state of the metal substrate. [adapted from[78]]

Titanium Dioxide. Titanium Dioxide is a semiconductor material, which was used as a SERS-active substrate for successfully sensing 4-mercaptobenzoic acid (4-MBA), 4-mercaptopyridine (4-MPy), and 4-aminothiophenol (4-ATP).[80] In the Titanium Dioxide – based SERS measurement, the surface plasmon resonant frequency of the titanium dioxide NPs is far from the excitation wavelength of the laser (514.5 nm) used in the study. Therefore, the electromagnetic enhancement could be ruled out for the SERS effect. In addition, the non-totally symmetric modes of b2 were enhanced, which were observed in the spectrum. Therefore, the chemical mechanism was mainly contributed to the enhanced Raman signal for these molecules fixed on the titanium dioxide nanoparticles, rather than the electromagnetic mechanism. Figure 1.8 illustrates the process of the charge transfer between the adsorbed molecule and titanium dioxide.[80] Since the energy of the excitation laser (2.4 eV) is insufficient to excite the electron of the valence band (VB) to transfer to the conduction band (CB) for either titanium dioxide NPs (Figure 1.8 a) or molecules (Figure 1.8 b). Therefore, the electron of VB in titanium dioxide NPs was most likely transferred to the CB of the target molecules. (Figure 1.8 c) They also found that the order of the enhancement of these molecules was: 4-MBA > 4-MPy > 4-ATP, which were in very good agreement with the attracting electron ability of groups para- to the mercapto group on the benzene ring. Later the titanium dioxide

enhanced Raman scattering involved in charge transfer was also observed by other groups.[81, 82] However, the Raman enhancement by titanium dioxide is not high.

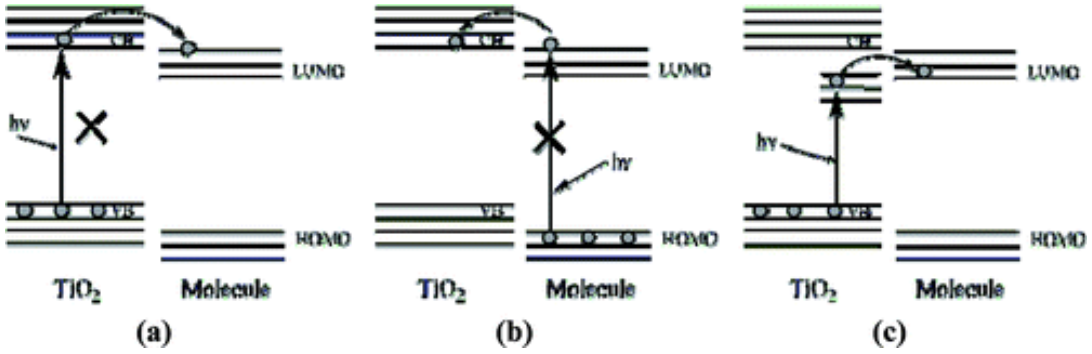

Figure 1.8. Modes of the charge transfer between the adsorbed molecule and titanium dioxide. [adapted from[80]]

Graphene. Graphene is a two-dimensional material of a honeycomb-like crystalline structure composed of a monolayer of sp2 bonded carbon atoms, possessing many unique merits, such as unique electron and photon structures, ultrahigh carrier mobility, excellent mechanical property, atomic uniformity, biological compatibility and so on.[83-86] Taking the advantages, graphene has been employed in many research fields. Especially, graphene has been employed as a substrate of enhanced Raman scattering to enhance Raman signal, namely graphene-enhanced Raman scattering.[86] The enhancement might mainly be benefited from two contributions, being able to effectively eliminate the fluorescence background of fluorescent dyes and enhancing the Raman scattering by means of the charge transfer between graphene and various molecules, likely due to the enrichment of the molecules via p–p interactions.[87] Zhang et al. reported that graphene was able to effectively suppress the fluorescence background of fluorescent dyes adsorbed on graphenes, such as rhodamine 6G (R6G) and protoporphyrin IX (PPP), through quenching the photoluminescence in the measurement of resonance Raman spectra.[88] A schematic illustration of graphene as a substrate to quench the fluorescence of R6G is shown in Figure 1.9a. The Raman spectrum of R6G with the excitation of 514 nm laser in Figure 1.9b (blue line) showed a strong fluorescence background. While the Raman spectrum of R6G adsorbed on graphene showed a weaker fluorescence background, resulting in the clear Raman peaks in Figure 1.9b (red line). They later systematically investigated the graphene-enhanced Raman scattering of several dyes deposited on graphenes, such as phthalocyanine (Pc), R6G, PPP, and crystal violet (CV)[89]. The enhancement depends on the structure of the material, and among monolayer, few-layer, multilayer graphene,

graphite, and highly ordered pyrolytic graphite, the most remarkable enhancement of the Raman signals were observed with monolayer graphene, which is attributed to the charge transfer between graphene and the molecules.[89] However, pure graphene substrate has weak enhancement.

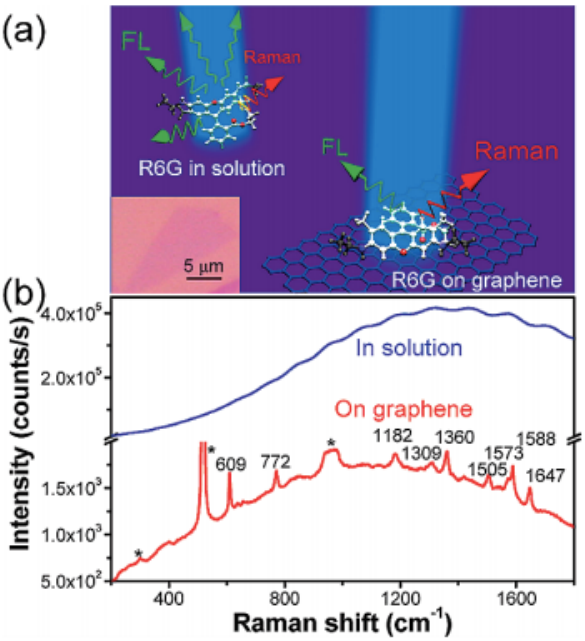

Figure 1.9. Schematic illustration of graphene as a substrate to quench the fluorescence of R6G in RRS (a). Raman- fluorescence spectra of R6G in water (10 μM) (blue line) and R6G on a 1L graphene (red line) at 514 nm excitation (b). [adapted from[88]]

Metal-organic frameworks (MOFs). MOFs are an emerging class of porous materials, possessing a great number of pores (90% free volume) and huge surface areas (beyond 8000 m^2 / g), which are composed of metal ions or clusters and organic linkers.[90, 91] The bottom-up synthesis method is commonly used to synthesize MOFs, including slow diffusion, hydrothermal (solvothermal), electrochemical, mechanochemical, microwave method, and ultrasound method.[92, 93] Zn(II), Cu(II), Fe(III), and Zr(IV) are commonly used as metal ions in MOFs.[94] The molecules with polydentate structures are often used as organic linkers, such as carboxylate, imidazolate, phosphonate, and hydroxy and so on.[95] The physical and chemical properties of MOFs could be regulated by judicious choice of the metal ions and organic linkers.[96] Due to the structural and functional tunability, MOFs have been widely studied for gas sorption, catalysis, separation, drug delivery, biological imaging, and biochemical sensing.[97] In particular, the MOFs could be a promising SERS substrate to enhance the SERS

signals through charge-transfer interactions between the MOFs SERS substrate and the molecules.[98-101] Szetsen Lee et al. reported that the enhanced Raman scattering of methyl orange (MO) was observed using MOFs (MIL series) as substrate without metal nanomaterials or enhancing agents.[98] The absorption peaks of ultraviolet-visible spectra of the MO, MOFs, and MO–MOFs complexes were far from the excitation wavelength of the laser in this study. After ruling out the effect of conventional resonance enhancement, they attributed the observed SERS effect to the charge transfer mechanism between the MOFs and the adsorbed MO molecules and verified this assumption using Density functional theory (DFT). Zhigang Zhao et al. reported that MOFs, as a SERS substrate, can highly enhance the Raman scattering of the target molecules with molecular selectivity.[99] Systemically comparing Cobalt-Based and Tetrakis(4-carboxyphenyl)porphyrin (TCPP)-based MOFs, they found that the EF for ZIF-67 could go as high as 1.9×10^{6} by purposively manipulating the electronic band structures of MOF-based SERS substrate to match the target analytes. As shown in Figure 1.10, 10^{-8} M of R6G on both the raw ZIF-67 and acid-treated ZIF-67 substrates shoed the clear SERS signals under the excitation of 532 nm laser.[99] The SERS effect has also been observed for MOFs on their own in different studies.[100, 101]

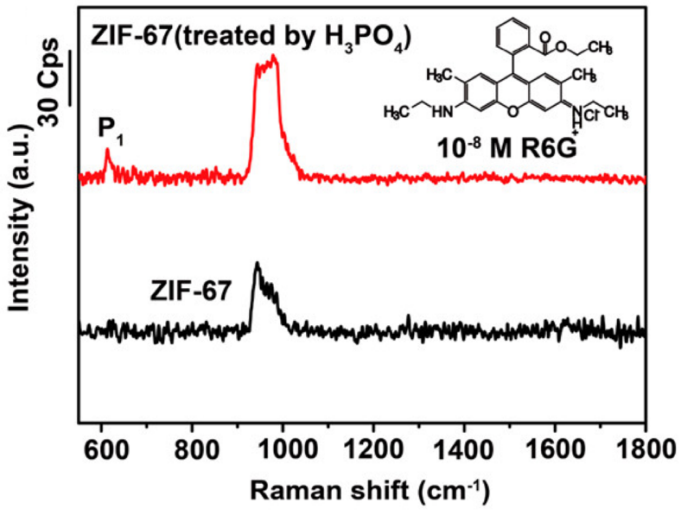

Figure 1.10. SERS spectra of R6G (10^{-8}M) on the raw ZIF-67 and acid-treated ZIF-67 substrates when excited by 532 nm laser. [adapted[99]]

1.2.3 SERS substrates (silver and gold substrates)

1.2.3.1 Silver nanoparticles

The great enhancements of the Raman signals, as aforementioned, are mainly considered to be due to the electromagnetic enhancement of the SERS substrates through LSPR, such as silver-based and gold-based substrates.[102] These SERS substrates could be fabricated by either a top-down approach or a bottom-up method.[103, 104] Thought top-down approach, such as atomic layer deposition and electron-beam lithography, highly controlled substrates are easily obtained.[105, 106] However, it is high-cost and time-consuming.[107] In contrast, the bottom-up method is commonly preferable, among which wet-chemical synthesis is the normal approach.[107]

More specifically, synthesis of the silver nanostructures by wet-chemical synthesis based on the reduction of the silver ions in a solution using reducing agents, such as, hydrazine, sodium borohydride, citrate, hydroxylamine, ascorbic acid and hydrochloride and so on, in the presence of capping molecules such as polyethylene glycol (PEG), citric acid, sodium citrate, hydroxylamine hydrochloride and polyvinylpyrrolidone (PVP) and so on, which are responsible for keeping the stability of the silver nanostructures by either repulsive or steric forces, is composed of two phases, a nucleation phase, and growth phase.[108-113] Silver atoms combine together to form the nuclei first, namely the nucleation phase, following by the growth of the crystal nuclei to generate the silver NPs during the growth phase.[114-116] The size and shape of the silver nanostructures can be regulated by controlling the experimental conditions during the synthesis.[111, 117] For instance, the 31 nm of quasi-spherical silver NPs were synthesized by using ascorbic acid as reductant at pH 10.5, while 73 nm of the silver NPs could be obtained by reducing the pH to 6.0.[118] The shape of the silver nanoparticle can be controlled by selection of the surfactants. The surfactant could bind to the specific crystal planes, thus, leading to orientated growth of the nanoparticles, such as nanocubes[119], nanospheres[120], nanotriangles[121], nanowires[122], nanoplates[123], and nanoflowers[112] and so on. Figure 1.11 shows the scanning electron microscope (SEM) / transmission electron microscope (TEM) images of these silver nanoparticles.

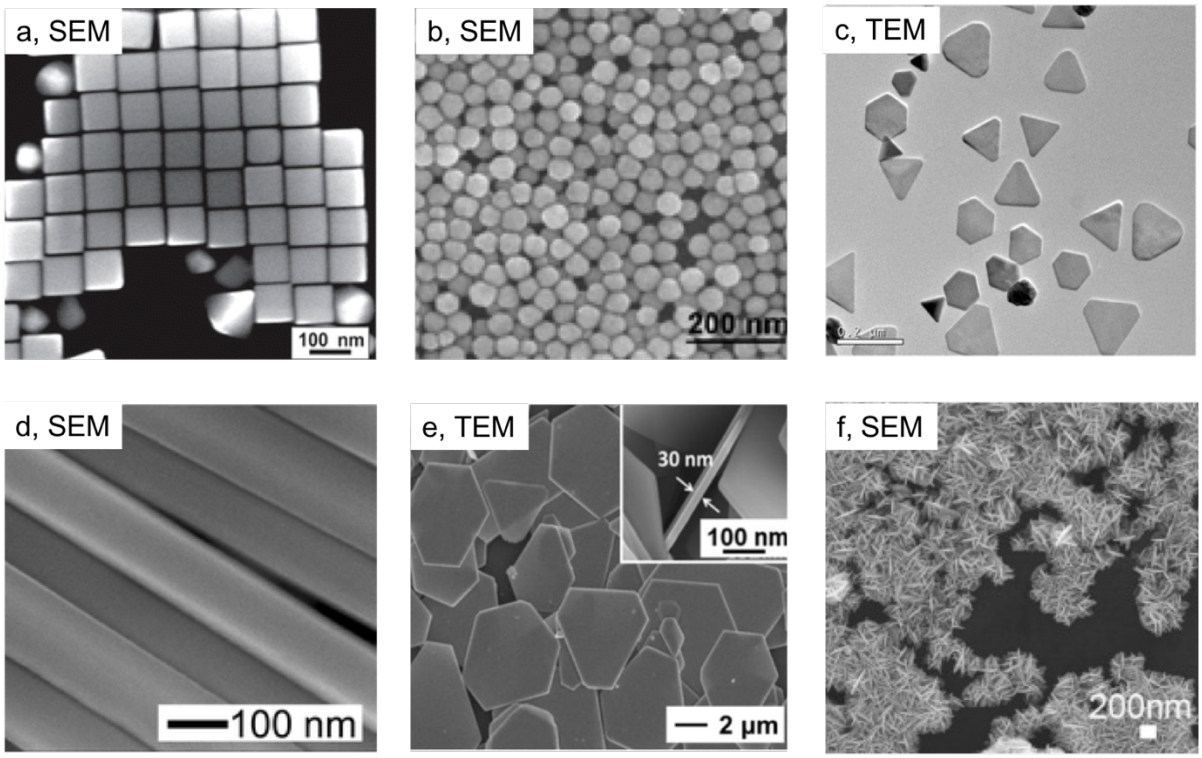

Figure 1.11. SEM / TEM images of different shapes of silver nanoparticles. Nanocubes (a), nanospheres (b), nanotriangles (c), nanowires (d), nanoplates (e), and nanoflowers (f). [adapted from[112, 119-123]]

The size and shape of the silver nanostructures have an effect on its SERS enhancement. If NPs are too small, the electrical conductivity will reduce due to the dominating of the electronic scattering processes at the surface, which could lead to poor polarizability, thus resulting in degrading the SERS enhancement.[124, 125] With the increase of the size of the nanoparticles, the SERS enhancement increases due to the increase of the number of electrons excited.[126] If the nanoparticle size is up to the scale of the excitation wavelength, the NPs will be mainly excited in nonradiative modes, diminishing the SERS enhancement.[110] The shape of the NPs could also greatly affect the distribution of the electromagnetic field, resulting in area-related SERS enhancement. A strong electromagnetic field usually occurs at the edge and corners of nanoparticles.[127] Figure 1.12 illustrates this phenomenon that strong electromagnetic fields could be observed at the edges and corners of silver nanoparticles.[128] The LSPR peak wavelength could be regulated by controlling the size and shape of the silver nanostructure. The spectrum of LSPR can be experimentally obtained from the extinction spectrum. For spherical nanoparticles, the LSPR peak wavelength could be theoretically predicted based on the Mie theory, which is given as following:[129-131]

$$\sigma = 24\pi r^3 \frac{{\varepsilon_m}^{3/2}}{\lambda} \frac{\varepsilon_2}{(\varepsilon_1+2\varepsilon_m)^2+{\varepsilon_2}^2} \quad 1.11$$

Here, λ is the wavelength of the extinction radiation, ε_m is the dielectric constant of the medium, and ε_1 and $\varepsilon_2$respectively are the real and imaginary parts of the dielectric function of the metal nanoparticles.

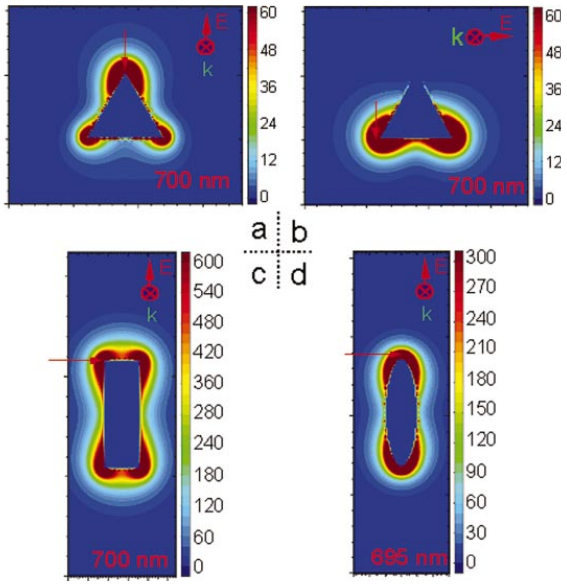

Figure 1.12. Local electric field enhancement on single silver nanoparticles with different shapes. (a) and (b) are the electric field enhancement contours external to a triangular prism polarized along the two different primary symmetry axes, (c) and (d) are the electric fields enhancement contours for a rod and spheroid polarized along their long axes. The arrows show where is the maximum electric field. [adapted from[128]]

From equation 1.11, it can be known that the dielectric function of the metal NPs plays a role in LSPR. The real part of the dielectric function determines the amount of polarization of the nanomaterial subjected to an electric field.[132] The imaginary part determines the optical losses, including inter-band and intra-band losses, such as plasmon damping.[133] As shown in Figure 1.13,[133] the real part and imaginary part of the dielectric function for silver and gold change differently with the wavelength. Although a difference could be found for the real part of the dielectric function for silver and gold, a significant distinction is found for the imaginary part in which silver has a smaller imaginary part of the dielectric function. Accordingly, silver has a stronger SERS enhancement effect among noble metal substrates.[134] Due to the excellent SERS enhancement, silver substrates have been widely used to improve Raman enhancement

signals. However, the SERS enhancement effect of silver substrates is easily impaired due to oxidation.[135] And the toxicity of silver to cells restricts the bio-applicability of silver nanoparticles.

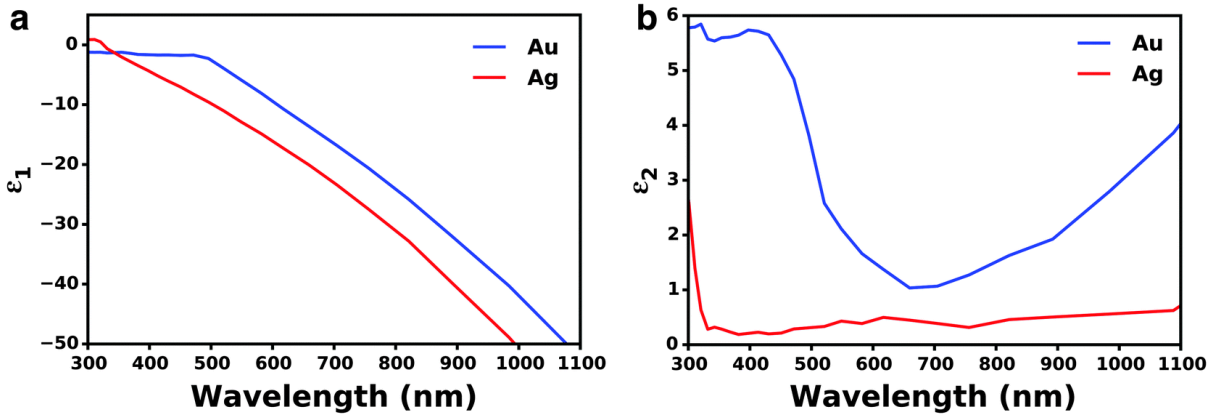

Figure 1.13. The real part of the dielectric function for Au and Ag (a). The imaginary part of the dielectric function of Au and Ag (b). [adapted from[133]]

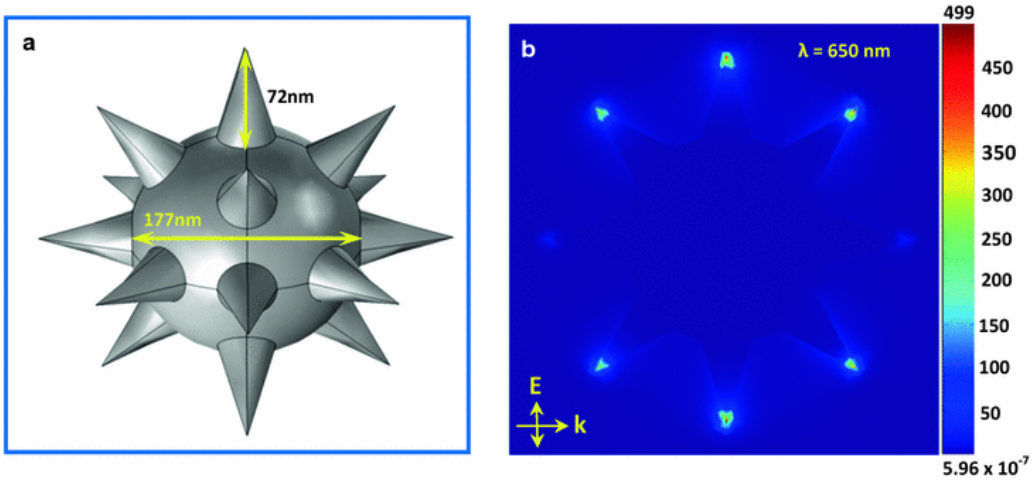

Figure 1.14. 3D modeling of a nanostar having 18 spikes, in COMSOL software (a). Electric field enhancement on the surface of a gold nanostar illuminated with the plane wave of wavelength 650 nm (b). [adapted from[136]]

1.2.3.2 Gold nanoparticles

Gold nanomaterials have been widely used in chemistry, biology, and medicine due to their excellent physicochemical properties, such as their large surface area which can be modified

with molecules, high resistance to oxidation, and non-toxicity.[137] Gold substrates could be obtained by reducing the gold ions in a solution by the reducing agents, such as, sodium borohydride, citrate, with the capping agents including sodium citrate, cetrimonium bromide (CTAB).[138, 139] Different shapes, such as nanorods,[140] nanocubes,[141] nanotriangles,[142] and nanoflowers[143] and so on, could be obtained by proper selection of the capping agents and the reducing agents. Same as silver, the size and shape of the gold nanomaterials could affect the LSPR. Figure 1.14 shows that the stronger electric field enhancement is mainly located at the edges.[136] Due to the large value of the imaginary parts of the dielectric function of the gold in the shorter wavelength, as shown in Figure 1.13, optical losses in gold are high. Consequently, gold nanomaterials are used as SERS substrates often under the excitation of 633 nm or 785 nm laser. Although the SERS enhancement of the gold is low than that of silver,[144] chemical stability and the biocompatibility of gold NPs are significantly higher than that of silver nanoparticles. Coating the silver nanomaterials with a thin gold layer would be a good way to combine the high SERS enhancement with excellent chemical stability and biocompatibility.[135, 145] As shown in Figure 1.15,[145] both the AgNPs and Ag@Au core-shell substrate shows a high SERS enhancement and a relatively homogeneous SERS mapping. However, after being left in the air for one week, a huge background and a heterogeneous mapping were observed for AgNPs. In contrast, no significant alteration in either the SERS spectra or the mapping was observed for Ag@Au, indicating oxidation resistance.

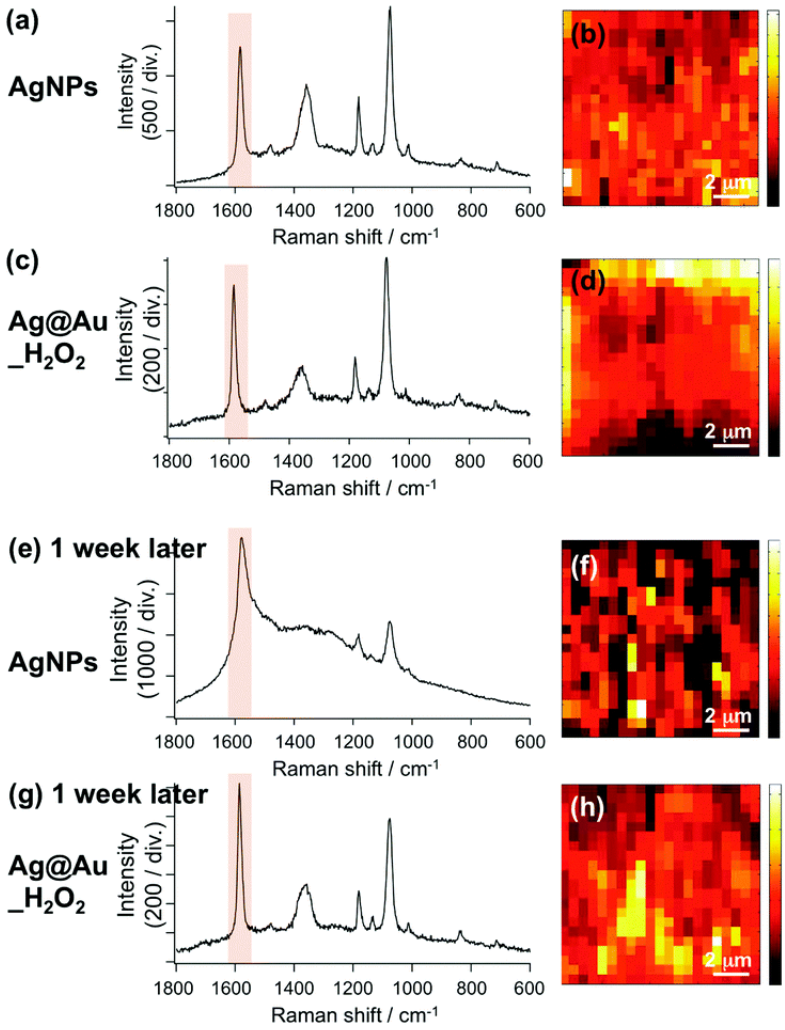

Figure 1.15. 4-MBA SERS spectra and mapping images measured on fresh and one week-old samples; freshly-prepared AgNPs (a and b) and AgNP@Au-shell_H_2O_2 (c and d), and one week-old AgNPs (e and f) and AgNP@Au-shell_H_2O_2 (g and h). The peak at 1590 cm^{-1} was used for the mapping. [adapted from[144]]

1.2.4 SERS bio-applications

SERS has been widely used in many fields, including biology, physics, chemistry, biomedical monitoring, food science and materials science.[61, 146-148] When it comes to bioanalysis, it is particularly advantageous due to the following reason: (a) molecular specificity; (b) ultrahigh sensitivity; (c) selectable excitation wavelengths; (d) high resolution; (e) multiplex detection capability; (f) noninvasion; (g) weak Raman signal of water; (h) negligible interference from autofluorescence of biological systems; (i) freedom from quenching or photobleaching; (j) customizable SERS substrates for various detection purpose.[149-152] As a result, SERS has been used to detect the biomolecules and drugs in living cells, the biomarker of cancers, and to monitor the intracellular environment.[152-155] For instance, Figure 1.16 shows that SERS endoscopy to investigate cells.[156] In this study, the silver nanowires-based SERS probe was inserted into Hela cells for site-specific detection. As shown in Figure 1.16c, this technique is able to interrogate the nucleus, which shows the great potential for cell study.

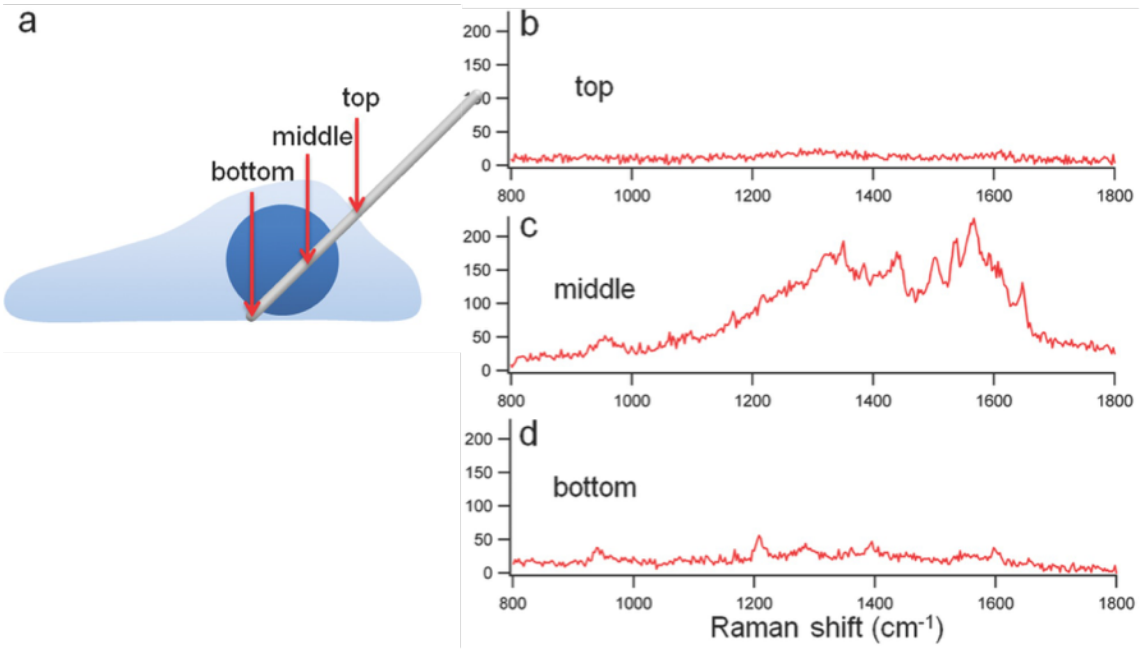

Figure 1.16. SERS endoscopy for cell study. Scheme of the positions chosen for direct excitation SERS spectroscopy inside a live HeLa cell during AgNW probe endoscopy (a). Raman spectra taken from hotspots at the top (b), middle (c) and bottom (d) parts of the AgNW probe corresponding to regions in the HBSS buffer, the cell nucleus, and the cell cytoplasm, respectively. [adapted from[156]]

In particular, intracellular pH is one of the most important regulating factors in the physiological activities of cells. Monitoring the intracellular pH would be essential for the profoundly understanding of many physiological and metabolic processes.[151] To the end, many efforts have been made on the development of the SERS-based pH sensing probes for sensing intracellular pH. The basic principle is to use pH-sensitive molecules whose Raman spectrum varies in different pH environments.

Talley and co-workers are the pioneer who functionalized silver NPs with pH-sensitive molecule 4-MBA, as a pH nanosensor, to sense local intracellular pH in 2004.[157] The spectra of the 4-MBA fixed on silver NPs showed obvious changes in the intensity of the COO^- stretch mode at around 1400 cm^{-1} in different pH environments as shown in Figure 1.17, thus, the local pH in the microenvironment could be monitored. The pH surrounding the nanoparticle after endocytosis calculated from the SERS spectra was below 6. The authors attributed this to being located inside a lysosome. This study demonstrated that the SERS technique could be used for intracellular pH sensing. To understand the maturation pathway of the endosome, the dynamic pH changes in the endolysosome in individual live cells were monitored in a timeline of cellular processes using the 4-MBA modified gold NPs as the pH sensing probe by Kneipp and co-workers.[158] To optimize the SERS performance for pH sensing, Fujita and co-workers investigated the SERS performance of 18 types of gold and silver NPs with different morphologies for pH sensing, utilizing 4-MBA as SERS probe molecule. Using 4-MBA modified Au@Ag core/satellites, they performed time-lapse pH measurements in the cytosol during apoptosis of HeLa cells.[159] They further used 4-MBA modified Ag nano-assemblies to visualize the spatiotemporal change of intracellular pH.[160] It is worth noting that one promising way for intracellular pH sensing is integrating pH-sensitive molecules with SERS-based endoscopy technique, which allows detecting pH at the desired position. In this regard, He and co-workers developed a 4-MBA modified gold nanoparticle decorated nanopipette to monitor the cytosolic pH change of individual HeLa and fibroblast cells under the change of the extracellular pH.[161]

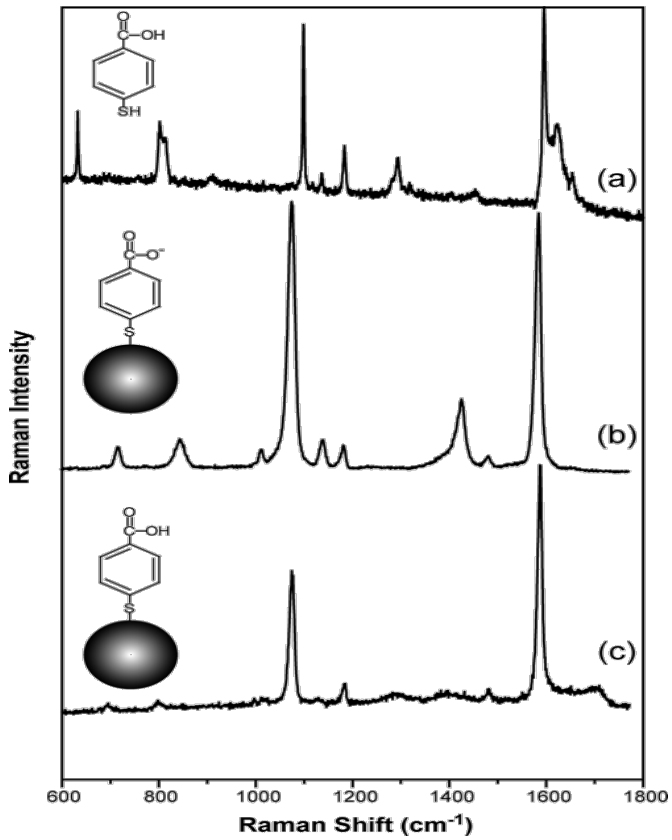

Figure 1.17. The Raman spectrum of solid 4-MBA (a) and the SERS spectra of 4-MBA attached to silver nanoparticles at pH = 12.3 (b) and pH = 5.0 (c). [adapted from[157]]

Except for 4-MBA, 4-MPy is another commonly used probe molecule. Rector and co-workers developed a gold@silver core-shell NPs acted as SERS nanosensor of endocytic vesicle that was consist of a targeting component 2,4-e-dinitrophenol-L-lysine (DNP) targeting at the FceRI receptor and a sensing part 4-MPy. The pH sensing probe was sensitive to pH changes in the pH range of 4.5 – 7.5. They obtained the whole-cell, time-lapse, endocytic vesicular pH changes during FceRI receptor-mediated endocytosis and further studied the effect of temperature on the behavior of the cells in terms of the pH monitored by the pH probe and the pH response to the dynamic external stimuli or the H^+ ATPase pump inhibitor drugs.[162, 163] Ren and co-workers developed BSA and 4-MPy modified gold NPs acted as pH nanosensor to further improve good stability and reliability. As shown in Figure 1.18, the Bovine serum albumin (BSA) functionalized Au-(4-MPy) probe (AMB) showed an excellent response in a wide pH range from 4.0 to 9.0. In contrast, no regular response was observed for the Au-(4-MPy) probe (AM). Taking advantage, the AMB pH sensor has been successfully used to monitor the pH distribution of live cells.[149] They future modified the probes with cell-penetrating-peptide TAT, an arginine-rich peptide with cationic property, to significantly

improve the internalization efficiency. With this probe, the pH response during the whole cell cycle was successfully monitored in situ.[164] In order to determine the pH values of organelles, Xu and co-workers designed mitochondria-targeted nanosensors using mitochondria targeting peptides and 4-MPy modified gold nanorods. The nanosensors possess pH response ability in the pH range from 4.0 to 9.0. The pH sensing for mitochondria was performed on a tumor cell line (human liver hepatocellular carcinoma, HepG2) and a normal cell line (mouse embryonic liver cells, BNL.CL2).[165]

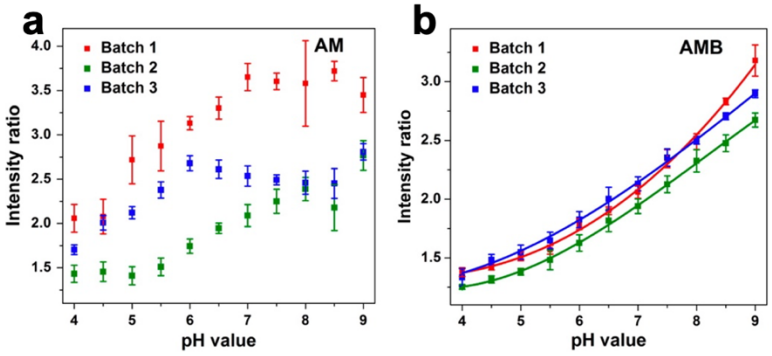

Figure 1.18. pH response of AM (a) and AMB (b) pH nanosensor of different batches shown with the intensity ratio from 1208 to 1274 cm^{-1} as a function of pH values. [adapted from[149]]

Besides, Cui and co-workers reported an intracellular pH sensor using the 4-ATP functionalized gold nanorods (GNRs) as the SERS probe. The pH-sensitive intensities of SERS bands of 4-ATP at 1142 cm^{-1}, 1390 cm^{-1}, and 1432 cm^{-1} enabled it to sense the pH value of a solution varying from 3.0 to 8.0. (Figure 1.19) After the internalized into living HeLa cells, the 4-ATP modified GNRs showed the pH-dependent SERS spectra of 4-ATP, indicating the proposed probe was able to sense intracellular pH.[166]

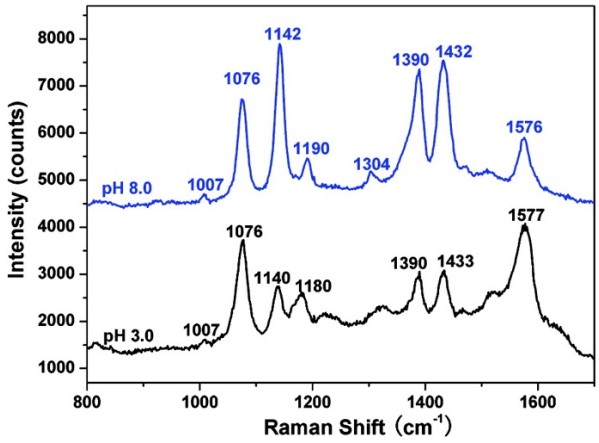

Figure 1.19. SERS spectra of 4-ATP–GNRs under pH 3.0 and 8.0. [adapted from[166]]

By far, various SERS nanosensors have been developed to monitor cellular pH through functionalizing the various SERS-active noble metal substrates with pH-sensitive molecules.[167-179] These works are of great importance not only for the demonstration of the usability of the SERS-based pH sensing technique but also for the understanding of intracellular processes. With these achievements, one could understand the dynamic pH change inside the endolysosomes with or without the external stimulus, during apoptosis and during photothermal therapy and so on, gaining sight into the whole picture of the pH regulation of the endolysosomes. But limited information is related to the other compartments, such as the cytosol and nucleus, especially for the nucleus. Considering the fact that the pH of the cytosol and nucleus has an effect on the function of cells, it is worth putting more effort into this field in order to better understand the physiological and pathological processes.

1.2.5 Curvature of the nanomaterials

The ligands functionalized nanomaterials have been used in sensing, imaging, drug delivery, and therapy.[180] In this context, the physicochemical properties of ligands play a crucial role. It is reported that the physicochemical properties of ligands immobilized on nanomaterials could be modified by the local curvatures of the nanomaterials.[181] For understanding the curvature of nanomaterial, assuming that the nanomaterial refers to a nanoparticle with the radius R, herein the curvature of nanoparticle k could be expressed as the following equation:

$$k = \frac{1}{R} \qquad 1.12$$

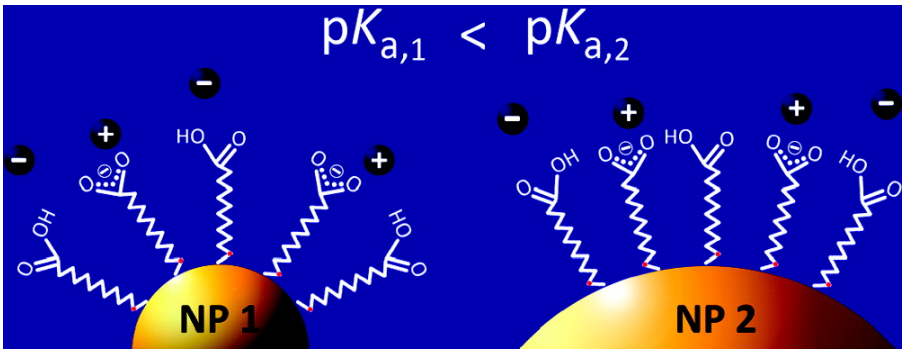

Figure 1.20. Schematic illustration of the effect of the NPs curvature on the ligands immobilized on it. [adapted from[182]]

Ligands immobilized on small gold nanoparticle which has the high curvature shown unique phenomena such as phase separation of sub-nanometer ligand domains, redox of the ligands, enhanced macromolecular crowding effect, and kinetic modulation of regioselective photoreactions, which are not observed on flat gold surfaces.[183, 184] In particular, the curvature has an effect on the acid dissociation constant (pKa) of the acidic ligands immobilized on nanoparticles.[182, 185] When the acidic ligands (COOH) immobilized on two NPs with different sizes, the acidic ligands (COOH) suffer from different intermolecular interactions.[182] More specifically, with the increase of the size of the nanoparticles, according to equation 1.12, the curvature of the NPs becomes small. As a result, the distance between the deprotonated groups (COO^-) of the acidic ligands reduces, thus, leading to the increase of the electrostatic repulsions between the acidic ligands, as illustrated in Figure 1.20. Since the energy increased situation is not favored, the system will counteract the increased energy by reducing the amount of the

deprotonated groups by shifting the acid-base equilibrium toward the protonated state. Consequently, the pKa of the acidic ligand on the NPs increases with the increase of the nanoparticle size. As shown in Figure 1.21, this curvature-dependent pKa of the acidic ligand on the NPs could be reflected in their titration.[185] The titration of spherical NPs always shows a single equivalence point. In contrast, nano-dumbbells and nanorods nano-objects, both of which have various regions of curvature, show multiple equivalence points: equivalence point 1 is from the side, and equivalence point 2 is from the tip.

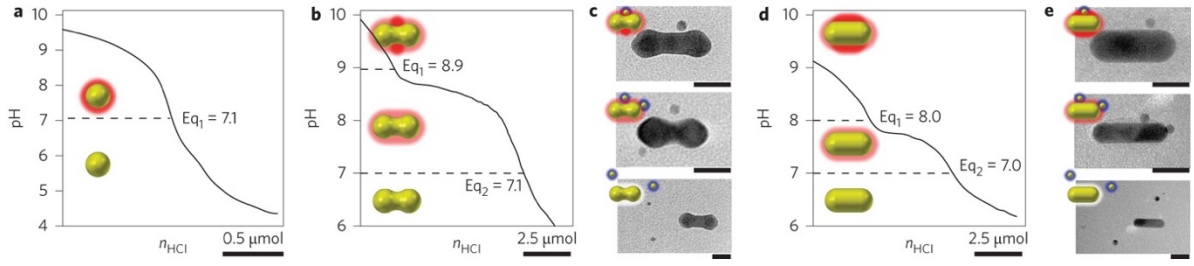

Figure 1.21. Titration of negatively charged particles. The titration of spherical NPs (a). Nano-dumbbells and nanorods (b, d). TEM images collected of larger nano-dumbbells or nanorods and smaller, TMA-coated spherical NPs of opposite charge (c, e) (all scale bars, 20 nm). [adapted from[185]]

1.3 Problem statement and research objectives

1.3.1 Problem statement

The highly compartmentalized cell is the basic structural and functional unit of organisms, which is a dynamic and heterogeneous system undergoing various metabolism.[2] In this context, the protons play a critical role in the physiological and pathological processes, and the change of the pH directly has effects on the physiological functions of living organisms.[151] In addition, intracellular pH provides basic information on various cellular processes. For example, the pH in lysosomes is involved in many cellular physiological events, such as autophagy and apoptosis.[173] Monitoring the pH in lysosomes could gain sight into the processes of these events. For another example, the pH gradient reversal, intracellular alkalization and extracellular acidosis, is known to be related to tumorigenesis with cancer cells.[6] This effect is associated with the increased glucose metabolism of cancer cells due to an oxygen-poor environment, which leads to the high production of lactate and H^+, as glycolysis byproducts.[9] Consequently, to maintain pH homeostasis, the activity of membrane proton pumps and transporters is drastically boosted, resulting in intracellular alkalization.[46] This pH of cancer cells, in general, is considered to play an essential role in cancer progressions, such as proliferation, apoptosis, metabolic adaptation, migration, and drug resistance and so on.[4, 5, 10] The studies on the lysosomal, cytosolic, and nuclear pH variations are therefore crucial for elucidating the interplay with cell functions and, in turn, gaining insights into both pH-related pathological processes and the studies on the lysosomal, cytosolic, and nuclear pH variations responding to the anticancer drug should contribute to the development of new therapeutic strategies.

Surface-enhanced Raman spectroscopy (SERS) as a pH-sensing technique shows great advantages compared with other pH-sensing techniques, which are as follows: (a) no damage for the biological samples; (b) negligible disturbance from the fluorescence of biological matters and the Raman signal of water; (c) no quenching or photobleaching.[151] Therefore, taking these merits, the pH SERS-based pH sensing technique should be able to contribute to the study of pH-related physiological reactions in cells and the development of new therapeutic strategies. In this context, SERS-based probes have been proposed to sense cellular pH. To the end, acidic ligands functionalized noble metal NPs are commonly used as SERS-based pH-sensing probes. The apparent dissociation constant (pKa) of acid ligands is known to be sensitive to NPs curvature.[182] Thus, SERS pH sensitivity should be related to NP morphology.

However, the coupling of SERS sensitivity of the probe molecules to pH with NP morphology remains ambiguous.

In addition, these NP-based probes are trapped in the endolysosomal system due to the internalized way (endocytosis) and the capture by cells, limiting the pH sensing to the inside of these acidic vesicles.[186-188] SERS-active endoscopy, such as glass micropipettes and fiber tips, have been developed for pH sensing for other compartments of the cell. These techniques, however, might cause drastic cell deformation and damage.[189] In the light of the foregoing, a new strategy is needed to monitor the pH variation of cells at the desired position such as the cytosolic and nuclear for a deep and comprehensive understanding of the behavior of cells, contributing to the study of the physiological and pathological processes as well as the development of new therapeutic strategies.

1.3.2 Research objectives

(1) Development of a method to design the SERS-based intracellular pH sensor

As aforementioned, many different noble metal nanostructures, including nanorods, nanospheres and nanostars, have been functionalized with the pH-sensitive molecules for pH sensing for various biological processes. However, a tailored nanosensor of high sensitivity with a targeted pH range for a biological condition has not been reported. This gives rise to such a question: how to design the probe for a certain purpose. In this context, in this study, we would like to figure out the coupling of SERS sensitivity of the probe molecules to pH with NP morphology, namely developing a method to tailor the pH sensing sensitivity of the probe for a targeted pH range and use the resulting probe for pH monitoring in endolysosomes, considering the importance of the endolysosomes.

(2) Development of a SERS-based pH sensor for the cytosolic and nuclear pH sensing

After clarifying the coupling of SERS sensitivity of the probe molecules to pH with the morphology of the nanomaterials, in this study, we would like to apply this finding to develop a SERS-based pH sensor for cytosolic and nuclear pH monitoring. As aforementioned, most of the pH sensors are for endolysosomes, and a great achievement related to the pH variation of the endolysosomes has been made with these efforts. However, very limited information is available about the cytosolic and nuclear pH variation, especially for the nucleus. And considering the key role of the cytosolic and nuclear pH in cells, therefore, in this study, we would like to give our contribution to the cytosolic and nuclear pH monitoring.

1.4 References

1. Ray, P. D.; Fry, R. C., The cell: The fundamental unit in systems biology[M]//Systems Biology in Toxicology and Environmental Health. *Academic Press* **2015**, 11-42.

2. Casey, J. R.; Grinstein, S.; Orlowski, J., Sensors and regulators of intracellular pH. *Nat. Rev. Mol. Cell Biol.* **2010,** *11* (1), 50-61.

3. Koch, L. M.; Birkeland, E. S.; Battaglioni, S.; Helle, X.; Meerang, M.; Hiltbrunner, S.; Ibanez, A. J.; Peter, M.; Curioni-Fontecedro, A.; Opitz, I.; Dechant, R., Cytosolic pH regulates proliferation and tumour growth by promoting expression of cyclin D1. *Nat. Metab.* **2020,** *2* (11), 1212-1222.

4. Czowski, B. J.; Romero-Moreno, R.; Trull, K. J.; White, K. A., Cancer and pH Dynamics: Transcriptional Regulation, Proteostasis, and the Need for New Molecular Tools. *CANCERS* **2020,** *12* (10), 2760.

5. Korenchan, D. E.; Flavell, R. R. J. C., Spatiotemporal pH heterogeneity as a promoter of cancer progression and therapeutic resistance. *CANCERS* **2019,** *11* (7), 1026.

6. Persi, E.; Duran-Frigola, M.; Damaghi, M.; Roush, W. R.; Aloy, P.; Cleveland, J. L.; Gillies, R. J.; Ruppin, E., Systems analysis of intracellular pH vulnerabilities for cancer therapy. *Nat. Commun.* **2018,** *9* (1), 2997.

7. Xu, H.; Ren, D., Lysosomal physiology. *Annu. Rev. Physiol.* **2015,** *77* (1), 57-80.

8. Swietach, P.; Vaughan-Jones, R. D.; Harris, A. L.; Hulikova, A., The chemistry, physiology and pathology of pH in cancer. *Philos. Trans. R. Soc. Lond. B Biol. Sci.* **2014,** *369* (1638), 20130099.

9. Damaghi, M.; Wojtkowiak, J. W.; Gillies, R. J., pH sensing and regulation in cancer. *Front Physiol* **2013,** *4* (370), 370.

10. Raghunand, N.; Gillies, R. J., pH and drug resistance in tumors. *Drug Resist. Updat.* **2000,** *3* (1), 39-47.

11. De Duve, C.; Pressman, B. C.; Gianetto, R.; Wattiaux, R.; Appelmans, F., Tissue fractionation studies. 6. Intracellular distribution patterns of enzymes in rat-liver tissue. *Biochem. J.* **1955,** *60* (4), 604-17.

12. Zeng, J.; Shirihai, O. S.; Grinstaff, M. W., Modulating lysosomal pH: a molecular and nanoscale materials design perspective. *J Life Sci (Westlake Village)* **2020,** *2* (4), 25-37.

13. Forgac, M., Vacuolar ATPases: rotary proton pumps in physiology and pathophysiology. *Nat. Rev. Mol. Cell Biol.* **2007,** *8* (11), 917-29.

14. Holliday, L. S., Vacuolar H+-ATPase: An Essential Multitasking Enzyme in Physiology and Pathophysiology. *New J. Chem.* **2014,** *2014*, 1-21.

15. Song, Q.; Meng, B.; Xu, H.; Mao, Z., The emerging roles of vacuolar-type ATPase-dependent Lysosomal acidification in neurodegenerative diseases. *Transl. Neurodegener.* **2020,** *9* (1), 17.

16. Beyenbach, K. W.; Wieczorek, H., The V-type H^+ ATPase: molecular structure and function, physiological roles and regulation. *J. Exp. Biol.* **2006,** *209* (Pt 4), 577-89.

17. Lawrence, R. E.; Zoncu, R., The lysosome as a cellular centre for signalling, metabolism and quality control. *Nat. Cell Biol.* **2019,** *21* (2), 133-142.

18. Mindell, J. A., Lysosomal acidification mechanisms. *Annu. Rev. Physiol.* **2012,** *74*, 69-86.

19. Ittner, L. M.; Gotz, J., Amyloid-beta and tau--a toxic pas de deux in Alzheimer's disease. *Nat. Rev. Neurosci.* **2011,** *12* (2), 65-72.

20. Wolfe, D. M.; Lee, J. H.; Kumar, A.; Lee, S.; Orenstein, S. J.; Nixon, R. A., Autophagy failure in Alzheimer's disease and the role of defective lysosomal acidification. *Eur. J. Neurosci.* **2013,** *37* (12), 1949-61.

21. Hu, Y. B.; Dammer, E. B.; Ren, R. J.; Wang, G., The endosomal-lysosomal system: from acidification and cargo sorting to neurodegeneration. *Transl. Neurodegener.* **2015,** *4* (1), 18.

22. Colacurcio, D. J.; Nixon, R. A., Disorders of lysosomal acidification—The emerging role of v-ATPase in aging and neurodegenerative disease. *Ageing Res. Rev.* **2016,** *32*, 75-88.

23. Funderburk, S. F.; Marcellino, B. K.; Yue, Z., Cell "self-eating" (autophagy) mechanism in Alzheimer's disease. *Mt. Sinai J. Med.* **2010,** *77* (1), 59-68.

24. Lee, S.; Sato, Y.; Nixon, R. A., Lysosomal proteolysis inhibition selectively disrupts axonal transport of degradative organelles and causes an Alzheimer's-like axonal dystrophy. *J. Neurosci.* **2011,** *31* (21), 7817-30.

25. Bagh, M. B.; Peng, S.; Chandra, G.; Zhang, Z.; Singh, S. P.; Pattabiraman, N.; Liu, A.; Mukherjee, A. B., Misrouting of v-ATPase subunit V0a1 dysregulates lysosomal acidification in a neurodegenerative lysosomal storage disease model. *Nat. Commun.* **2017,** *8* (1), 14612.

26. Majumdar, A.; Cruz, D.; Asamoah, N.; Buxbaum, A.; Sohar, I.; Lobel, P.; Maxfield, F. R., Activation of microglia acidifies lysosomes and leads to degradation of Alzheimer amyloid fibrils. *Mol. Biol. Cell* **2007,** *18* (4), 1490-6.

27. Liberti, M. V.; Locasale, J. W., The Warburg Effect: How Does it Benefit Cancer Cells? *Trends Biochem. Sci.* **2016,** *41* (3), 211-218.

28. White, K. A.; Grillo-Hill, B. K.; Barber, D. L., Cancer cell behaviors mediated by dysregulated pH dynamics at a glance. *J. Cell. Sci.* **2017,** *130* (4), 663-669.

29. Bohme, I.; Bosserhoff, A. K., Acidic tumor microenvironment in human melanoma. *Pigment Cell Melanoma Res.* **2016,** *29* (5), 508-23.

30. Chen, R.; Jäättelä, M.; Liu, B., Lysosome as a Central Hub for Rewiring PH Homeostasis in Tumors. *CANCERS* **2020,** *12* (9), 2437.

31. White, E., The role for autophagy in cancer. *J. Clin. Invest.* **2015,** *125* (1), 42-6.

32. Li, Y.; Cao, F.; Li, M.; Li, P.; Yu, Y.; Xiang, L.; Xu, T.; Lei, J.; Tai, Y. Y.; Zhu, J.; Yang, B.; Jiang, Y.; Zhang, X.; Duo, L.; Chen, P.; Yu, X., Hydroxychloroquine induced lung cancer suppression by enhancing chemo-sensitization and promoting the transition of M2-TAMs to M1-like macrophages. *J. Exp. Clin. Cancer Res.* **2018,** *37* (1), 259.

33. Liu, J.; Huang, Y.; Kumar, A.; Tan, A.; Jin, S.; Mozhi, A.; Liang, X. J., pH-sensitive nano-systems for drug delivery in cancer therapy. *Biotechnol. Adv.* **2014,** *32* (4), 693-710.

34. Robinson, P. K., Enzymes: principles and biotechnological applications. *Essays Biochem.* **2015,** *59*, 1-41.

35. Swietach, P., What is pH regulation, and why do cancer cells need it? *Cancer Metastasis Rev.* **2019,** *38* (1-2), 5-15.

36. Dechant, R.; Saad, S.; Ibanez, A. J.; Peter, M., Cytosolic pH regulates cell growth through distinct GTPases, Arf1 and Gtr1, to promote Ras/PKA and TORC1 activity. *Mol. Cell* **2014,** *55* (3), 409-21.

37. Brown, D. A.; Melvin, J. E.; Yule, D. I., Critical role for NHE1 in intracellular pH regulation in pancreatic acinar cells. *Am. J. Physiol. Gastrointest. Liver Physiol.* **2003,** *285* (5), G804-12.

38. Valles, P. G.; Bocanegra, V.; Gil Lorenzo, A.; Costantino, V. V., Physiological Functions and Regulation of the Na^+/H^+ Exchanger [NHE1] in Renal Tubule Epithelial Cells. *Kidney Blood Press. Res.* **2015,** *40* (5), 452-66.

39. Li, X.; Dutta, D.; Jung, M.; Zimmermann, R.; Fliegel, L., Amino Acids 563-566 of the Na(+)/H(+) Exchanger Isoform 1 C-Terminal Cytosolic Tail Prevent Protein Degradation and Stabilize Protein Expression and Activity. *Int. J. Mol. Sci.* **2020,** *21* (5), 1737.

40. Fliegel, L., Structural and Functional Changes in the Na^+/H^+ Exchanger Isoform 1, Induced by Erk1/2 Phosphorylation. *Int. J. Mol. Sci.* **2019,** *20* (10), 2378.

41. Webb, B. A.; Chimenti, M.; Jacobson, M. P.; Barber, D. L., Dysregulated pH: a perfect storm for cancer progression. *Nat. Rev. Cancer* **2011,** *11* (9), 671-7.

42. Meehan, J.; Ward, C.; Turnbull, A.; Bukowski-Wills, J.; Finch, A. J.; Jarman, E. J.; Xintaropoulou, C.; Martinez-Perez, C.; Gray, M.; Pearson, M.; Mullen, P.; Supuran, C. T.; Carta, F.; Harrison, D. J.; Kunkler, I. H.; Langdon, S. P., Inhibition of pH regulation as a therapeutic strategy in hypoxic human breast cancer cells. *Oncotarget* **2017,** *8* (26).

43. Jose, C.; Bellance, N.; Rossignol, R., Choosing between glycolysis and oxidative phosphorylation: a tumor's dilemma? *Biochim. Biophys. Acta* **2011,** *1807* (6), 552-61.

44. Marchiq, I.; Pouyssegur, J., Hypoxia, cancer metabolism and the therapeutic benefit of targeting lactate/H^+ symporters. *J. Mol. Med.* **2016,** *94* (2), 155-71.

45. Yu, X.; Li, S., Non-metabolic functions of glycolytic enzymes in tumorigenesis. *Oncogene* **2017,** *36* (19), 2629-2636.

46. White, K. A.; Grillo-Hill, B. K.; Barber, D. L., Cancer cell behaviors mediated by dysregulated pH dynamics at a glance. *J. Cell Sci.* **2017,** *130* (4), 663-669.

47. Pérez-Sala, D.; Collado-Escobar, D.; Mollinedo, F. J. J. o. B. C., Intracellular alkalinization suppresses lovastatin-induced apoptosis in HL-60 cells through the inactivation of a pH-dependent endonuclease. *J. Biol. Chem.* **1995,** *270* (11), 6235-6242.

48. Matsuyama, S.; Llopis, J.; Deveraux, Q. L.; Tsien, R. Y.; Reed, J. C., Changes in intramitochondrial and cytosolic pH: early events that modulate caspase activation during apoptosis. *Nat. Cell Biol.* **2000,** *2* (6), 318-25.

49. Amith, S. R.; Wilkinson, J. M.; Fliegel, L., KR-33028, a potent inhibitor of the Na^+/H^+ exchanger NHE1, suppresses metastatic potential of triple-negative breast cancer cells. *Biochem. Pharmacol.* **2016,** *118*, 31-39.

50. Raudenska, M.; Balvan, J.; Fojtu, M.; Gumulec, J.; Masarik, M., Unexpected therapeutic effects of cisplatin. *Metallomics* **2019,** *11* (7), 1182-1199.

51. Yang, F.; Teves, S. S.; Kemp, C. J.; Henikoff, S., Doxorubicin, DNA torsion, and chromatin dynamics. *Biochim. Biophys. Acta* **2014,** *1845* (1), 84-9.

52. Bright, G.; Fisher, G.; Rogowska, J.; Taylor, D., Fluorescence ratio imaging microscopy: temporal and spatial measurements of cytoplasmic pH. *J. Cell Biol.* **1987,** *104* (4), 1019-1033.

53. Cody, S. H.; Dubbin, P. N.; Beischer, A. D.; Duncan, N. D.; Hill, J. S.; Kaye, A. H.; Williams, D. A., Intracellular pH mapping with SNARF-1 and confocal microscopy. I: A quantitative technique for living tissue and isolated cells. *Micron* **1993,** *24* (6), 573-580.

54. Seksek, O.; Bolard, J., Nuclear pH gradient in mammalian cells revealed by laser microspectrofluorimetry. *J. Cell Sci.* **1996,** *109 (Pt 1)* (1), 257-62.

55. Smekal, A., Zur Quantentheorie der Dispersion. *Die Naturwissenschaften* **1923,** *11* (43), 873-875.

56. Raman, C. V.; Krishnan, K. S., A New Type of Secondary Radiation. *Nature* **1928,** *121* (3048), 501-502.

57. Kumar, S.; Kumar, P.; Das, A.; Pathak, C. S., Surface-Enhanced Raman Scattering: Introduction and Applications. In *Recent Advances in Nanophotonics-Fundamentals and Applications*, IntechOpen London, UK: 2020; pp 1-24.

58. Bruno, G.; Classical Theory of Rayleigh and Raman Scattering. In *The Raman Effect*, 2002; pp 31-48.

59. Procházka, M. J. B.; medical physics, b. e., Surface-enhanced raman spectroscopy. **2016**.

60. Ornstein, L. S.; Rekveld, J.; Utrecht, Intensity Measurements in the Raman Effect and the Distribution Law of Maxwell-Boltzmann. *Physical Review* **1929,** *34* (5), 720-725.

61. Shipp, D. W.; Sinjab, F.; Notingher, I., Raman spectroscopy: techniques and applications in the life sciences. *Adv. Opt. Photon.* **2017,** *9* (2), 315-428.

62. Hackshaw, K. V.; Miller, J. S.; Aykas, D. P.; Rodriguez-Saona, L., Vibrational Spectroscopy for Identification of Metabolites in Biologic Samples. *Molecules* **2020,** *25* (20), 4725.

63. Fleischmann, M.; Hendra, P. J.; McQuillan, A. J., Raman spectra of pyridine adsorbed at a silver electrode. *Chem. Phys. Lett.* **1974,** *26* (2), 163-166.

64. Jeanmaire, D. L.; Van Duyne, R. P., Surface raman spectroelectrochemistry. *J. Electroanal. Chem.* **1977,** *84* (1), 1-20.

65. Albrecht, M. G.; Creighton, J. A., Anomalously intense Raman spectra of pyridine at a silver electrode. *J. Am. Chem. Soc.* **2002,** *99* (15), 5215-5217.

66. Zong, C.; Xu, M.; Xu, L. J.; Wei, T.; Ma, X.; Zheng, X. S.; Hu, R.; Ren, B., Surface-Enhanced Raman Spectroscopy for Bioanalysis: Reliability and Challenges. *Chem. Rev.* **2018,** *118* (10), 4946-4980.

67. Le Ru, E. C.; Blackie, E.; Meyer, M.; Etchegoin, P. G., Surface Enhanced Raman Scattering Enhancement Factors: A Comprehensive Study. *J. Phys. Chem. C* **2007,** *111* (37), 13794-13803.

68. Nie, S.; Emory, S. R., Probing Single Molecules and Single Nanoparticles by Surface-Enhanced Raman Scattering. *Science* **1997,** *275* (5303), 1102-6.

69. Wei, H.; Xu, H., Hot spots in different metal nanostructures for plasmon-enhanced Raman spectroscopy. *Nanoscale* **2013,** *5* (22), 10794-10805.

70. Cao, E.; Lin, W.; Sun, M.; Liang, W.; Song, Y., Exciton-plasmon coupling interactions: from principle to applications. *Nanophotonics* **2018,** *7* (1), 145-167.

71. Li, M.; Cushing, S. K.; Wu, N., Plasmon-enhanced optical sensors: a review. *Analyst* **2015,** *140* (2), 386-406.

72. Das, G.; Coluccio, M. L.; Alrasheed, S.; Giugni, A.; Allione, M.; Torre, B.; Perozziello, G.; Candeloro, P.; Di Fabrizio, E., Plasmonic nanostructures for the ultrasensitive detection of biomolecules. *La Rivista del Nuovo Cimento* **2016,** *39* (11), 547-586.

73. Jones, M. R.; Osberg, K. D.; Macfarlane, R. J.; Langille, M. R.; Mirkin, C. A., Templated techniques for the synthesis and assembly of plasmonic nanostructures. *Chem. Rev.* **2011,** *111* (6), 3736-827.

74. Petryayeva, E.; Krull, U. J., Localized surface plasmon resonance: nanostructures, bioassays and biosensing-a review. *Anal. Chim. Acta* **2011,** *706* (1), 8-24.

75. Willets, K. A.; Van Duyne, R. P., Localized surface plasmon resonance spectroscopy and sensing. *Annu. Rev. Phys. Chem.* **2007,** *58*, 267-97.

76. Pilot, R.; Signorini, R.; Durante, C.; Orian, L.; Bhamidipati, M.; Fabris, L., A Review on Surface-Enhanced Raman Scattering. *Biosensors* **2019,** *9* (2).

77. Chowdhury, J., How the Charge Transfer (CT) Contributions Influence the SERS Spectra of Molecules? A Retrospective from the View of Albrecht's "A" and Herzberg-Teller Contributions. *Appl. Spectrosc. Rev.* **2014,** *50* (3), 240-260.

78. Lombardi, J. R.; Birke, R. L., A Unified Approach to Surface-Enhanced Raman Spectroscopy. *J. Phys. Chem. C* **2008,** *112* (14), 5605-5617.

79. Lombardi, J. R.; Birke, R. L.; Lu, T.; Xu, J., Charge-transfer theory of surface enhanced Raman spectroscopy: Herzberg–Teller contributions. *J. Chem. Phys.* **1986,** *84* (8), 4174-4180.

80. Yang, L.; Jiang, X.; Ruan, W.; Zhao, B.; Xu, W.; Lombardi, J. R., Observation of Enhanced Raman Scattering for Molecules Adsorbed on TiO2 Nanoparticles: Charge-Transfer Contribution. *J. Phys. Chem. C* **2008,** *112* (50), 20095-20098.

81. Yang, L.; Qin, X.; Jiang, X.; Gong, M.; Yin, D.; Zhang, Y.; Zhao, B., SERS investigation of ciprofloxacin drug molecules on TiO_2 nanoparticles. *Phys. Chem. Chem. Phys.* **2015,** *17* (27), 17809-15.

82. Musumeci, A.; Gosztola, D.; Schiller, T.; Dimitrijevic, N. M.; Mujica, V.; Martin, D.; Rajh, T., SERS of semiconducting nanoparticles (TiO_2 hybrid composites). *J. Am. Chem. Soc.* **2009,** *131* (17), 6040-1.

83. Xu, M.; Liang, T.; Shi, M.; Chen, H., Graphene-like two-dimensional materials. *Chem. Rev.* **2013,** *113* (5), 3766-98.

84. Geim, A. K., Graphene: status and prospects. *Science* **2009,** *324* (5934), 1530-4.

85. Geim, A. K.; Novoselov, K. S., The rise of graphene. *Nat. Mater.* **2007,** *6* (3), 183-91.

86. Zhang, N.; Tong, L.; Zhang, J., Graphene-Based Enhanced Raman Scattering toward Analytical Applications. *Chem. Mater.* **2016,** *28* (18), 6426-6435.

87. Lai, H.; Xu, F.; Zhang, Y.; Wang, L., Recent progress on graphene-based substrates for surface-enhanced Raman scattering applications. *J. Mater. Chem. B* **2018,** *6* (24), 4008-4028.

88. Xie, L.; Ling, X.; Fang, Y.; Zhang, J.; Liu, Z., Graphene as a substrate to suppress fluorescence in resonance Raman spectroscopy. *J. Am. Chem. Soc.* **2009,** *131* (29), 9890-1.

89. Ling, X.; Xie, L.; Fang, Y.; Xu, H.; Zhang, H.; Kong, J.; Dresselhaus, M. S.; Zhang, J.; Liu, Z., Can graphene be used as a substrate for Raman enhancement? *Nano Lett.* **2010,** *10* (2), 553-61.

90. Zhou, H. C.; Long, J. R.; Yaghi, O. M, Introduction to Metal–Organic Frameworks. *Chem. Rev.* **2012,** *112* (2), 673-674.

91. Yuan, S.; Feng, L.; Wang, K.; Pang, J.; Bosch, M.; Lollar, C.; Sun, Y.; Qin, J.; Yang, X.; Zhang, P.; Wang, Q.; Zou, L.; Zhang, Y.; Zhang, L.; Fang, Y.; Li, J.; Zhou, H.-C., Stable Metal–Organic Frameworks: Design, Synthesis, and Applications. *Adv. Mater.* **2018,** *30* (37), 1704303.

92. Safaei, M.; Foroughi, M. M.; Ebrahimpoor, N.; Jahani, S.; Omidi, A.; Khatami, M., A review on metal-organic frameworks: Synthesis and applications. *TrAC - Trends Anal. Chem.* **2019,** *118*, 401-425.

93. Kumar, P.; Deep, A.; Kim, K.-H., Metal organic frameworks for sensing applications. *TrAC, Trends Anal. Chem.* **2015,** *73*, 39-53.

94. Manousi, N.; Giannakoudakis, D. A.; Rosenberg, E.; Zachariadis, G. A., Extraction of Metal Ions with Metal-Organic Frameworks. *Molecules* **2019,** *24* (24), 4605.

95. Nong, W.; Liu, X.; Wang, Q.; Wu, J.; Guan, Y., Metal-organic Framework-based Materials: Synthesis, Stability and Applications in Food Safety and Preservation. *ES Food & Agroforestry* **2020,** *1*, 11-40.

96. Baumann, A. E.; Burns, D. A.; Liu, B.; Thoi, V. S., Metal-organic framework functionalization and design strategies for advanced electrochemical energy storage devices. *Commun. Chem.* **2019,** *2* (1), 86.

97. Tanabe, K. K.; Cohen, S. M., Postsynthetic modification of metal-organic frameworks-a progress report. *Chem. Soc. Rev.* **2011,** *40* (2), 498-519.

98. Yu, T.-H.; Ho, C.-H.; Wu, C.-Y.; Chien, C.-H.; Lin, C.-H.; Lee, S., Metal-organic frameworks: a novel SERS substrate. *J. Raman Spectrosc.* **2013,** *44* (11), 1506-1511.

99. Sun, H.; Cong, S.; Zheng, Z.; Wang, Z.; Chen, Z.; Zhao, Z., Metal-Organic Frameworks as Surface Enhanced Raman Scattering Substrates with High Tailorability. *J. Am. Chem. Soc.* **2019,** *141* (2), 870-878.

100. Xu, J.; Cheng, C.; Shang, S.; Gao, W.; Zeng, P.; Jiang, S., Flexible, Reusable SERS Substrate Derived from ZIF-67 by Adjusting LUMO and HOMO and Its Application in Identification of Bacteria. *ACS Appl. Mater. Interfaces* **2020,** *12* (44), 49452-49463.

101. Fu, J. H.; Zhong, Z.; Xie, D.; Guo, Y. J.; Kong, D. X.; Zhao, Z. X.; Zhao, Z. X.; Li, M., SERS-Active MIL-100(Fe) Sensory Array for Ultrasensitive and Multiplex Detection of VOCs. *Angew. Chem. Int. Ed.* **2020,** *59* (46), 20489-20498.

102. Nguyen, A. H.; Peters, E. A.; Schultz, Z. D., Bioanalytical applications of surface-enhanced Raman spectroscopy: de novo molecular identification. *Rev. Anal. Chem.* **2017,** *36* (4).

103. Shi, R.; Liu, X.; Ying, Y., Facing Challenges in Real-Life Application of Surface-Enhanced Raman Scattering: Design and Nanofabrication of Surface-Enhanced Raman Scattering Substrates for Rapid Field Test of Food Contaminants. *J. Agric. Food Chem.* **2018,** *66* (26), 6525-6543.

104. Luo, S. C.; Sivashanmugan, K.; Liao, J. D.; Yao, C. K.; Peng, H. C., Nanofabricated SERS-active substrates for single-molecule to virus detection in vitro: a review. *Biosens. Bioelectron.* **2014,** *61*, 232-40.

105. Abu Hatab, N. A.; Oran, J. M.; Sepaniak, M. J., Surface-enhanced Raman spectroscopy substrates created via electron beam lithography and nanotransfer printing. *ACS Nano* **2008,** *2* (2), 377-85.

106. Zhang, X.; Zhao, J.; Whitney, A. V.; Elam, J. W.; Van Duyne, R. P., Ultrastable substrates for surface-enhanced Raman spectroscopy: Al_2O_3 overlayers fabricated by atomic layer deposition yield improved anthrax biomarker detection. *J. Am. Chem. Soc.* **2006,** *128* (31), 10304-9.

107. Shiohara, A.; Wang, Y.; Liz-Marzán, L. M., Recent approaches toward creation of hot spots for SERS detection. *JPPC* **2014,** *21*, 2-25.

108. Leopold, N.; Lendl, B., A New Method for Fast Preparation of Highly Surface-Enhanced Raman Scattering (SERS) Active Silver Colloids at Room Temperature by Reduction of Silver Nitrate with Hydroxylamine Hydrochloride. *J. Phys. Chem. B* **2003,** *107* (24), 5723-5727.

109. Stiufiuc, R.; Iacovita, C.; Lucaciu, C. M.; Stiufiuc, G.; Dutu, A. G.; Braescu, C.; Leopold, N., SERS-active silver colloids prepared by reduction of silver nitrate with short-chain polyethylene glycol. *Nanoscale Res. Lett.* **2013,** *8* (1), 47.

110. Israelsen, N. D.; Hanson, C.; Vargis, E., Nanoparticle properties and synthesis effects on surface-enhanced Raman scattering enhancement factor: an introduction. *Sci. World J.* **2015,** *2015*, 124582.

111. Mosier-Boss, P. A., Review of SERS Substrates for Chemical Sensing. *Nanomaterials* **2017,** *7* (6).

112. Hong, L.; Li, Q.; Lin, H.; Li, Y., Synthesis of flower-like silver nanoarchitectures at room temperature. *Mater. Res. Bull.* **2009,** *44* (6), 1201-1204.

113. Sun, X., Morphology and size-controllable preparation of silver nanostructures through a wet-chemical route at room temperature. *Inorg. Mater.* **2010,** *46* (6), 679-682.

114. Liu, J.; Lin, Q.; Zhou, Y.; Dai, J.; Han, Y., Shape Controllable Synthesis of Silver Particles by Selecting the Crystallization Routes. *KONA Powder Part. J.* **2020,** *37* (0), 166-175.

115. Thanh, N. T.; Maclean, N.; Mahiddine, S., Mechanisms of nucleation and growth of nanoparticles in solution. *Chem. Rev.* **2014,** *114* (15), 7610-30.

116. Patakfalvi, R.; Papp, S.; Dékány, I., The kinetics of homogeneous nucleation of silver nanoparticles stabilized by polymers. *J. Nanoparticle Res.* **2006,** *9* (3), 353-364.

117. Sun, Y.; Xia, Y., Shape-controlled synthesis of gold and silver nanoparticles. *Science* **2002,** *298* (5601), 2176-9.

118. Qin, Y.; Ji, X.; Jing, J.; Liu, H.; Wu, H.; Yang, W., Size control over spherical silver nanoparticles by ascorbic acid reduction. *Colloids Surf. A Physicochem. Eng. Asp.* **2010,** *372* (1-3), 172-176.

119. Zhou, S.; Li, J.; Gilroy, K. D.; Tao, J.; Zhu, C.; Yang, X.; Sun, X.; Xia, Y., Facile Synthesis of Silver Nanocubes with Sharp Corners and Edges in an Aqueous Solution. *ACS Nano* **2016,** *10* (11), 9861-9870.

120. Liang, H.; Wang, W.; Huang, Y.; Zhang, S.; Wei, H.; Xu, H., Controlled Synthesis of Uniform Silver Nanospheres. *J. Phys. Chem. C* **2010,** *114* (16), 7427-7431.

121. Wu, C.; Zhou, X.; Wei, J., Localized Surface Plasmon Resonance of Silver Nanotriangles Synthesized by a Versatile Solution Reaction. *Nanoscale Res. Lett.* **2015,** *10* (1), 1058.

122. Korte, K. E.; Skrabalak, S. E.; Xia, Y., Rapid synthesis of silver nanowires through a $CuCl^-$ or $CuCl_2^-$mediated polyol process. *J. Mater. Chem.* **2008,** *18* (4), 437-441.

123. Shahzad, A.; Chung, J.; Lee, T.-J.; Kim, Y. H.; Bhang, S. H.; Kim, W.-S.; Yu, T., A Facile Room Temperature Synthesis of Large Silver Nanoplates with Low Cytotoxicity. *ChemistrySelect* **2018,** *3* (6), 1801-1808.

124. Ko, H.; Singamaneni, S.; Tsukruk, V. V., Nanostructured Surfaces and Assemblies as SERS Media. *Small* **2008,** *4* (10), 1576-1599.

125. Moskovits, M., Surface-enhanced Raman spectroscopy: a brief retrospective. *J. Raman Spectrosc.* **2005,** *36* (6-7), 485-496.

126. Abalde-Cela, S.; Aldeanueva-Potel, P.; Mateo-Mateo, C.; Rodriguez-Lorenzo, L.; Alvarez-Puebla, R. A.; Liz-Marzan, L. M., Surface-enhanced Raman scattering biomedical applications of plasmonic colloidal particles. *J. R. Soc. Interface* **2010,** *7 Suppl 4* (suppl_4), S435-50.

127. Ouyang, L.; Ren, W.; Zhu, L.; Irudayaraj, J., Prosperity to challenges: recent approaches in SERS substrate fabrication. *Rev. Anal. Chem.* **2017,** *36* (1).

128. Hao, E.; Schatz, G. C., Electromagnetic fields around silver nanoparticles and dimers. *J. Chem. Phys.* **2004,** *120* (1), 357-66.

129. Kasani, S.; Curtin, K.; Wu, N., A review of 2D and 3D plasmonic nanostructure array patterns: fabrication, light management and sensing applications. *Nanophotonics* **2019,** *8* (12), 2065-2089.

130. Link, S.; El-Sayed, M. A., Size and Temperature Dependence of the Plasmon Absorption of Colloidal Gold Nanoparticles. *J. Phys. Chem. B* **1999,** *103* (21), 4212-4217.

131. Nehl, C. L.; Hafner, J. H., Shape-dependent plasmon resonances of gold nanoparticles. *J. Mater. Chem.* **2008,** *18* (21), 2415-2419.

132. Andrade-Neto, A. J. R. B. d. E. d. F., *Revista Brasileira de Ensino de Física* **2016,** *39*.

133. Erwin, W. R.; Zarick, H. F.; Talbert, E. M.; Bardhan, R., Light trapping in mesoporous solar cells with plasmonic nanostructures. *Energy Environ. Sci.* **2016,** *9* (5), 1577-1601.

134. Hong, S.; Li, X., Optimal Size of Gold Nanoparticles for Surface-Enhanced Raman Spectroscopy under Different Conditions. *J. Nanomater.* **2013,** *2013*, 1-9.

135. Yang, Y.; Liu, J.; Fu, Z. W.; Qin, D., Galvanic replacement-free deposition of Au on Ag for core-shell nanocubes with enhanced chemical stability and SERS activity. *J. Am. Chem. Soc.* **2014,** *136* (23), 8153-6.

136. Chatterjee, S.; Ringane, A. B.; Arya, A.; Das, G. M.; Dantham, V. R.; Laha, R.; Hussian, S., A high-yield, one-step synthesis of surfactant-free gold nanostars and numerical study for single-molecule SERS application. *J. Nanoparticle Res.* **2016,** *18* (8), 242.

137. Giljohann, D. A.; Seferos, D. S.; Daniel, W. L.; Massich, M. D.; Patel, P. C.; Mirkin, C. A., Gold nanoparticles for biology and medicine. *Angew. Chem. Int. Ed.* **2010,** *49* (19), 3280-94.

138. Herizchi, R.; Abbasi, E.; Milani, M.; Akbarzadeh, A., Current methods for synthesis of gold nanoparticles. *Artif. Cells Nanomed. Biotechnol.* **2016,** *44* (2), 596-602.

139. Perezjuste, J.; Pastorizasantos, I.; Lizmarzan, L.; Mulvaney, P., Gold nanorods: Synthesis, characterization and applications. *Coord. Chem. Rev.* **2005,** *249* (17-18), 1870-1901.

140. Gole, A.; Murphy, C. J., Seed-Mediated Synthesis of Gold Nanorods: Role of the Size and Nature of the Seed. *Chem. Mater.* **2004,** *16* (19), 3633-3640.

141. Park, J. E.; Lee, Y.; Nam, J. M., Precisely Shaped, Uniformly Formed Gold Nanocubes with Ultrahigh Reproducibility in Single-Particle Scattering and Surface-Enhanced Raman Scattering. *Nano Lett.* **2018,** *18* (10), 6475-6482.

142. Kuttner, C.; Mayer, M.; Dulle, M.; Moscoso, A.; Lopez-Romero, J. M.; Forster, S.; Fery, A.; Perez-Juste, J.; Contreras-Caceres, R., Seeded Growth Synthesis of Gold Nanotriangles: Size Control, SAXS Analysis, and SERS Performance. *ACS Appl. Mater. Interfaces* **2018,** *10* (13), 11152-11163.

143. Song, C. Y.; Yang, B. Y.; Chen, W. Q.; Dou, Y. X.; Yang, Y. J.; Zhou, N.; Wang, L. H., Gold nanoflowers with tunable sheet-like petals: facile synthesis, SERS performances and cell imaging. *J. Mater. Chem. B* **2016,** *4* (44), 7112-7118.

144. Fleger, Y.; Rosenbluh, M., Surface Plasmons and Surface Enhanced Raman Spectra of Aggregated and Alloyed Gold-Silver Nanoparticles. *Res. Lett. Opt.* **2009,** *2009*, 1-5.

145. Fortuni, B.; Inose, T.; Uezono, S.; Toyouchi, S.; Umemoto, K.; Sekine, S.; Fujita, Y.; Ricci, M.; Lu, G.; Masuhara, A.; Hutchison, J. A.; Latterini, L.; Uji-i, H., In situ synthesis of Au-shelled Ag nanoparticles on PDMS for flexible, long-life, and broad spectrum-sensitive SERS substrates. *Chem. Commun.* **2017,** *53* (82), 11298-11301.

146. Panneerselvam, R.; Liu, G. K.; Wang, Y. H.; Liu, J. Y.; Ding, S. Y.; Li, J. F.; Wu, D. Y.; Tian, Z. Q., Surface-enhanced Raman spectroscopy: bottlenecks and future directions. *Chem. Commun.* **2017,** *54* (1), 10-25.

147. Zhou, H.; Li, X.; Wang, L.; Liang, Y.; Jialading, A.; Wang, Z.; Zhang, J. J. R. i. A. C., Application of SERS quantitative analysis method in food safety detection. *Rev Anal Chem* **2021,** *40* (1), 173-186.

148. Li, P.; Long, F.; Chen, W.; Chen, J.; Chu, P. K.; Wang, H., Fundamentals and applications of surface-enhanced Raman spectroscopy–based biosensors. *Curr. Opin. Biomed. Eng.* **2020,** *13*, 51-59.

149. Zheng, X. S.; Hu, P.; Cui, Y.; Zong, C.; Feng, J. M.; Wang, X.; Ren, B., BSA-coated nanoparticles for improved SERS-based intracellular pH sensing. *Anal. Chem.* **2014,** *86* (24), 12250-7.

150. Qi, J.; Zeng, J.; Zhao, F.; Lin, S. H.; Raja, B.; Strych, U.; Willson, R. C.; Shih, W. C., Label-free, in situ SERS monitoring of individual DNA hybridization in microfluidics. *Nanoscale* **2014,** *6* (15), 8521-6.

151. Zhang, L.; Zhao, Q.; Jiang, Z.; Shen, J.; Wu, W.; Liu, X.; Fan, Q.; Huang, W., Recent Progress of SERS Nanoprobe for pH Detecting and its Application in Biological Imaging. *Biosensors* **2021**, 11(8), 282.

152. Zong, C.; Xu, M.; Xu, L.-J.; Wei, T.; Ma, X.; Zheng, X.-S.; Hu, R.; Ren, B., Surface-Enhanced Raman Spectroscopy for Bioanalysis: Reliability and Challenges. *Chem. Rev.* **2018,** *118* (10), 4946-4980.

153. Chen, Y.; Zhang, Y.; Pan, F.; Liu, J.; Wang, K.; Zhang, C.; Cheng, S.; Lu, L.; Zhang, W.; Zhang, Z.; Zhi, X.; Zhang, Q.; Alfranca, G.; de la Fuente, J. M.; Chen, D.; Cui, D., Breath Analysis Based on Surface-Enhanced Raman Scattering Sensors Distinguishes Early and Advanced Gastric Cancer Patients from Healthy Persons. *ACS Nano* **2016,** *10* (9), 8169-79.

154. Qiao, X.; Su, B.; Liu, C.; Song, Q.; Luo, D.; Mo, G.; Wang, T., Selective Surface Enhanced Raman Scattering for Quantitative Detection of Lung Cancer Biomarkers in Superparticle@MOF Structure. *Adv. Mater.* **2018,** *30* (5).

155. Chen, Y.; Cheng, S.; Zhang, A.; Song, J.; Chang, J.; Wang, K.; Zhang, Y.; Li, S.; Liu, H.; Alfranca, G. J. J. o. b. n., Salivary analysis based on surface enhanced Raman scattering sensors distinguishes early and advanced gastric cancer patients from healthy persons. *J Biomed Nanotechnol* **2018,** *14* (10), 1773-1784.

156. Lu, G.; De Keersmaecker, H.; Su, L.; Kenens, B.; Rocha, S.; Fron, E.; Chen, C.; Van Dorpe, P.; Mizuno, H.; Hofkens, J.; Hutchison, J. A.; Uji-i, H., Live-Cell SERS Endoscopy Using Plasmonic Nanowire Waveguides. *Adv. Mater.* **2014,** *26* (30), 5124-5128.

157. Talley, C. E.; Jusinski, L.; Hollars, C. W.; Lane, S. M.; Huser, T., Intracellular pH sensors based on surface-enhanced raman scattering. *Anal. Chem.* **2004,** *76* (23), 7064-8.

158. Kneipp, J.; Kneipp, H.; Wittig, B.; Kneipp, K., Following the Dynamics of pH in Endosomes of Live Cells with SERS Nanosensors. *J. Phys. Chem. C* **2010,** *114* (16), 7421-7426.

159. Zhang, Z.; Bando, K.; Mochizuki, K.; Taguchi, A.; Fujita, K.; Kawata, S., Quantitative Evaluation of Surface-Enhanced Raman Scattering Nanoparticles for Intracellular pH Sensing at a Single Particle Level. *Anal. Chem.* **2019,** *91* (5), 3254-3262.

160. Bando, K.; Zhang, Z.; Graham, D.; Faulds, K.; Fujita, K.; Kawata, S., Dynamic pH measurements of intracellular pathways using nano-plasmonic assemblies. *Analyst* **2020,** *145* (17), 5768-5775.

161. Guo, J.; Sesena Rubfiaro, A.; Lai, Y.; Moscoso, J.; Chen, F.; Liu, Y.; Wang, X.; He, J., Dynamic single-cell intracellular pH sensing using a SERS-active nanopipette. *Analyst* **2020,** *145* (14), 4852-4859.

162. Nowak-Lovato, K. L.; Wilson, B. S.; Rector, K. D., SERS nanosensors that report pH of endocytic compartments during FcepsilonRI transit. *Anal. Bioanal. Chem.* **2010,** *398* (5), 2019-29.

163. Nowak-Lovato, K. L.; Rector, K. D., Targeted surface-enhanced Raman scattering nanosensors for whole-cell pH imagery. *Appl. Spectrosc.* **2009,** *63* (4), 387-95.

164. Zheng, X. S.; Zong, C.; Wang, X.; Ren, B., Cell-Penetrating Peptide Conjugated SERS Nanosensor for in Situ Intracellular pH Imaging of Single Living Cells during Cell Cycle. *Anal. Chem.* **2019,** *91* (13), 8383-8389.

165. Shen, Y.; Liang, L.; Zhang, S.; Huang, D.; Zhang, J.; Xu, S.; Liang, C.; Xu, W., Organelle-targeting surface-enhanced Raman scattering (SERS) nanosensors for subcellular pH sensing. *Nanoscale* **2018,** *10* (4), 1622-1630.

166. Zong, S.; Wang, Z.; Yang, J.; Cui, Y., Intracellular pH sensing using p-aminothiophenol functionalized gold nanorods with low cytotoxicity. *Anal. Chem.* **2011,** *83* (11), 4178-83.

167. Kneipp, J.; Kneipp, H.; Wittig, B.; Kneipp, K., One- and two-photon excited optical ph probing for cells using surface-enhanced Raman and hyper-Raman nanosensors. *Nano Lett.* **2007,** *7* (9), 2819-23.

168. Luo, R.; Li, Y.; Zhou, Q.; Zheng, J.; Ma, D.; Tang, P.; Yang, S.; Qing, Z.; Yang, R., SERS monitoring the dynamics of local pH in lysosome of living cells during photothermal therapy. *Analyst* **2016,** *141* (11), 3224-7.

169. Zhao, X.; Campbell, S.; Wallace, G. Q.; Claing, A.; Bazuin, C. G.; Masson, J.-F., Branched Au Nanoparticles on Nanofibers for Surface-Enhanced Raman Scattering Sensing of Intracellular pH and Extracellular pH Gradients. *ACS Sens.* **2020,** 5(7): 2155-2167.

170. Wang, F.; Widejko, R. G.; Yang, Z.; Nguyen, K. T.; Chen, H.; Fernando, L. P.; Christensen, K. A.; Anker, J. N., Surface-enhanced raman scattering detection of pH with silica-encapsulated 4-mercaptobenzoic acid-functionalized silver nanoparticles. *Anal. Chem.* **2012,** *84* (18), 8013-9.

171. Sun, F.; Zhang, P.; Bai, T.; David Galvan, D.; Hung, H. C.; Zhou, N.; Jiang, S.; Yu, Q., Functionalized plasmonic nanostructure arrays for direct and accurate mapping extracellular pH of living cells in complex media using SERS. *Biosens. Bioelectron.* **2015,** *73*, 202-207.

172. García-Algar, M.; Tsoutsi, D.; Sanles-Sobrido, M.; Cabot, A.; Izquierdo-Roca, V.; Gil, H. P. R., Subcellular Optical pH Nanoscale Sensor. *ChemistrySelect* **2017,** *2* (26), 8115-8121.

173. Li, S. S.; Zhang, M.; Wang, J. H.; Yang, F.; Kang, B.; Xu, J. J.; Chen, H. Y., Monitoring the Changes of pH in Lysosomes during Autophagy and Apoptosis by Plasmon Enhanced Raman Imaging. *Anal. Chem.* **2019,** *91* (13), 8398-8405.

174. Zhang, Y.; Jimenez de Aberasturi, D.; Henriksen-Lacey, M.; Langer, J.; Liz-Marzan, L. M., Live-Cell Surface-Enhanced Raman Spectroscopy Imaging of Intracellular pH: From Two Dimensions to Three Dimensions. *ACS Sens.* **2020,** *5* (10), 3194-3206.

175. Chen, P.; Wang, Z.; Zong, S.; Chen, H.; Zhu, D.; Zhong, Y.; Cui, Y., A wide range optical pH sensor for living cells using Au@Ag nanoparticles functionalized carbon nanotubes based on SERS signals. *Anal. Bioanal. Chem.* **2014,** *406* (25), 6337-46.

176. Pallaoro, A.; Braun, G. B.; Reich, N. O.; Moskovits, M., Mapping local pH in live cells using encapsulated fluorescent SERS nanotags. *Small* **2010,** *6* (5), 618-22.

177. Puppulin, L.; Hosogi, S.; Sun, H.; Matsuo, K.; Inui, T.; Kumamoto, Y.; Suzaki, T.; Tanaka, H.; Marunaka, Y., Bioconjugation strategy for cell surface labelling with gold nanostructures designed for highly localized pH measurement. *Nat. Commun.* **2018,** *9* (1), 5278.

178. Wei, H.; Willner, M. R.; Marr, L. C.; Vikesland, P. J., Highly stable SERS pH nanoprobes produced by co-solvent controlled AuNP aggregation. *Analyst* **2016,** *141* (17), 5159-69.

179. Wang, J.; Geng, Y.; Shen, Y.; Shi, W.; Xu, W.; Xu, S., SERS-active fiber tip for intracellular and extracellular pH sensing in living single cells. *Sens. Actuators B Chem.* **2019,** *290*, 527-534.

180. Biju, V., Chemical modifications and bioconjugate reactions of nanomaterials for sensing, imaging, drug delivery and therapy. *Chem. Soc. Rev.* **2014,** *43* (3), 744-64.

181. Gonzalez Solveyra, E.; Szleifer, I., What is the role of curvature on the properties of nanomaterials for biomedical applications? *Wiley Interdiscip. Rev. Nanomed. Nanobiotechnol.* **2016,** *8* (3), 334-54.

182. Wang, D.; Nap, R. J.; Lagzi, I.; Kowalczyk, B.; Han, S.; Grzybowski, B. A.; Szleifer, I., How and why nanoparticle's curvature regulates the apparent pKa of the coating ligands. *J. Am. Chem. Soc.* **2011,** *133* (7), 2192-7.

183. Villarreal, E.; Li, G. G.; Zhang, Q.; Fu, X.; Wang, H., Nanoscale Surface Curvature Effects on Ligand-Nanoparticle Interactions: A Plasmon-Enhanced Spectroscopic Study of Thiolated Ligand Adsorption, Desorption, and Exchange on Gold Nanoparticles. *Nano Lett.* **2017,** *17* (7), 4443-4452.

184. Browne, K. P.; Grzybowski, B. A., Controlling the properties of self-assembled monolayers by substrate curvature. *Langmuir* **2011,** *27* (4), 1246-50.

185. Walker, D. A.; Leitsch, E. K.; Nap, R. J.; Szleifer, I.; Grzybowski, B. A., Geometric curvature controls the chemical patchiness and self-assembly of nanoparticles. *Nat. Nanotechnol.* **2013,** *8* (9), 676-81.

186. Remaut, K.; Oorschot, V.; Braeckmans, K.; Klumperman, J.; De Smedt, S. C., Lysosomal capturing of cytoplasmic injected nanoparticles by autophagy: an additional barrier to non viral gene delivery. *J. Control. Release* **2014,** *195*, 29-36.

187. Behzadi, S.; Serpooshan, V.; Tao, W.; Hamaly, M. A.; Alkawareek, M. Y.; Dreaden, E. C.; Brown, D.; Alkilany, A. M.; Farokhzad, O. C.; Mahmoudi, M., Cellular uptake of nanoparticles: journey inside the cell. *Chem. Soc. Rev.* **2017,** *46* (14), 4218-4244.

188. Salatin, S.; Maleki Dizaj, S.; Yari Khosroushahi, A., Effect of the surface modification, size, and shape on cellular uptake of nanoparticles. *Cell Biol. Int.* **2015,** *39* (8), 881-90.

189. Yum, K.; Wang, N.; Yu, M. F., Nanoneedle: a multifunctional tool for biological studies in living cells. *Nanoscale* **2010,** *2* (3), 363-72.

Chapter 2

Low-Cytotoxic Gold-Coated Silver Nanoflowers for Intracellular pH Sensing

The results reported in this chapter are based on the following publication:

Zhang, Q.; Wen, H.; Watanabe, K.; Kotani, I.; Ricci, M.; Fortuni, B.; Dao, A. T. N.; Masuhara, A.; Hirai, K.; Kasai, H.; Inose, T.; Uji-i, H., Low-Cytotoxic Gold-Coated Silver Nanoflowers for Intracellular pH Sensing. ACS Appl. Nano Mater. 2020, 3 (8), 7643-7650.

2.1 Abstract

Intracellular pH affects many biological processes such as apoptosis, proliferation, endocytosis, and multi-drug resistance. In view of this, highly sensitive pH sensing in live cells is essential for understanding biological dynamics. Although surface-enhanced Raman spectroscopy (SERS) using noble metal nanoparticles functionalized with acidic ligands has been proposed for highly sensitive intracellular pH sensing, the dependence of SERS pH sensitivity on nanoparticle morphology has been overlooked. The apparent dissociation constant (pK_a) of acid ligands is known to be sensitive to nanoparticles curvature. Thus, nanoparticle morphology should reflect SERS pH sensitivity. Here, we compared pK_a behaviors and SERS pH sensitivities of nearly spherical isotropic and flower-like anisotropic gold-coated silver nanoparticles (AuAgNPs and AuAgNFs, respectively). We found that the NPs with higher curvature like AuAgNFs show a narrower pH-sensitive range (pH 5 ~ 8) compared to the nearly spherical nanoparticles, providing higher sensitivity to the pH range. Taking advantage of the narrow pH range of AuAgNFs, pH changes are successfully monitored as function of time in cells treated with and without anticancer drugs, respectively. The results indicate that the pH-sensitive range of SERS-sensing can be tailored by controlling nanoparticle morphology. This tunability is a crucial requirement for pH sensing applications in various biological systems.

2.2 Introduction

Intracellular pH reflects the physiological conditions of the cell, giving fundamental information on various cellular processes, such as metabolism, cell growth, proliferation, cytoskeleton polymerization, enzymatic activities, and so on.[1-5] For example, monitoring pH in lysosomes allows us to detect the occurrence of cellular physiological processes such as autophagy and apoptosis.[6, 7] Furthermore, a reversed pH gradient is known to be related to tumorigenesis with cancer cells possessing higher cytosolic pH, lower extracellular pH and a more acidic lysosomal pH than healthy cells.[8-10] Considering that pH provides insights into cell metabolism and disease, local intracellular pH probes are essential for a better understanding of biochemical dynamics.

Several fluorescence-based microscopic techniques, associated with the use of pH-sensitive dyes, have been well-established for intracellular pH measurements and have gained much attention because of being considered as non-invasive and real-time sensing methods.[11, 12] However, their performances are often affected by autofluorescence of cells, photoquenching, or photobleaching. Furthermore, the absolute intracellular pH values can be hardly estimated by monitoring the fluorescence of pH-sensitive dyes. More specifically, the pH sensing via organic dyes relies on the change of fluorescent intensity upon different pH. Simultaneously, the fluorescent intensity is also influenced by the local concentration of the organic dye used, which strongly depends on the cellular compartments. As a consequence, fluorescent intensity-based approaches often do not enable for estimating absolute pH values especially inside cellular compartments.

In this context, the use of surface-enhanced Raman spectroscopy (SERS) has been proposed as an alternative pH sensing.[13] In the SERS-based pH sensing, noble metal nanostructures, such as gold and silver nanoparticles, are functionalized with molecules of which Raman spectrum responds to pH changes upon protonation and deprotonation. Several pH sensitive nanosensors have been used for pH sensing.[14-18] Suitable Raman probes can be selected depending on the monitoring environments; for example, m-cresol can be used around the neutral range[16] and 4-aminothiophenol (4-ATP) is useful for wider range pH sensing.[18] Among those, 4-mercaptobenzonic acid (4-MBA) has been one of the most widely used pH-sensing Raman reporter based on its carboxylic group. SERS spectrum variations upon the degree of protonation and deprotonation of its acidic ligands provide a means to estimate pH values of

surrounding media. The high reliability and accuracy of this method are associated with the use of a calibration curve constructed in advance, which allows to estimate pH values around each nanoparticle. In addition to this, such an approach provides extra advantages, i.e. high sensitivity and selectability of excitation wavelengths from visible to near-infrared (near-IR). The use of near-IR excitation enables negligible interference from biological autofluorescence and a reduced photoquenching or photobleaching effect.[19-21]

SERS spectrum response to pH, however, might depend on the size and morphology of nanoparticles (NPs). The apparent acid dissociation constant (pK_a) of ionizable ligands such as 4-MBA immobilized on NPs have been reported to be sensitive to the curvature of NPs.[22, 23] D. Wang et al. reported that lower pK_a of acidic ligands was expected on higher curvature due to weaker electrostatic repulsions between COO^- groups of 11-mercaptoundeca-noic acid (MUA).[22] This suggests that the range and sensitivity of SERS-based pH sensing can be tailored by controlling the size and morphology of NPs. In order to enhance SERS sensitivity, various anisotropic metal NPs like nanostars have been explored for pH sensing. Such NPs with complex morphology are expected to exhibit complex pK_a behavior. D. A. Walker et al. reported that a single chemical species show two equivalence points in their pH titration curves and different apparent pK_a values whether adsorbed on gold nano-dumbbells or nanorods, respectively.[23] Despite these findings, the relationship between such pK_a behavior and SERS response to pH remains unclear.

Another aspect to be taken into account, especially for cellular applications, is the cytotoxicity of metal NPs. Because a chemical enhancement is required, silver nanoparticles are usually a better candidate than gold for the pH sensing.[24,25] Ag ions released from silver nanoparticles, however, are highly cytotoxic,[26, 27] and can induce apoptosis, which likely affects the results of an intercellular pH sensing. The apoptotic process, indeed, acidifies the cytosol and the increases the pH inside lysosomes.[6, 28-30] We recently reported that coating silver nanoparticles with thin gold layers retains the visible wavelength sensitivity and the chemical enhancement of silver nanoparticles, while increases the oxidation resistance.[31] Thus, the gold coating could also reduce the potential cytotoxicity of silver nanoparticles.

In this work, we investigated the relationship between the morphology of gold-coated silver nanoparticles and their SERS activity for pH sensing. We coated nearly spherical and anisotropic flower-like silver nanoparticles with thin gold layers (AuAgNPs and AuAgNFs,

respectively) and functionalized the surface with 4-MBA (Scheme 2.1). 4-MBA was chosen as a pH sensitive Raman reporter in this study to compare it with the previously reported studies.[22, 23] The relation between the change in SERS intensity and the apparent pK_a value of 4-MBA was also evaluated. By carefully analyzing the SERS peak of COO^- carefully, we correlated SERS pH response with titration curves. We also found that anisotropic AuAgNFs could provide more sensitive pH monitoring ability between 5 and 8 compared to nearly spherical AuAgNPs. Taking advantage of this sensitivity, pH sensing inside lysosomes was successfully performed in human lung carcinoma cell line (A549) with and without anticancer drug treatment. In order to exclude any incidence of potential NPs toxicity on the pH sensing results, cytotoxicity tests on A549 cells were also performed. We found that SERS pH-sensitive range and sensitivity can be controlled by choosing nanoparticles with different curvatures. The results reported here are essential to guarantee an appropriate use of SERS in pH sensing applications, especially for in-situ single cell investigation. The application of our AuAgNFs as intracellular pH sensors will promote better understanding of various pH-dependent biological processes.

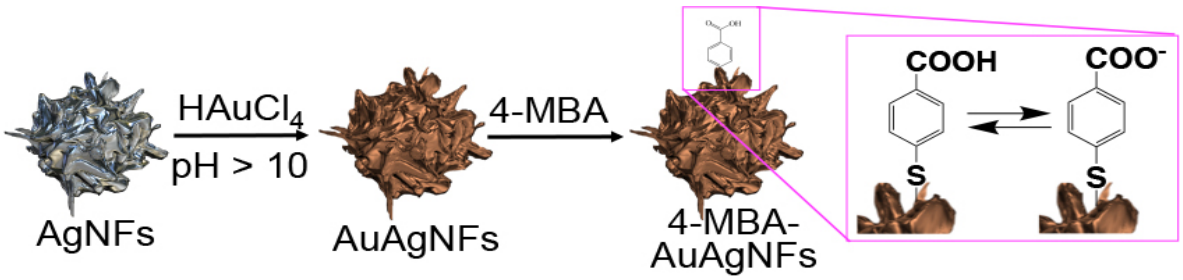

Scheme 2.1. Schematic illustration of the procedure for the preparation of AgNFs, AuAgNFs, and 4-MBA-AuAgNFs.

2.3 Result and discussion

Characterization of AgNPs and AgNFs and Au-coated AgNPs and AgNFs. AgNPs and AgNFs were characterized for size and morphology by means of scanning electron microscopy (SEM) before and after the Au-coating (Figure 2.1) Nearly spherical nanoparticles with small protrusions (AgNPs) have been obtained at a lower concentration of Na_3Cit (~ 0.01 mM) (Figure 2.1a), while the same synthesis protocol with higher Na_3Cit concentration (~ 1.4 mM) provided flower-like silver nanoparticles (AgNFs) (Figure 2.1b). The size of these colloids was around 150 - 350 nm in diameter according to the SEM and DLS analyses (Figure 2.1 and Figure 2.A1). Although AgNPs showed a slight aggregation, AgNFs were well dispersed in the suspension.

The colloidal morphology dependence on the Na_3Cit concentration has been already explained in literature.[31-34] According to these studies, before the reduction of silver ions, the Ag^+– Na_3Cit complexes are formed due to the strong chelating ability of the carboxyl groups, regulating the reduction rate and, therefore, the growth of the nanoparticles. When the reducing agent, L(+)-ascorbic acid, was added, reduced silver ions formed Ag^0 crystal nucleus. At the presence of a high concentration of Na_3Cit, the crystal growth occurs anisotropically because Na_3Cit molecules could preferentially adsorb on (111) facet of the silver nanocrystals, resulting in formation of Ag nanoparticles (AgNFs). Instead, with a smaller amount of Na_3Cit, the anisotropic growth is not efficiently induced and the particles spontaneously grow into nearly spherical structures (AgNPs).

Au-coating on both AgNPs and AgNFs was performed by adding $HAuCl_4$ aqueous solution in the presence of L(+)-ascorbic acid. At a high pH, reduction of gold ions by L(+)-ascorbic acid becomes dominant, resulting in gold atom deposition to form a thin gold shell on AgNPs/AgNFs surface instead of galvanic replacement (GR).[35] Thus, in this study, $HAuCl_4$ solution with L(+)-ascorbic acid was adjusted to pH 11. As shown in Figure 2.1c and 2.1d, after the Au deposition, both the AgNPs and AgNFs maintained the original morphologies and sizes, indicating GR did not occur. Note that nanoparticle morphology usually drastically change through GR reaction.[31] To ensure the presence of the Au coating, nanoparticles were treated with 2% H_2O_2 aq (Figure 2.A2). While AgNPs and AgNFs are rapidly oxidized and collapsed (Figure 2.A2e, 2.A2f), AuAgNPs and AuAgNFs remained intact after the treatment as shown in Figure 2.A2g, 2.A2h and Figure 2.A3. In order to confirm the gold deposition and

the consequent formation of a gold layer on AgNPs/AgNFs surfaces, energy dispersive X-ray spectroscopy (EDX) elemental analysis by scanning electron microscopy (SEM) was performed. The EDX mappings of AuAgNPs and AuAgNFs are shown in Figure 2.A4 and 2.A5, respectively, where gold was marked in yellow and silver in green. The contrast between them indicates that only a small amount of gold was deposited on the AgNPs and AgNFs, which agrees with the weak peak of gold element in the EDX spectra (Figure 2.A4d and 2.A5d, respectively). The Scanning transmission electron microscopy (STEM)-EDX mappings of AuAgNP and AuAgNF shown in Figure 2.A6 and Figure 2.A7 demonstrate that most parts of AuAgNP or AuAgNF were successfully covered by thin gold film. The optical properties of these nanoparticles were investigated with extinction spectroscopy (Figure 2.A8). After Au coating, the extinction peak of AgNPs slightly shifted from 480 to 520 nm. On the other hand, the extinction of AuAgNFs increased above 600nm, while peak position around 520nm remained stable. As expected from previously reported results,[31] the extinction spectra show that the gold coating did not drastically affect the nanoparticle optical responses at visible light frequency.

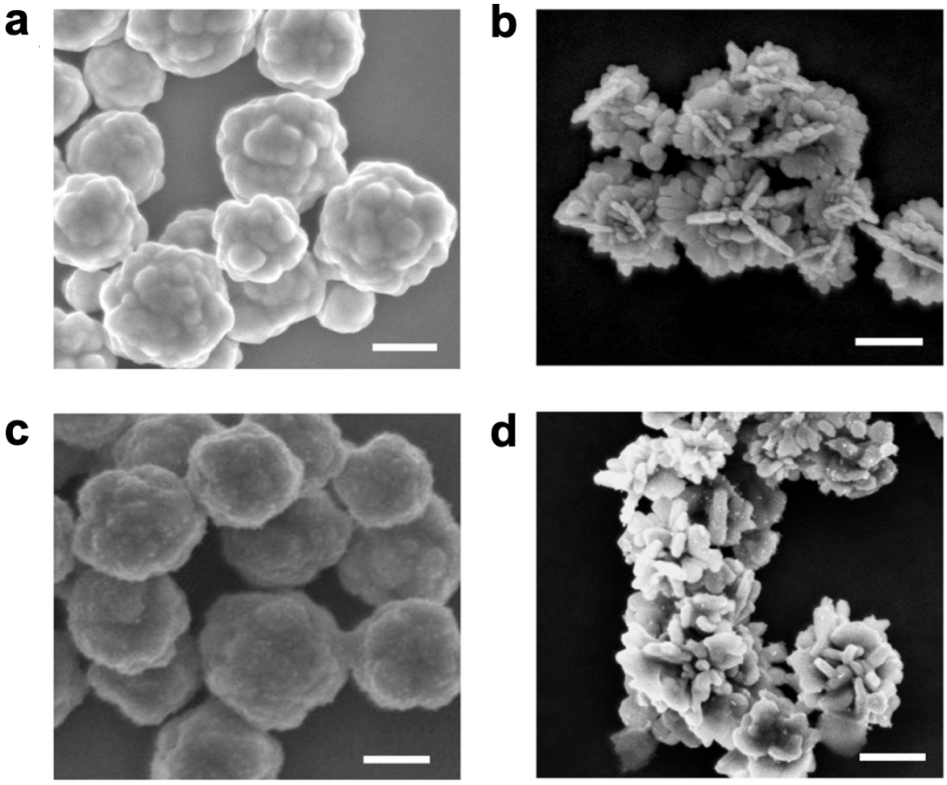

Figure 2.1. SEM images of AgNPs (a), AgNFs (b), AuAgNPs (c) and AuAgNFs (d). (Scale bar: 200 nm)

Titration of AuAgNPs and AuAgNFs. As mentioned in the introduction, pK_a of molecules adsorbed on nanoparticles surface has been proven to be sensitive to the curvature, with higher pK_a on lower curvature and lower pK_a on higher curvature.[22, 23] Based on these findings, a smaller apparent pK_a is expected for AuAgNFs compared to AuAgNPs because of the higher curvature of AuAgNFs, especially at the edges. To verify this hypothesis, the protonation-deprotonation behaviors of 4-MBA on AuAgNPs and AuAgNFs were investigated using potentiometric titration according to the reported method.[23, 36, 37] The titration curves for AuAgNPs and AuAgNFs are displayed in Figure 2.2a and 2.2b, respectively. The pK_a and the Hill coefficient, n, were extracted by fitting the titration curves with the following equation:[36]

$$\alpha_{COOH} = A + (B - A)\frac{1}{1+10^{n(pH-pKa)}} \quad 2.1$$

The apparent pK_a values of 4MBA on AuAgNPs and AuAgNFs were estimated to be ~7.0 and ~6.6, respectively (Table 2.1). In general terms, the lower curvature results in shorter average distance between the COO^- groups in 4-MBA, therefore, generating stronger electrostatic repulsion between 4-MBA molecules. It follows that for a more favorable energetically situation, the acid-base equilibrium is shifted towards the protonated state 4-MBA, increasing the apparent pK_a. Accordingly, the lower apparent pK_a estimated for AuAgNFs (~ 6.6) can be associated with the larger curvature at the edges of AuAgNFs, while the higher pK_a found on AuAgNPs (~ 7.0) reflects their lower curvature. The Hill coefficient, n, on AuAgNPs and AuAgNFs was estimated to be 0.24 and 0.81, respectively. This difference in n can be also associated with different interaction degree between the 4-MBA ligands (Table 2.1). The smaller n value on AuAgNPs indicates the stronger interaction between 4-MBA molecules than that on AuAgNFs, being consistent with the curvature dependence.

The titration curve featured complex and different protonation-deprotonation behavior on AuAgNFs compared to that on AuAgNPs. The nearly spherical AuAgNPs showed only one equivalence point in the pH titration curve (Figure 2.2a, 2.2c), while the titration curve for AuAgNFs displayed two equivalence points (Figure 2.2b, 2.2d). On AuAgNFs, acidic carboxyl groups experience two different curvatures at the flat and edge areas of NFs (Figure 2.2b). The equivalence point was obtained according to the following:

$$0 = \frac{\mathrm{d(dpH/dv)}}{\mathrm{dv}} \quad 2.2$$

The acidic carboxyl groups at the flat regions of NFs will be protonated first until reaching the first equivalence point (Eq1) (pH ~ 7.5). Further addition of HCl protonates the acidic carboxyl group at the tip edge until the second equivalence point (Eq2) (pH 5.2). At this step, all carboxyl groups will be protonated, resulting in a pH value decrease upon further addition of an excess amount of HCl. The observed two Eqs can be explained by taking into account the structure of NFs. The stronger electrostatic repulsions between 4-MBA molecules on the flat region of the NFs likely lead to the first equivalence point at pH ~ 7.5, while the second equivalence point at pH 5.2 could be attributed to a weak repulsion at the edges of NFs. The pH sensitivity on the negative curvature on the NFs is expected to be much lower than that of on the higher curvature and flat areas due to the steric hindrance and the electrostatic repulsion between COO^- groups. Therefore, NFs showed only Eq1 and Eq2 in Figure 2.2d.

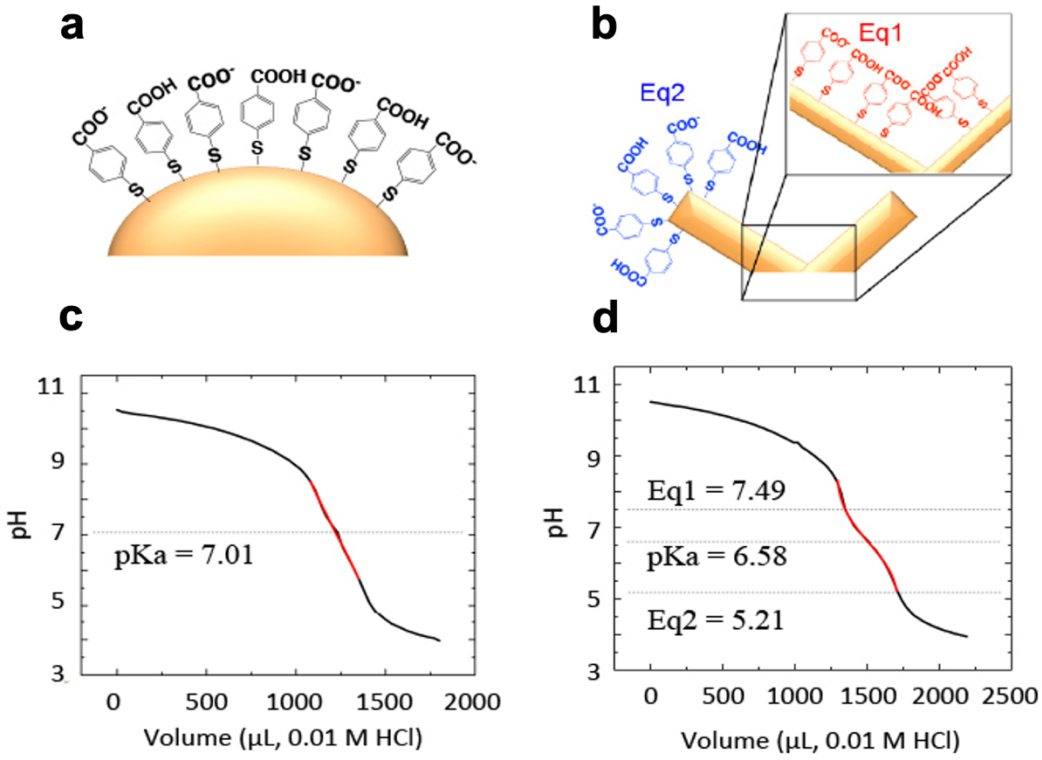

Figure 2.2. The mean curvature of the surface of 4-MBA-AuAgNPs (a) and 4-MBA-AuAgNFs (b). Titration curves in H_2O of 4-MBA-AuAgNPs (c) and 4-MBA-AuAgNFs (d) in H_2O. pK_a values were extracted from the titration data by fitting with the Hill equation (equation 2.1) (red lines).

Table 2.1. The pK_a values and Hill coefficients (n) of 4-MBA on AuAgNFs and AuAgNPs

	pK_a values	Hill coefficient n
4-MBA on AuAgNPs	7.01	0.24
4-MBA on AuAgNFs	6.58	0.81

Calibration for SERS pH sensing. SERS-based pH sensing relies on the dependency of the Raman peak intensity of carboxylate upon pH changes of surrounding media.[19] Since the different pK_a values would affect the pH dependence of SERS intensity, calibration curves needs to be extracted for both types of nanostructures in order to accurately estimate the pH. Figure 2.3a and 2.3b show SERS spectra of 4-MBA on AuAgNPs and AuAgNFs, respectively, at pH ranging from 4 to 11 (SERS peak assignment and the enhancement factors are shown in the Appendix). Several SERS peaks related to carboxylate of 4-MBA are visible in the SERS spectra; C–COOH stretching mode at 802 cm^{-1}, COO^- bending mode at 840 cm^{-1}, COO^- stretching mode at 1400 cm^{-1}, and CO stretching mode at 1703 cm^{-1}.[38, 39] Among them, the COO^- stretching band at 1400 cm^{-1} is the most sensitive to pH values. The intensity of the broad COO^- stretching band (1400 cm^{-1}) was much lower than that of the CO stretching mode (1703 cm^{-1}) at pH 4.0, indicating that a small number of carboxylate ions were formed. The intensity of the broad COO^- stretching mode increased at elevated pH, while the CO stretching intensity decreased because of increased carboxylate groups formation. In addition to the intensity increment, the COO^- stretching band shifted to the higher wavenumbers as pH increased. This shift can be attributed either to hydrogen bonding of 4-MBA or to the interaction between carboxylate groups and hydrogen atoms.[13, 40] Furthermore, it is worth to note that the COO^- stretching band consisted of one peak at low pH value (Figure 2.3c), while two peaks at 1370 ~ 1380 cm^{-1} and 1420 cm^{-1} were clearly observed at high pH value (typically above pH 6.5) (Figure 2.3d). These peaks have been attributed to surface-bound COO^- groups and unbinding carboxylate groups of the more vertically oriented 4-MBA molecules, respectively.[38, 41]

For a more in-depth investigation of the peak intensity changes towards SERS-based pH calibration, the SERS peak of COO^- stretching mode was carefully analyzed. The intensity of the SERS band around 1400 cm^{-1} was fitted either with one component at low pH (peak at 1400 cm^{-1}) (Figure 2.3c) or with two components Gaussian function at high pH (peak at 1370-1380 cm^{-1} and 1420 cm^{-1}) (Figure 2.3d), respectively. The maximum peak intensities are denoted as

I_{max} in this study. In case that two components were found, the intensity at 1370-1380 cm^{-1} and at 1420 cm^{-1} are indicated as $I_{2\text{-}1}$ and $I_{2\text{-}2}$, respectively (see Figure 2.3d).

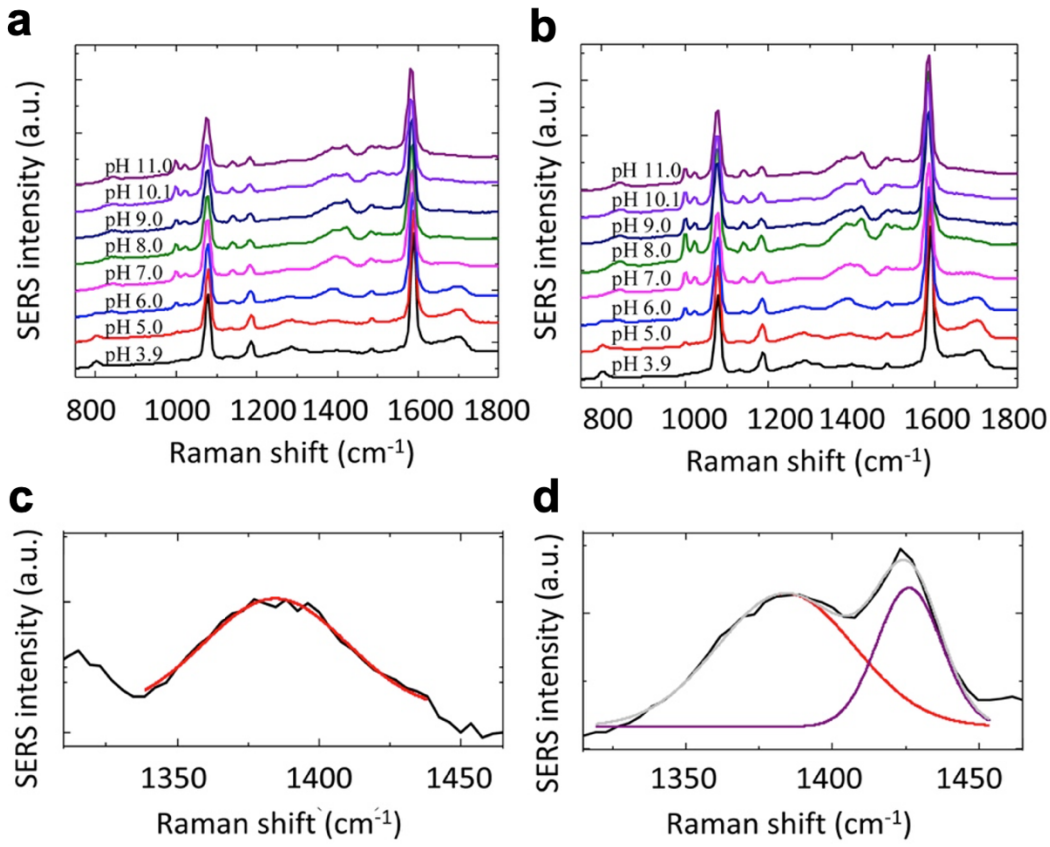

Figure 2.3. SERS spectra of 4-MBA-AuAgNPs (a) and 4-MBA-AuAgNFs (b) in PBS solutions at pH values ranging from 3.9 to 11.0. Curve fitting to determine peak intensities of COO^- stretching: with one component at 1400 cm^{-1} at low pH (c) and two components at 1370-1380 cm^{-1} and 1420 cm^{-1} at high pH (d).

Averaged I_{max}, $I_{2\text{-}1}$, and $I_{2\text{-}2}$ for AuAgNPs and AuAgNFs at each pH are plotted in Figure 2.4. The intensities were normalized based on the peak intensity of the pH-insensitive benzene ring breathing mode at 1079 cm^{-1} (I_{1079} estimated by fitting the Raman peak with Lorentzian function). The calibration curves originated from I_{max} / I_{1079} show different behavior for AuAgNPs (Figure 2.4a) and AuAgNFs (Figure 2.4b). The curve of AuAgNFs (slope of 0.1) was clearly steeper than that of AuAgNPs (slope of 0.06), suggesting a higher sensitivity for AuAgNFs at the pH ranging from 5.0 to 8.0, and a broader but less sensing availability for AuAgNPs. The middle point (at 50% value of the sigmoid function) of the curves for AuAgNPs and AuAgNFs were found at pH 5.5 and 5.9, respectively. In the same way, the other two

calibration curves were made using $I_{2\text{-}1}$ (Figure 2.4c-d) and $I_{2\text{-}2}$ (Figure 2.4e-f). The ratio $I_{2\text{-}1}$ / I_{1079} showed a similar trend as that of I_{max} / I_{1079}, but the middle point for AuAgNFs was as slightly lower as pH 5.6. The curve for AuAgNPs was too gradual to determine the middle point. The lower middle point of $I_{2\text{-}1}$ / I_{1079} compared to that of I_{max} / I_{1079} for AuAgNFs, $I_{2\text{-}1}$ was likely generated from Eq2 at pH 5.2 found in the titration. It is consistent with the fact that SERS enhancement is much higher due to high localized surface plasmon resonances (LSPRs) at the edge than that at the flat region

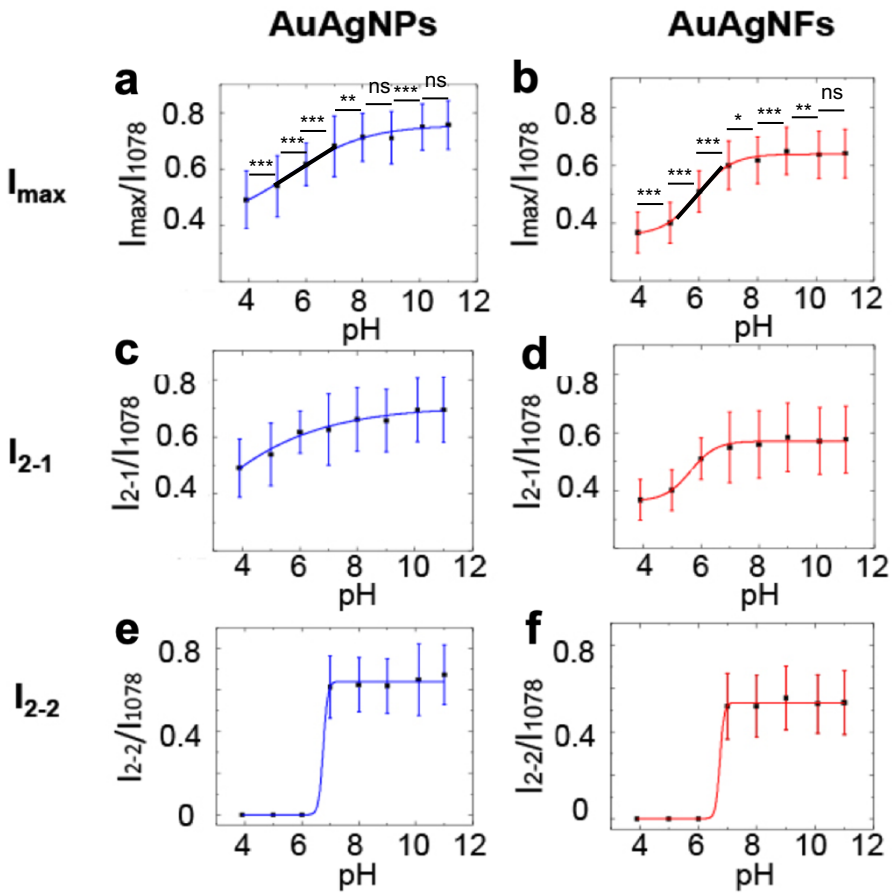

Figure 2.4. pH calibration curves expressing averaged peak intensity ratio between the COO^- stretching mode and the benzene ring breathing mode for 4-MBA-AuAgNPs (a, c, e) and 4-MBA-AuAgNFs (b, d, f). All the curves were fitted with a sigmoid function (solid line). (Error bars indicate mean ± SD, with n=300. *** stands for $p < 0.001$; ** stands for $p < 0.01$; * stands for $p < 0.05$; ns stands for $p > 0.05$)

of AuAgNFs.[42] Thus, SERS signals are dominantly from 4-MBA molecules at the edge rather than on the flat part. Based on its middle point position, the use of $I_{2\text{-}1}$ calibration curve appears

more suitable for SERS pH sensing between 5.0 and 8.0 rather than that with I_{max} (Figure 2.4c and 2.4d). The ratio $I_{2\text{-}2}$ / I_{1079} for both nanoparticles drastically change between pH 6 and 7 and saturate above pH 7.0 (Figure 2.4e and 2.4f). This suggests that the COO^- group of 4-MBA strongly bind on nanoparticle at pH between 6.0 and 7.0. Therefore, this digital behavior of the ratio $I_{2\text{-}2}$ / I_{1079} can be used for ultra-sensitive pH sensing between 6 and 7. To this end, one possible application could be the detection of the pH of Golgi, which, indeed, ranges from 6.0 to 6.7.[2] It is worth mentioning that the added advantage of $I_{2\text{-}2}$ / I_{1079} is insensitive to the nanoparticle morphology.

Cytotoxicity and photocytotoxicity evaluation. The internalization of silver nanoparticles inside living cells is known to induce apoptosis upon release of silver ions from nanoparticle surface.[29,30] The induction of an apoptotic process can, in turn, change the cellular physiological pH, and, consequently, affect the accuracy of pH sensing measurements. Accordingly, a prior evaluation of nanoparticle cytotoxicity is crucial when meant to be used for pH sensing purpose. To this end, A549 cells were incubated with AgNFs and AuAgNFs, as well as those functionalized with a Raman reporter, 4-MBA, for 24 h (0.01 mg/mL of nanoparticles, respectively), and then subjected to viable cell counting (Figure 2.5a). As expected from previously reported results,[31] AgNFs showed high cytotoxicity compared to the Au-coated ones. Both AgNFs and 4-MBA-AgNFs induced a remarkable decrease in viable cell percentages compared to control, as low as ~ 60%. On the other hand, high viabilities over 90% were confirmed upon incubation with AuAgNFs, as well as with 4-MBA-AuAgNFs (Figure 2.5a). The higher cell viability obtained from AuAgNFs incubation is most likely due to suppressed release of silver ions in the presence of gold layers.[43, 44] Considering that nanoparticles will be exposed to light during SERS-based pH measurements, the photocytotoxicity of these nanoparticles was also investigated. As shown in Figure 2.5b, the overall viability percentages seemed not to be affected by light irradiation, with both AuAgNFs and AgNFs, not exhibiting higher cytotoxicity compared to the values obtained in dark. In both cases, the 4-MBA-AuAgNFs exhibited sufficiently low cytotoxicity, resulting suitability for applications in intracellular pH sensing.

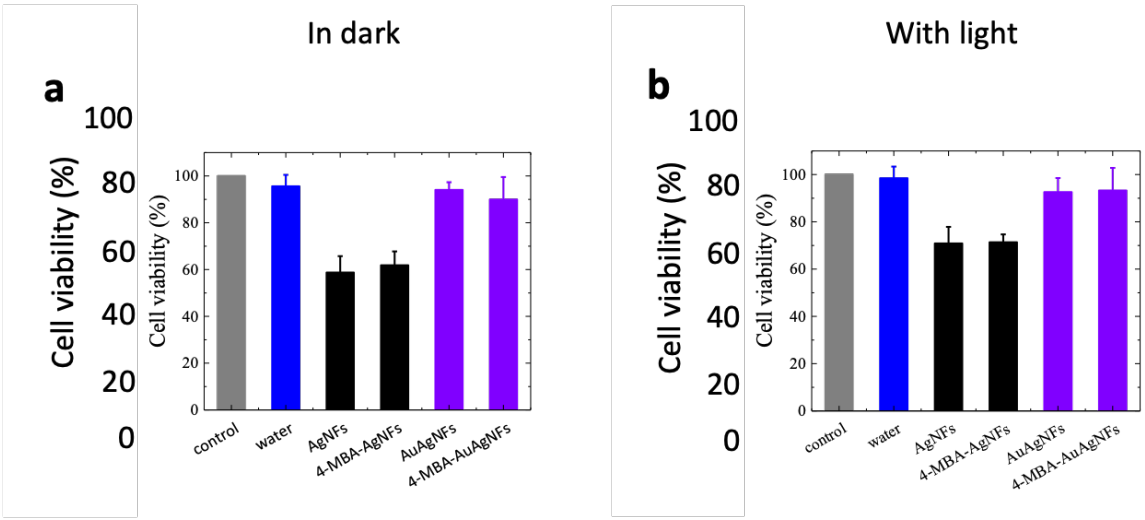

Figure 2.5. Cell viability of A549 cells after 24 h incubation with MilliQ, 10 μL of AgNFs, 4-MBA-AgNFs, AuAgNFs, and 4-MBA-AuAgNFs (~1.0 mg/mL) without (a) and with light irradiation (b), respectively. (Error bars indicate mean ± SD.)

Intracellular pH sensing. In order to demonstrate the application of AuAgNPs and AuAgNFs for highly sensitive pH monitoring inside living cells, A549 cells were incubated with 4-MBA-AuAgNPs or 4-MBA-AuAgNFs for different time intervals between 1 to 24 h. The corresponding SERS spectra of 4-MBA from internalized particles are plotted in Figure 2.A10. The estimated averaged pH values are plotted as a function of time in Figure 2.6. The calibration was performed by using both I_{max} / I_{1079} (Figure 2.6a and 2.6c) and $I_{2\text{-}1}$ / I_{1079} (Figure 2.6b and 2.6d) curves. The averaged pH shows a decreased over time from ~ 7.0 to ~5.0 for both nanoparticles. This decrease can be associated with the migration of AuAgNFs from endosomes to the lysosomes, and might be an evidence of a proper pH sensing. However, the high standard deviations obtained for 4-MBA-AuAgNPs drastically reduce the significance of the pH values estimated (Figure 2.6a and 2.6b). In contrast, the standard deviations of the pH values estimated from 4-MBA-AuAgNFs resulted in being relatively low by using the I_{max} / I_{1079} calibration curve and extremely low, when using the one of $I_{2\text{-}1}$ / I_{1079}. This indicates that very sensitive pH sensing can be performed at the range between pH 5 and 7 (Figure 2.6c and 2.6d). As stated above, calibration with $I_{2\text{-}1}$ / I_{1079} should provide a better estimation of pH although the resulted difference was less than 0.3. Indeed, estimated pH values in live cells were slightly low by the difference of 0.1 ~ 0.2 when calibrated with $I_{2\text{-}1}$ / I_{1079}. To confirm that

NPs are inside cells for intracellular pH sensing, SERS mapping was conducted with larger amount of AuAgNFs incubated for 24 h (Figure 2.A11). The pH range from ~ 7.0 to ~ 5.0 in the SERS mapping was estimated, indicating AuAgNFs are inside endo/lysosome of the cells.

As a comparison, intracellular pH sensing has been performed on A549 cells treated with cisplatin (Figure 2.6e and 2.6f). Cisplatin is an anticancer drug commonly used in chemotherapy, therefore able to efficiently induce cell apoptosis. For both calibrations, the pH values were found to decrease from ~ 7.0 to ~ 6.0 over 24 h. However, this pH decrease was less marked compared to non-treated cells (from ~ 7 to ~ 5). This higher pH found over 24 h in cisplatin-treated cells likely indicates that the cells were undergoing apoptosis. More specifically, when apoptosis occurs, the pH inside lysosomes, where nanoparticles are normally addressed upon internalization, increases due to H^+ ions release.[45, 46] These results indicate that the SERS pH sensing of AuAgNFs, along with the use of the $I_{2\text{-}1}$ / I_{1079} calibration curve, enabled measuring the pH inside lysosomes. Additionally, the pH sensing exhibited a sufficiently high sensitivity to monitor the occurrence of apoptosis processes.

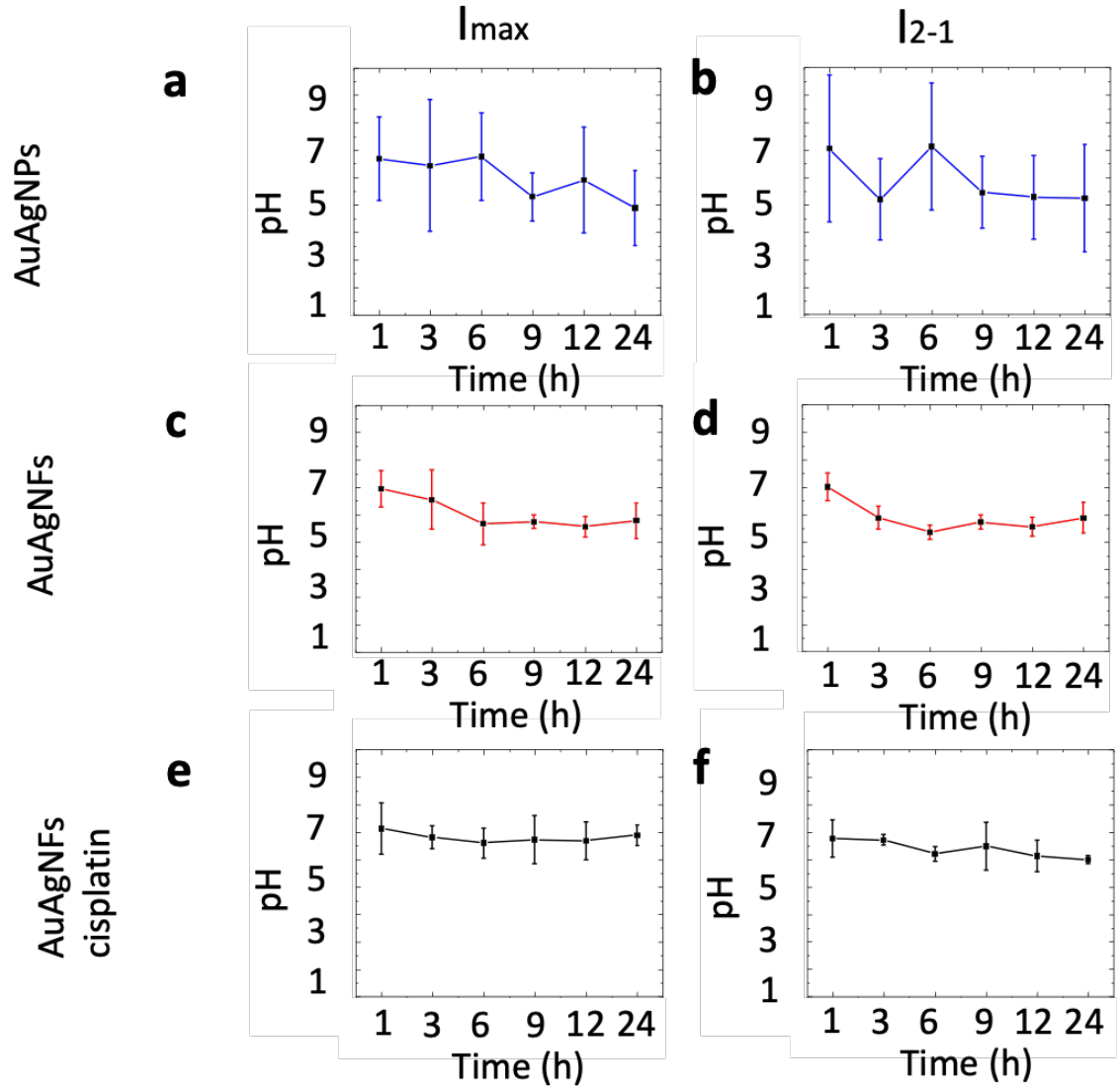

Figure 2.6. Intracellular pH evaluation as function of time measured using 4-MBA-AuAgNPs calibrated with I_{max} / I_{1079} (a) and I_{2-1} / I_{1079} (b), curves measured using 4-MBA-AuAgNFs calibrated with I_{max} / I_{1079} (c) and I_{2-1} / I_{1079} (d) inside non-treated A549 cells, and with I_{max} / I_{1079} (e) and I_{2-1} / I_{1079} (f) inside A549 cells treated with cisplatin. (one spectrum was collected form one spot for one cell. Error bars indicate mean ± SD, with n=10.)

2.4 Conclusion

In this work, we investigated the correlation between the apparent pK_a behavior of 4-MBA and the SERS intensity change of COO^- stretching mode upon pH change. As pK_a depends on nanoparticle curvature, we compared the pH response on nearly spherical and flower-like anisotropic nanoparticles. As expected, anisotropic AuAgNFs featured two equivalence points, while nearly spherical AuAgNPs showed one in their bulk pH titrations. In contrast, in SERS-based pH calibration, only one equivalence point was found for both particles. Interestingly, the value of pH at one of the equivalence points for AuAgNFs agreed with SERS-based pH calibration, which we have attributed to the SERS detection of the protonation-deprotonation process of the acidic ligands at the edges of AuAgNFs. In addition to this, we analyzed the pH-dependence of the COO^- stretching SERS peak, consisting of one broad component at low pH (1370 ~ 1380 cm^{-1}) and an additional relatively sharp component at high pH (1420 cm^{-1}). We found that SERS pH calibration curve from the peak around 1370 ~ 1380 cm^{-1} provided the higher sensitivity to pH change. Viability tests revealed that the Au coating on AgNFs drastically reduces their cytotoxicity, as well as their photocytotoxicity, while keeping high chemical enhancement in SERS. Taking the advantage of the high pH sensitivity obtained from 4-MBA-AuAgNFs, we have successfully performed pH sensing measurements inside lysosomes of A549 cells, being able to detect apoptosis process under anticancer drug treatment.

2.5 Experiment

Reagents. Silver nitrate ($AgNO_3$), ethylene glycol (anhydrous, 99.8%), and gold(III) chloride hydrate ($HAuCl_4$) were purchased from SIGMA-ALDRICH (Japan). Ethanol, trisodium citrate dehydrate (Na_3Cit), L(+)-ascorbic acid, and sodium hydroxide (NaOH) were purchased from FUJIFILM Wako Pure Chemical Corporation. 4-MBA was purchased from Tokyo Chemical Industry Co., Ltd. (TCI). All the reagents were used as received without further purification.

Synthesis of Silver Nano-Flower Particles (AgNFs) and Silver Nanoparticles (AgNPs). The AgNFs and AgNPs were synthesized according to the reported method. Small modifications were performed for obtaining a better dispersity in suspension.[31-33] The synthesis of AgNFs was performed by adding 0.2 mL of 0.1 M $AgNO_3$ in ethylene glycol and 2.0 mL of 1.36mM Na_3Cit solution in 10.0 mL of MilliQ water (18 MΩcm, Milli-Q System, Millipore) and stirring for 5 minutes at room temperature. Then, 0.8 mL of 0.1 M NaOH and 1.0 mL of 0.1 M L(+)-ascorbic acid were added and stirred for further 15 minutes at room temperature. After adding the L(+)-ascorbic acid, the reaction solution turned into blue-black. The AgNFs were collected by centrifugation washing for three times at 5000 rpm. The synthesis of AgNPs was performed similarly except for the use of less concentration of Na_3Cit (0.013 mM).

Gold coating of AgNFs (AuAgNFs) and AgNPs (AuAgNPs). The Au coating was performed according to the reported method with modification.[31, 35] 0.1 mL of a mixed solution prepared from 0.5 mL of 0.5 M NaOH and 1.0 mL of 0.1 M L(+)-ascorbic acid was added to 0.8 mL of AgNFs or AgNPs dispersed solution (0.2 mg/mL). Then 0.1 mL of 1.0 mM $HAuCl_4$ solution was added and stirred for 1 h at room temperature. The excess gold ions were removed by centrifugation at 5000 rpm for three times.

Functionalization of AuAgNFs or AuAgNPs with 4-MBA 0.1 mL of 2.0 mM 4-MBA in ethanol was added to 0.9 mL of AuAgNFs or AuAgNPs in ethanol and stirred overnight. Functionalized nanoparticles were collected by three centrifugations at 5000 rpm.

Characterization. The morphology of nanoparticles was characterized with scanning electron microscopy (SEM, JEOL JSM-6700FT at 5.0 kV), and scanning transmission electron microscopy (STEM, HITACHI HD-2000 equipped with energy dispersive X-ray spectroscopy (EDX) with acceleration voltage of 200 kV). The particle size and dispersity in suspension were analyzed by dynamic light scattering (DLS) on Delsa Nano HC (Beckman Coulter).

Raman spectroscopy were conducted using an inverted optical microscope (TiU, Nikon) equipped with a piezoelectric sample stage. Continuous wave 532 nm laser light was reflected by a dichroic mirror (Z532RDC, Chroma) and was then focused onto the sample by an objective lens (PlanApo x60, N.A. 0.95, Nikon). Raman scattering light from the sample was collected by the same objective and was guided to the spectrograph (iHR320, Horiba) equipped with a CCD detector (Newton 920P, Andor) after passing through a confocal pinhole and longpass filters (BLP01-532, Semrock). The laser power was 0.326 mW, and the accumulation time was 1 second. Extinction spectra of colloidal solution was measured with UV-VIS spectrum (V-750, HITACH).

Potentiometric Titration. The pH of the 4-MBA-AuAgNFs and 4-MBA-AuAgNPs solutions, individually, were measured using a LAQUAact pH meter with HORIBA 9625 electrode. The pH meter was calibrated using pH 4.0, 7.0, and 9.9 H_2O-based standard buffer solutions. For the titration, the pH of the colloidal solutions was adjusted to basic (pH > 10.5) by adding NaOH (1 M). The samples were then titrated by using HCl (0.01 M).

SERS pH calibration curve. SERS pH calibration for AuAgNFs and AuAgNPs were performed in PBS buffer solution ranging over pH 3.9–11.0. AuAgNFs or AuAgNPs were first dropped on a glass coverslip and immersed into each pH solution. Afterwards, SERS spectra on both NPs and NFs, independently, were recorded with 1 s exposure time upon 532 nm excitation.

Cell culture. A549 cells were cultured in 960 mm^2 cell culture dishes at 37 ˚C under humidified 5% CO_2 atmosphere. Once the confluency reached around 80%, the cells were passaged with trypsinization (typically every 2 ~ 3 days). The cells were maintained in Dulbecco's modified Eagle medium (DMEM) containing 10% of FBS, 1% of L-glutammax and 0.1% of gentamicin. For the SERS measurements, the medium was replaced with fresh medium (1 mL) and nanoparticles were added into the culture (~60% of confluency). Then the culture was further incubated at 37 °C under humidified 5% CO_2 for different time intervals.

Cell viability assay. In order to perform viability tests, the cells were seeded in 960 mm^2 cell culture dish and cultured until density reached ~ 5×10^5 cells/cm^2. 10 μL of MilliQ, AgNFs in MilliQ, AuAgNFs in MilliQ, 4-MBA-AgNFs in MilliQ and 4-MBA-AuAgNFs in MilliQ (1 mg/mL) were added into the cell dishes. After incubation at 37 °C under humidified 5% CO_2 for 24 h, the dishes were rinsed with 1.0 mL of PBS (final concentration of nanoparticles is

0.01 mg/mL). In total, 100 μL of cells were mixed with 100 μL of Trypan Blue. Kova® glasstick slides were used for counting the cells inside the grids on the slides with a microscope.

2.6 Appendix

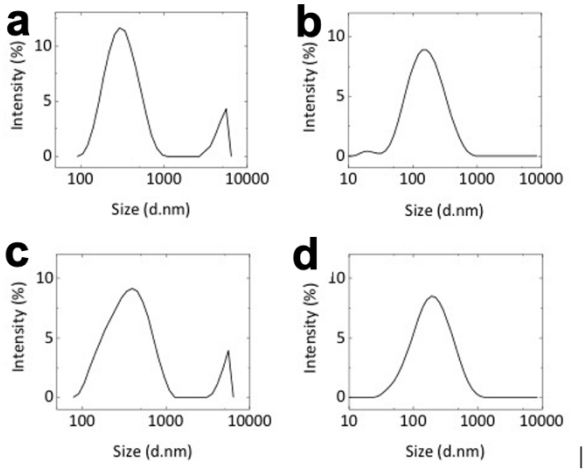

Figure 2.A1. DLS measurements of AgNPs (a, 342.7 nm), AgNFs (b, 131.6 nm), AuAgNPs (c, 357.0 nm) and AuAgNFs (d, 162.7 nm).

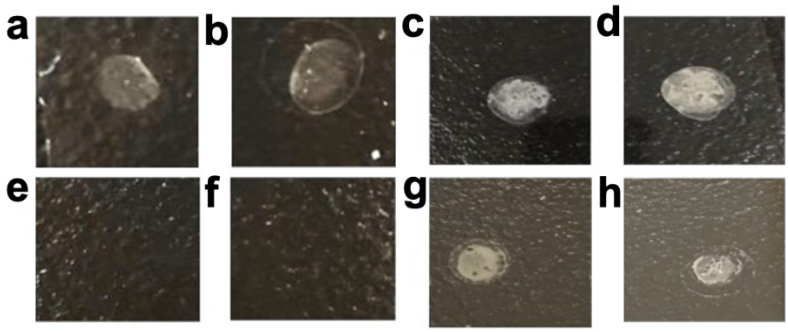

Figure 2.A2. Photographs of AgNPs (a), AgNFs (b), AuAgNPs (c), AuAgNFs (d) on a glass substrate, and AgNPs (e), AgNFs (f), AuAgNPs (g), and AuAgNFs (h) on a glass substrate after treated with 2% of H_2O_2 aqueous solution.

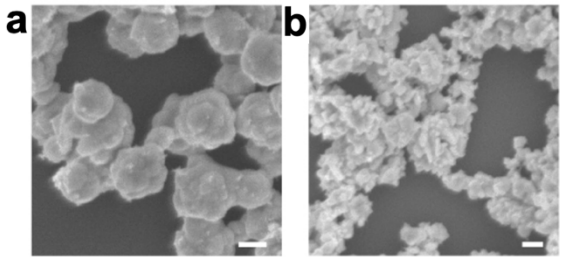

Figure 2.A3. SEM images of AuAgNPs (a), AuAgNFs (b) after treated with 2% of H_2O_2 aqueous.

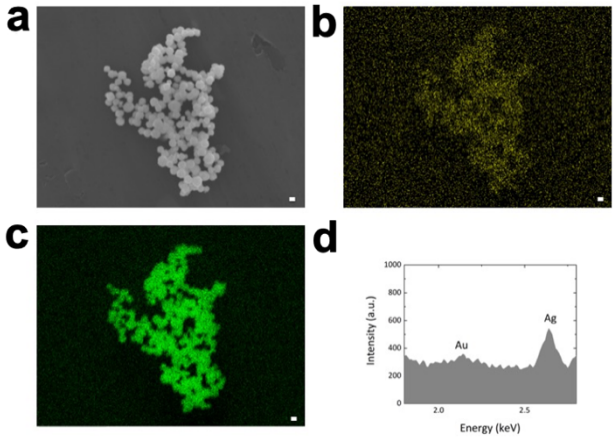

Figure 2.A4. EDX images of AuAgNPs by SEM. SEM image (a), gold elemental mapping (b), silver element mapping (c) and spectrum (d) of EDX elemental analysis. (Scale bar: 200 nm)

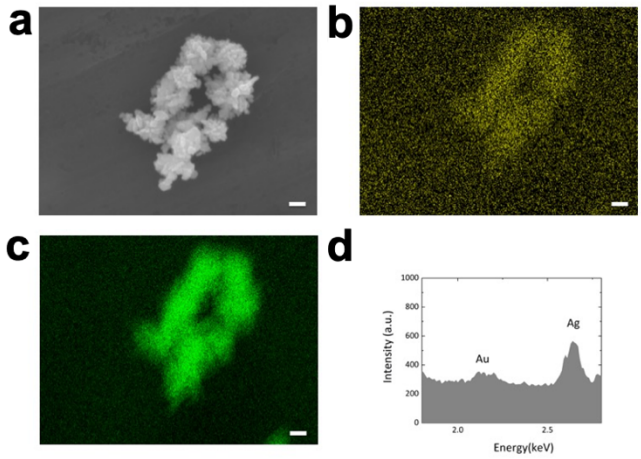

Figure 2.A5. EDX images of AuAgNFs by SEM. SEM image (a), gold elemental mapping (b), silver element mapping (c) and spectrum (d) of EDX elemental analysis. (Scale bar: 200 nm)

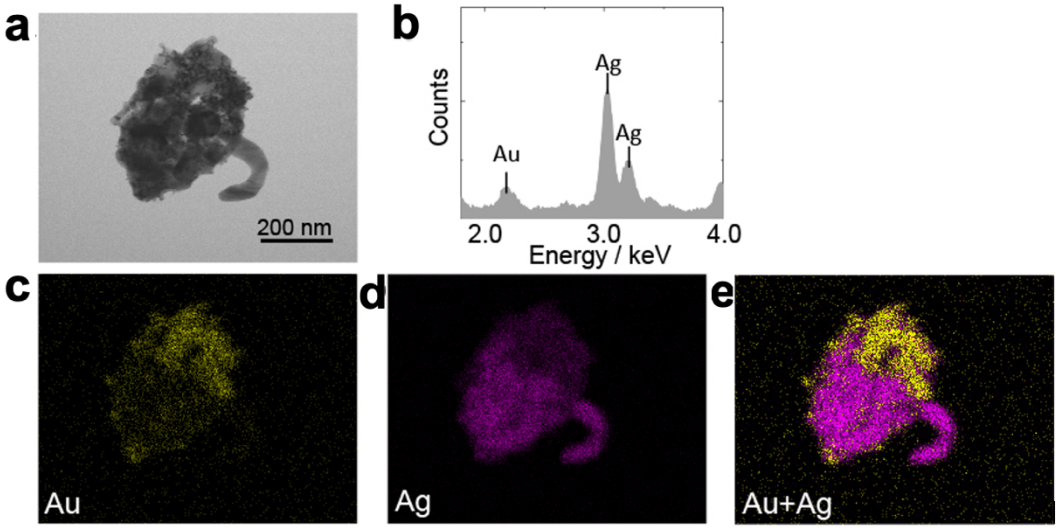

Figure 2.A6. EDX images of AuAgNPs by STEM. STEM image (a), spectrum (b), gold elemental mapping (c), silver element mapping (d) and merged image of individual gold and silver mapping (e).

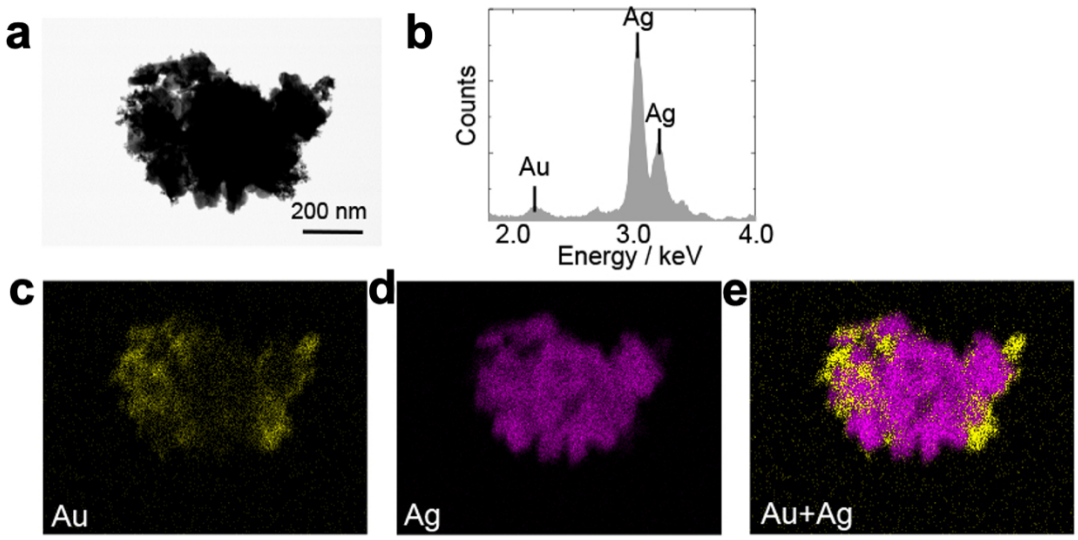

Figure 2.A7. EDX images of AuAgNFs by STEM. STEM image (a), spectrum (b), gold elemental mapping (c), silver element mapping (d) and merged image of individual gold and silver mapping (e).

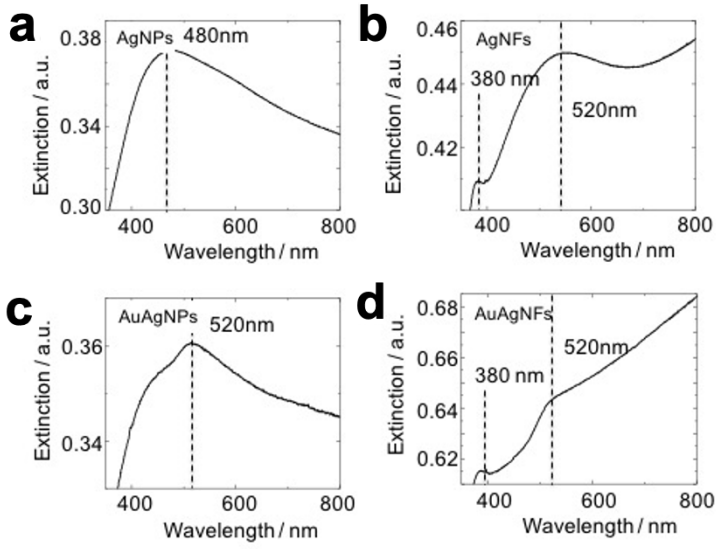

Figure 2.A8. Extinction spectra of AgNPs (a), AgNFs (b), AuAgNPs (c), and AuAgNFs (d) dispersed in water.

SERS measurements of 4-MBA

The pH response from 4-MBA-AuAgNFs or 4-MBA-AuAgNPs was investigated separately by recording SERS spectra in acidic to basic pH levels in PBS buffer solution. SERS spectra at each pH in PBS buffer solution were acquired after immersion of the sample for 10 min.

The intense bands at 1079 cm^{-1} and 1587 cm^{-1} correspond to C–C benzene ring breathing mode of 4-MBA. Both of them were shifted compared to the normal Raman spectrum due to the charge transfer between 4-MBA and metal.[47]

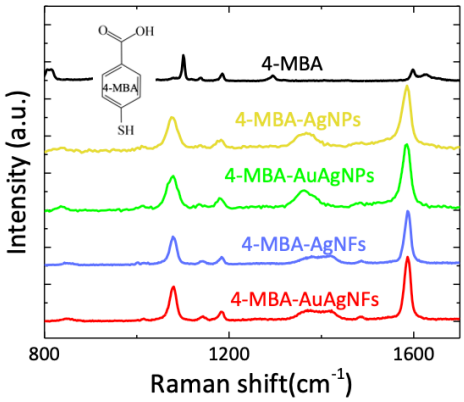

Figure 2.A9. SERS activities of AuAgNFs, AgNFs, AuAgNPs and AgNPs with excitation of 532 nm laser.

Estimation of SERS enhancement factor (EF)

EF was estimated based on the following equation. EF = $(I_{SERS}/N_{SERS})/(I_{bulk}/N_{bulk})$, where I_{SERS} and I_{bulk} are the SERS intensity of 4-MBA on the surface of metal nanoparticles and that of normal Raman scattering from 4-MBA, respectively. N_{SERS} and N_{bulk} are the number of 4-MBA molecules. Assuming full coverage of 4-MBA monolayers on the metal nanoparticles with 0.8 x 0.8 nm^2 spacing per molecule and the diameter of AgNFs and AgNPs were estimated to be 200 x 10^{-9} m. The number of 4-MBA molecules N_{bulk} was 6.07 x 10^8, and the number of 4-MBA molecules N_{SERS} was 4.9 x 10^5. Considering the laser power, EF was calculated for AgNFs: 5.7 x 10^5, AuAgNFs: 2.7 x 10^5, AgNPs: 1.7 x 10^5, AuAgNPs: 1.4 x 10^5.

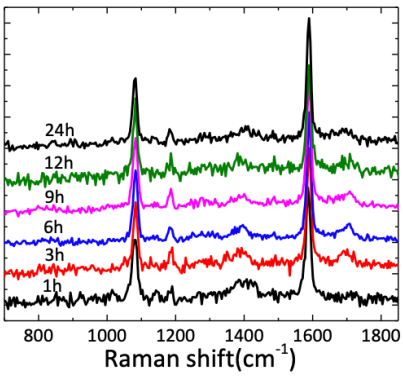

Figure 2.A10. Typical SERS spectra at different time points measured with 4-MBA-AuAgNFs inside A549 cells.

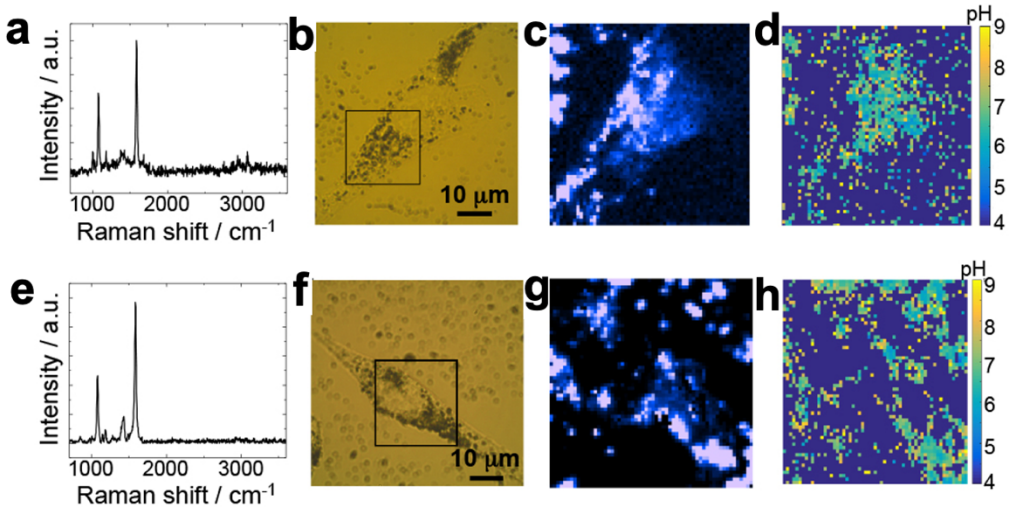

Figure 2.A11. Two set of pH imaging inside single A549 cell. A549 cells incubated with 0.1 mg / mL of AuAgNFs for 24 h. (a) (e) Typical SERS spectra of 4-MBA-AuAgNFs inside single A549 cell. (b) (f) Optica transmission images of cells with 4-MBA-AuAgNFs. (c)(g) SERS mappings constracted with the peak intensity at 1079 cm^{-1}, whcih were scanned marked by black square area in the transmission images in (a) (e). (d), (h) the corresponding pH mapping reconstructed using the peak around 1440 cm^{-1}.

2.7 References

1. Lubman, R. L.; Crandall, E. D., Regulation of intracellular pH in alveolar epithelial cells. *Am. J. Physiol.* **1992,** *262* (1 Pt 1), L1-14.

2. Casey, J. R.; Grinstein, S.; Orlowski, J., Sensors and regulators of intracellular pH. *Nat. Rev. Mol. Cell Biol.* **2010,** *11* (1), 50-61.

3. Shangguan, J.; He, D.; He, X.; Wang, K.; Xu, F.; Liu, J.; Tang, J.; Yang, X.; Huang, J., Label-Free Carbon-Dots-Based Ratiometric Fluorescence pH Nanoprobes for Intracellular pH Sensing. *Anal. Chem.* **2016,** *88* (15), 7837-43.

4. Liu, M.; Hu, M.; Jiang, Q.; Lu, Z.; Huang, Y.; Tan, Y.; Jiang, Q., A novel coumarin derivative as a sensitive probe for tracing intracellular pH changes. *RSC Advances* **2015,** *5* (21), 15778-15783.

5. Geisow, M. J.; Evans, W. H., pH in the endosome. Measurements during pinocytosis and receptor-mediated endocytosis. *Exp. Cell Res.* **1984,** *150* (1), 36-46.

6. Li, S. S.; Zhang, M.; Wang, J. H.; Yang, F.; Kang, B.; Xu, J. J.; Chen, H. Y., Monitoring the Changes of pH in Lysosomes during Autophagy and Apoptosis by Plasmon Enhanced Raman Imaging. *Anal. Chem.* **2019,** *91* (13), 8398-8405.

7. Xu, M.; Ma, X.; Wei, T.; Lu, Z. X.; Ren, B., In Situ Imaging of Live-Cell Extracellular pH during Cell Apoptosis with Surface-Enhanced Raman Spectroscopy. *Anal. Chem.* **2018,** *90* (23), 13922-13928.

8. Zhang, Z.; Bando, K.; Mochizuki, K.; Taguchi, A.; Fujita, K.; Kawata, S., Quantitative Evaluation of Surface-Enhanced Raman Scattering Nanoparticles for Intracellular pH Sensing at a Single Particle Level. *Anal. Chem.* **2019,** *91* (5), 3254-3262.

9. Webb, B. A.; Chimenti, M.; Jacobson, M. P.; Barber, D. L., Dysregulated pH: a perfect storm for cancer progression. *Nat. Rev. Cancer* **2011,** *11* (9), 671-7.

10. Yang, Q.; Wang, H.; Chen, S.; Lan, X.; Xiao, H.; Shi, H.; Ma, Y., Fiber-Optic-Based Micro-Probe Using Hexagonal 1-in-6 Fiber Configuration for Intracellular Single-Cell pH Measurement. *Anal. Chem.* **2015,** *87* (14), 7171-9.

11. Han, J.; Burgess, K., Fluorescent indicators for intracellular pH. *Chem. Rev.* **2010,** *110* (5), 2709-28.

12. Wencel, D.; Abel, T.; McDonagh, C., Optical chemical pH sensors. *Anal. Chem.* **2014,** *86* (1), 15-29.

13. Pallaoro, A.; Braun, G. B.; Reich, N. O.; Moskovits, M., Mapping local pH in live cells using encapsulated fluorescent SERS nanotags. *Small* **2010,** *6* (5), 618-22.

14. Xie, M.; Li, F.; Gu, P.; Wang, F.; Qu, Z.; Li, J.; Wang, L.; Zuo, X.; Zhang, X.; Shen, J. J. C. p., Gold nanoflower-based surface-enhanced Raman probes for pH mapping of tumor cell microenviroment. *Cell Prolif.* **2019,** *52* (4), e12618.

15. Bi, L.; Wang, Y.; Yang, Y.; Li, Y.; Mo, S.; Zheng, Q.; Chen, L., Highly Sensitive and Reproducible SERS Sensor for Biological pH Detection Based on a Uniform Gold Nanorod Array Platform. *ACS Appl. Mater. Interfaces* **2018,** *10* (18), 15381-15387.

16. Zou, X.; Wang, Y.; Liu, W.; Chen, L., m-Cresol purple functionalized surface enhanced Raman scattering paper chips for highly sensitive detection of pH in the neutral pH range. *Analyst* **2017,** *142* (13), 2333-2337.

17. Wang, Y.; Yan, B.; Chen, L., SERS tags: novel optical nanoprobes for bioanalysis. *Chem. Rev.* **2013,** *113* (3), 1391-428.

18. Chen, P.; Wang, Z.; Zong, S.; Chen, H.; Zhu, D.; Zhong, Y.; Cui, Y., A wide range optical pH sensor for living cells using Au@Ag nanoparticles functionalized carbon nanotubes based on SERS signals. *Anal. Bioanal. Chem.* **2014,** *406* (25), 6337-46.

19. Kneipp, J.; Kneipp, H.; Kneipp, K., SERS-a single-molecule and nanoscale tool for bioanalytics. *Chem. Soc. Rev.* **2008,** *37* (5), 1052-60.

20. Lane, L. A.; Qian, X.; Nie, S., SERS Nanoparticles in Medicine: From Label-Free Detection to Spectroscopic Tagging. *Chem. Rev.* **2015,** *115* (19), 10489-529.

21. Cialla-May, D.; Zheng, X. S.; Weber, K.; Popp, J., Recent progress in surface-enhanced Raman spectroscopy for biological and biomedical applications: from cells to clinics. *Chem. Soc. Rev.* **2017,** *46* (13), 3945-3961.

22. Wang, D.; Nap, R. J.; Lagzi, I.; Kowalczyk, B.; Han, S.; Grzybowski, B. A.; Szleifer, I., How and why nanoparticle's curvature regulates the apparent pKa of the coating ligands. *J. Am. Chem. Soc.* **2011,** *133* (7), 2192-7.

23. Walker, D. A.; Leitsch, E. K.; Nap, R. J.; Szleifer, I.; Grzybowski, B. A., Geometric curvature controls the chemical patchiness and self-assembly of nanoparticles. *Nat. Nanotechnol.* **2013,** *8* (9), 676-81.

24. Zong, S.; Wang, Z.; Yang, J.; Cui, Y., Intracellular pH sensing using p-aminothiophenol functionalized gold nanorods with low cytotoxicity. *Anal. Chem.* **2011,** *83* (11), 4178-83.

25. Hill, I. G.; Schwartz, J.; Kahn, A., Metal-dependent charge transfer and chemical interaction at interfaces between 3,4,9,10-perylenetetracarboxylic bisimidazole and gold, silver and magnesium. *Organic Electronics* **2000,** *1* (1), 5-13.

26. AshaRani, P. V.; Low Kah Mun, G.; Hande, M. P.; Valiyaveettil, S., Cytotoxicity and genotoxicity of silver nanoparticles in human cells. *ACS Nano* **2009,** *3* (2), 279-90.

27. Ramachandran, R.; Krishnaraj, C.; Sivakumar, A. S.; Prasannakumar, P.; Abhay Kumar, V. K.; Shim, K. S.; Song, C. G.; Yun, S. I., Anticancer activity of biologically synthesized silver and gold nanoparticles on mouse myoblast cancer cells and their toxicity against embryonic zebrafish. *Mater. Sci. Eng. C* **2017,** *73*, 674-683.

28. Zhu, H.; Fan, J.; Xu, Q.; Li, H.; Wang, J.; Gao, P.; Peng, X., Imaging of lysosomal pH changes with a fluorescent sensor containing a novel lysosome-locating group. *Chem. Commun.* **2012,** *48* (96), 11766-8.

29. Park, E. J.; Yi, J.; Kim, Y.; Choi, K.; Park, K., Silver nanoparticles induce cytotoxicity by a Trojan-horse type mechanism. *Toxicol. In Vitro* **2010,** *24* (3), 872-8.

30. Miura, N.; Shinohara, Y., Cytotoxic effect and apoptosis induction by silver nanoparticles in HeLa cells. *Biochem. Biophys. Res. Commun.* **2009,** *390* (3), 733-7.

31. Fortuni, B.; Inose, T.; Uezono, S.; Toyouchi, S.; Umemoto, K.; Sekine, S.; Fujita, Y.; Ricci, M.; Lu, G.; Masuhara, A.; Hutchison, J. A.; Latterini, L.; Uji-i, H., In situ synthesis of Au-shelled Ag nanoparticles on PDMS for flexible, long-life, and broad spectrum-sensitive SERS substrates. *Chem. Commun.* **2017,** *53* (82), 11298-11301.

32. Hong, L.; Li, Q.; Lin, H.; Li, Y., Synthesis of flower-like silver nanoarchitectures at room temperature. *Mater. Res. Bull.* **2009,** *44* (6), 1201-1204.

33. Zheng, H.; Ni, D.; Yu, Z.; Liang, P.; Chen, H., Fabrication of flower-like silver nanostructures for rapid detection of caffeine using surface enhanced Raman spectroscopy. *Sens. Actuators B Chem.* **2016,** *231*, 423-430.

34. Agnihotri, S.; Mukherji, S.; Mukherji, S., Size-controlled silver nanoparticles synthesized over the range 5–100 nm using the same protocol and their antibacterial efficacy. *RSC Adv.* **2014,** *4* (8), 3974-3983.

35. Yang, Y.; Liu, J.; Fu, Z. W.; Qin, D., Galvanic replacement-free deposition of Au on Ag for core-shell nanocubes with enhanced chemical stability and SERS activity. *J. Am. Chem. Soc.* **2014,** *136* (23), 8153-6.

36. Koivisto, J.; Chen, X.; Donnini, S.; Lahtinen, T.; Häkkinen, H.; Groenhof, G.; Pettersson, M., Acid–Base Properties and Surface Charge Distribution of the Water-Soluble Au102(pMBA)44 Nanocluster. *J. Phys. Chem. C* **2016,** *120* (18), 10041-10050.

37. Charron, G.; Huhn, D.; Perrier, A.; Cordier, L.; Pickett, C. J.; Nann, T.; Parak, W. J., On the use of pH titration to quantitatively characterize colloidal nanoparticles. *Langmuir* **2012,** *28* (43), 15141-9.

38. Ho, C.-H.; Lee, S., SERS and DFT investigation of the adsorption behavior of 4-mercaptobenzoic acid on silver colloids. *Colloids Surf. A Physicochem. Eng. Asp.* **2015,** *474*, 29-35.

39. Wei, H.; Vejerano, E. P.; Leng, W.; Huang, Q.; Willner, M. R.; Marr, L. C.; Vikesland, P. J., Aerosol microdroplets exhibit a stable pH gradient. *Proc. Natl. Acad. Sci. U. S. A.* **2018,** *115* (28), 7272-7277.

40. Sun, F.; Zhang, P.; Bai, T.; David Galvan, D.; Hung, H. C.; Zhou, N.; Jiang, S.; Yu, Q., Functionalized plasmonic nanostructure arrays for direct and accurate mapping extracellular pH of living cells in complex media using SERS. *Biosens. Bioelectron.* **2015,** *73*, 202-207.

41. Puppulin, L.; Hosogi, S.; Sun, H.; Matsuo, K.; Inui, T.; Kumamoto, Y.; Suzaki, T.; Tanaka, H.; Marunaka, Y., Bioconjugation strategy for cell surface labelling with gold nanostructures designed for highly localized pH measurement. *Nat. Commun.* **2018,** *9* (1), 5278.

42. Kim, W.; Kim, N.; Park, J. W.; Kim, Z. H., Nanostar probes for tip-enhanced spectroscopy. *Nanoscale* **2016,** *8* (2), 987-94.

43. Guo, D.; Zhu, L.; Huang, Z.; Zhou, H.; Ge, Y.; Ma, W.; Wu, J.; Zhang, X.; Zhou, X.; Zhang, Y.; Zhao, Y.; Gu, N., Anti-leukemia activity of PVP-coated silver nanoparticles via generation of reactive oxygen species and release of silver ions. *Biomaterials* **2013,** *34* (32), 7884-94.

44. Kittler, S.; Greulich, C.; Diendorf, J.; Köller, M.; Epple, M., Toxicity of Silver Nanoparticles Increases during Storage Because of Slow Dissolution under Release of Silver Ions. *Chem. Mater.* **2010,** *22* (16), 4548-4554.

45. Nilsson, C.; Johansson, U.; Johansson, A. C.; Kagedal, K.; Ollinger, K., Cytosolic acidification and lysosomal alkalinization during TNF-alpha induced apoptosis in U937 cells. *Apoptosis* **2006,** *11* (7), 1149-59.

46. Lagadic-Gossmann, D.; Huc, L.; Lecureur, V., Alterations of intracellular pH homeostasis in apoptosis: origins and roles. *Cell Death Differ.* **2004,** *11* (9), 953-61.

47. Capocefalo, A.; Mammucari, D.; Brasili, F.; Fasolato, C.; Bordi, F.; Postorino, P.; Domenici, F., Exploring the Potentiality of a SERS-Active pH Nano-Biosensor. *Front Chem* **2019,** *7* (413), 413

Chapter 3

Gold-Photodeposited Silver Nanowire Endoscopy for Cytosolic and Nuclear pH Sensing

The results reported in this chapter are based on the following publication:

Zhang, Q.; Inose, T.; Ricci, M.; Li, J.; Tian, Y.; Wen, H.; Toyouchi, S.; Fron, E.; Ngoc Dao, A. T.; Kasai, H.; Rocha, S.; Hirai, K.; Fortuni, B.; Uji-i, H., Gold-Photodeposited Silver Nanowire Endoscopy for Cytosolic and Nuclear pH Sensing. ACS Appl. Nano Mater. 2021.(DOI: 10.1021/acsanm.1c02363)

3.1 Abstract

Intracellular pH variations are a crucial indicator of physiological and pathological conditions. As such, cancer is known to have a direct interplay with pH dysregulation. For investigating pH alterations in cells, metal nanoparticles have been widely used as surface-enhanced Raman spectroscopy (SERS)–based sensors thanks to their high pH sensitivity. However, these SERS probes allow for the detection of pH exclusively at the acidic compartments of the cells (endo-lysosomes), where particles are entrapped after their endocytosis. Consequently, the results obtained with metal nanoparticles are limited, and the relation between the pH values detected in cells and their physiological conditions remains unclear. Herein, we propose an alternative approach based on gold-deposited silver nanowires endoscopy to study cytosolic and nuclear pH variations with high spatio-temporal resolution and sensitivity. The sensing probe was fabricated by depositing gold nanostructures on silver nanowires (Au-dep AgNW) via visible laser light irradiation and modifying the surface with a pH-responsive Raman reporter (4-mercaptobenzoic acid). The high pH sensitivity was demonstrated by immersing the probe in solutions with different pH values (4.4 – 9.3). The endoscopic probe was then inserted either into the nucleus or into the cytosol of a living HeLa cell for site-specific pH sensing. The same experiments were performed after adding a hypoxia mimetic agent ($CoCl_2$) and an anticancer drug (cisplatin), individually. Notably, our probe accurately detected specific pH variations upon these treatments over time. Similar pH alterations were not measured in untreated cells. The results reported in this work clearly show that the Au-dep AgNW endoscopy is a promising powerful tool for pH-sensing applications in biological systems.

3.2 Introduction

Cancer cells feature a reverse pH gradient compared to normal cells, with a slight intracellular alkalization (pH ~ 7.4) and extracellular acidosis (pH ~ 6.8).[1] In general, this pH gradient is considered to play an essential role in cancer progressions, namely in cell proliferation, apoptosis, metabolic adaptation, migration, and drug resistance.[2-6] An in-depth study of cytosolic and nuclear pH variations is therefore crucial for elucidating their influence in cell functions, and in turn, gaining insights into both pH-related pathological processes and the development of new therapeutic strategies. Monitoring how drugs specifically affect the cytosolic pH and verifying if there is an effect on the nuclear pH of cancer cells might provide fundamental information for a deeper understanding of their mechanism of action, and to a further extent, for advancements in the design of next-generation anticancer drugs.

Several strategies have been developed for intracellular pH sensing, such as electrochemistry[7], fluorescence technique[8, 9], and surface-enhanced Raman spectroscopy (SERS)[10-15], and so on. SERS has gained great interest due to its high sensitivity and selectivity, which has been widely used in the detection of molecules inside cells and cellular environments.[11] Intracellular pH as a critical factor has also been detected by SERS, mainly using noble metal nanoparticles (NPs) modified with pH-responsive Raman reporter molecules.[14, 16, 17] However, these SERS probes are usually internalized via endocytosis and trapped in the vesicles, namely the endo-lysosomal system of the cell, focusing on the pH measurements to the inside of these acidic vesicles.[18, 19] Although some strategies, such as electroporation, have been proposed to deliver nanoparticles into the cytosol avoiding endocytosis,[20-22] the delivered NPs might also be captured by cells.[22] In addition, the delivery of the NPs still remains poor spatiotemporal control.

The nano-endoscopy technique is a promising means to interrogate cells at target spots with high spatio-temporal resolution by physically inserting the endoscopy probe into a living cell.[23, 24] Taking advantage of this technique, the strategies using SERS-active glass micropipettes or fiber tips have been proposed for pH sensing.[25-27] These techniques, although highly appealing, suffer from the large structure of the probe originated from the conical shape, which might cause drastic cell deformation and damage during cell penetration.[28] What is more, little is known about the regulation of pH variations of the nucleus, although the nucleus is the target of most anticancer drugs.[29, 30] In the light of the foregoing, alternative strategy is required in order to monitor the cytosolic and nuclear pH for better understanding of the behavior of cells.

In the past, our group introduced the use of silver nanowires (AgNWs) as a non-invasive endoscopic probe to collect highly resolved Raman signals from the nucleus of living cells.[31] Most recently, we have enhanced the SERS performance of AgNWs by etching their surface with Au precursor via galvanic replacement reaction (GRR). After inserting the etched AgNW into a living cell, SERS signals were recorded at the laser focused position on the etched AgNW, namely the direct excitation. Using this method, we proved the site-specificity of our endoscopic technique by detecting SERS signal of dyes from different cell compartments.[32] Moreover, this technique has been proven to be non-invasive according to the cell stress tests by monitoring the variation of the concentration of cytosolic calcium ions.[31, 32] Thanks to its spatio-temporal resolution and non-invasiveness, this technique holds great potential for site-specific pH sensing in living cells. AgNWs can be functionalized with a pH-responsive Raman reporter, such as 4-mercaptobenzoic acid (4-MBA), and inserted into specific compartments of living cells to detect pH variations. The protonation and deprotonation degree of 4-MBA gives rise to a clear change in the SERS intensity of the peak around 1400 cm^{-1}, corresponding to carboxylate stretching mode (COO^-), and can be therefore used for monitoring pH variations.[33, 34] When adsorbed on nanomaterials, the pH response of 4-MBA, as for most interfacial ligands, is affected by the surface curvature (the reciprocal of the radius).[35-37] In a different work, we reported that 4-MBA showed higher sensitivity from pH 5 to 8 when adsorbed on metal nanostructures with larger curvatures.[38] According to these results, the surface of AgNWs needs to be carefully evaluated prior to pH sensing applications.

In this study, we propose an innovative approach for site-specific sensing of cytosolic and nuclear pH using a gold photo-deposited AgNW endoscopic probe (Au-dep AgNW). As recently demonstrated by our group, gold nanostructures can be easily formed at a desired position on the AgNW surface via photoinduced deposition.[39] Comparing with the AgNW probe obtained by GRR (Au-etched AgNW), the Au-dep AgNW showed a highly rough surface with sharp protrusions (larger curvature) and consequently a dramatically enhanced pH sensitivity at a biologically relevant pH range (~ 5 – 8). Taking advantage of the high sensitivity, pH variations in the cytosol and nucleus of HeLa cells before and after treatment with $CoCl_2$ and cisplatin, individually, were successfully monitored by collecting the SERS signals of the 4-MBA immobilized on the gold nanoparticles at the laser focused position. The results obtained in this work showed the great potential of this technique for unraveling crucial information on the relation between intracellular pH and the physiology of cells.

3.3 Result and discussion

Characterization and pH sensitivity of gold-deposited AgNWs. For immobilized acidic ligands, such as 4-MBA, the apparent pK_a drastically increases (up to 4 units)[37] when immobilized on a quasi-flat surface (e.g., large NPs with small curvature) compared to the free molecules in solution (pK_a of 4-MBA in solution = 4.8[40]). This phenomenon raises from electrostatic repulsions of the deprotonated molecules, which make the deprotonated state less favorable (increase of the apparent pK_a).[37,41] In AgNWs, sharp protrusions of Au nanostructures with a local small diameter on the smooth nanowire surface would increase the curvature. From previous results,[32,39] we expect gold-deposited AgNWs via photo-deposition to exhibit a larger curvature than gold-etched AgNWs prepared by GRR. In order to validate this hypothesis and verify the impact on the pH sensitivity of the final probes, we compared the two surface modification methods: GRR and photo-deposition. A schematic representation of the two techniques is shown in Figure 3.1a and 3.1b. The GRR implies that, due to the higher standard reduction potential of Au compared to that of Ag, once a solution containing $HAuCl_4$ is added, gold ions deprive the AgNW surface of electrons, resulting in both etching of Ag (Ag oxidation, $Ag \longrightarrow Ag^+$) and formation of Au nanostructures on the AgNW surface (Au reduction, $Au^{3+} \longrightarrow Au$) (Figure 3.1a).[42,43]

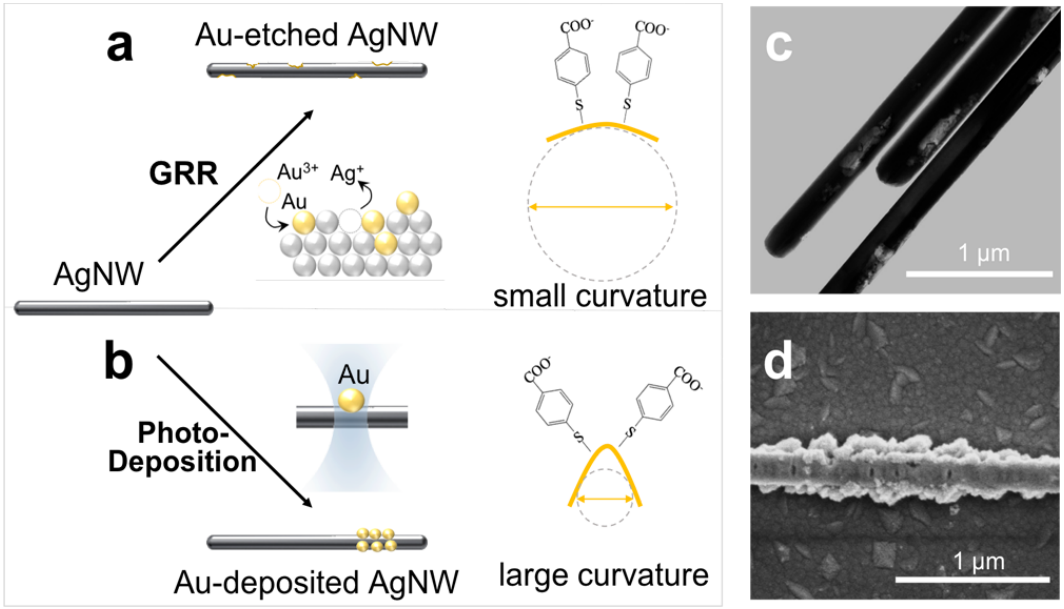

Figure 3.1. Schematic illustration of the fabrication of Au-etched AgNW via GRR (a) and Au-dep AgNW via photo-deposition (b). STEM and SEM image of Au-etched AgNW (c) and Au-dep AgNW (d), respectively.

On the other hand, during the photo-deposition, while GRR is repressed by high pH,[44] the surface plasmon polaritons excited by laser irradiation generate electron-hole pairs on the AgNWs surface, which promote the reduction of Au^{3+} from the $HAuCl_4$ surrounding solution into Au^0. The Au^0 originated from the photo-reduction then deposits on AgNW surface, forming Au nanostructures on the irradiated region (Figure 3.1b).[39] Both methods were performed on AgNWs prepared by the polyol synthesis.[31, 45] GRR was carried out by adding a solution of $HAuCl_4$ (0.2 mM) into an AgNWs solution at 80 °C (Au-etched AgNW). Au-deposition was performed according to the reported method with slight modifications.[39] Shortly, Au NPs were site-specifically deposited by irradiating AgNWs with a 488 nm laser (~ 6 kW/cm^2) for ~ 120 s in a $HAuCl_4$ solution (28.6 μM) at pH 11 (Au-dep AgNW). The pH value was chosen in order to suppress the GRR and, in turn, guarantee a better control of the gold photo-deposition.[46, 47] Scanning transmission electron microscopy (STEM) / scanning electron microscopy (SEM) images of Au-etched and Au-dep AgNW show a clear difference in surface roughness, with no clear Au protursions but rather some hollow structure generated by etching (the concave) on the Au-etched AgNW (Figure 3.1c) and well-defined Au-nanostructures (the convex) obtained by photo-deposition on the Au-dep AgNW surface (Figure 3.1d), respectively. In the concave structure, the surface is inversely bent (compared to the small and large curvature reported in Figure 3.1a and 3.1b) and the resulting molecular repulsions between deprotonated 4-MBA on Au-etched AgNW will be therefore maximized. In order to verify the pH sensitivity of the two probes, and the influence of their surface morphology, Au-etched AgNW and Au-dep AgNW were functionalized with 4-MBA. To this end, a solution of 4-MBA (0.2 mM) was drop casted on spincoated AgNWs and rinsed after 60 min. After the functionalization, SERS spectra were collected from Au-etched AgNW and Au-dep AgNW in PBS solutions at different pH values (4.4, 5.4, 6.5, 7.4, 8.1, and 9.3) (Figure 3.2a and 3.2b, respectively).

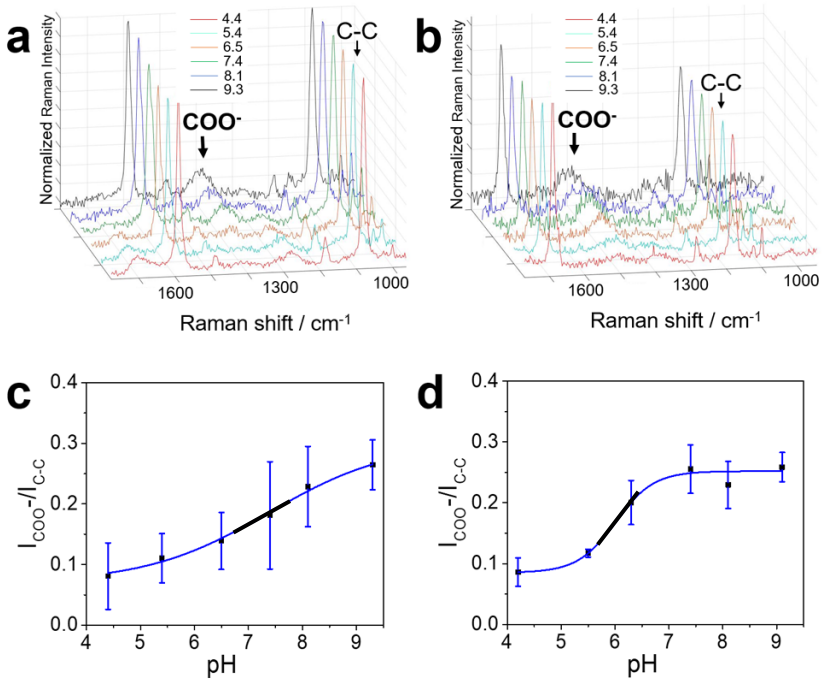

Figure 3.2. pH sensitivity evaluation. SERS spectra of 4-MBA from Au-etched AgNW (a) and from Au-dep AgNW (b) in PBS at various pH values (the spectra were normalized to the peak at 1079 cm^{-1}). Related intensity ratio between COO^- and C–C peak (I_{COO^-} / I_{C-C}) as a function of pH (c and d, respectively), with the black line representing the calibration curve obtained by Boltzmann fitting. (Error bars indicate mean ± SD, with n = 5.)

The intensity ratio of the pH-sensitive band (carboxylate stretching at around 1400 cm^{-1}) to the pH-insensitive band (benzene ring breathing at 1079 cm^{-1}) was plotted as a function of pH and fitted with Boltzmann fitting to construct the pH calibration curve (I_{COO^-} / I_{C-C} curve) (Figure 3.2c, 3.2d, respectively).[38] In order to compare these calibration curves in terms of sensitivity, the most sensitive range (5.5 – 7.5) was assumed as a linear function and the slope was used as an indicator of pH sensitivity. The slope for the calibration curve was estimated to be 0.05 for Au-etched AgNW and 0.1 for Au-dep AgNW, indicating a greater sensitivity for Au-dep AgNW. To further confirm the relation between the curvature and the pH probe sensitivity, we prepared Au-dep AgNW with a smaller curvature using a shorter photo-irradiation time (60 s). SEM images of the Au-dep AgNW obtained upon 60 s irradiation (Figure 3.A1a, 3.A1b) show less sharp protrusions than those obtained under 120 s irradiation (Figure 3.1d). SERS spectra collected from 4-MBA modified Au-dep AgNW obtained with 60 s irradiation in PBS solutions at different pHs (Figure 3.A1c) gave a calibration curve with a slope of 0.07 at the sensitive range (Figure 3.A1d), indicating an intermediate sensitivity (higher than Au-etched AgNW and

lower than Au-dep AgNW obtained by 120 s irradiation). These results confirm the dependence of 4-MBA pH sensitivity on the surface curvature and indicate that Au-dep AgNW fabricated upon 120 s of irradiation holds the highest pH sensitivity, therefore being the most suitable for the fabrication of the endoscopic probes.

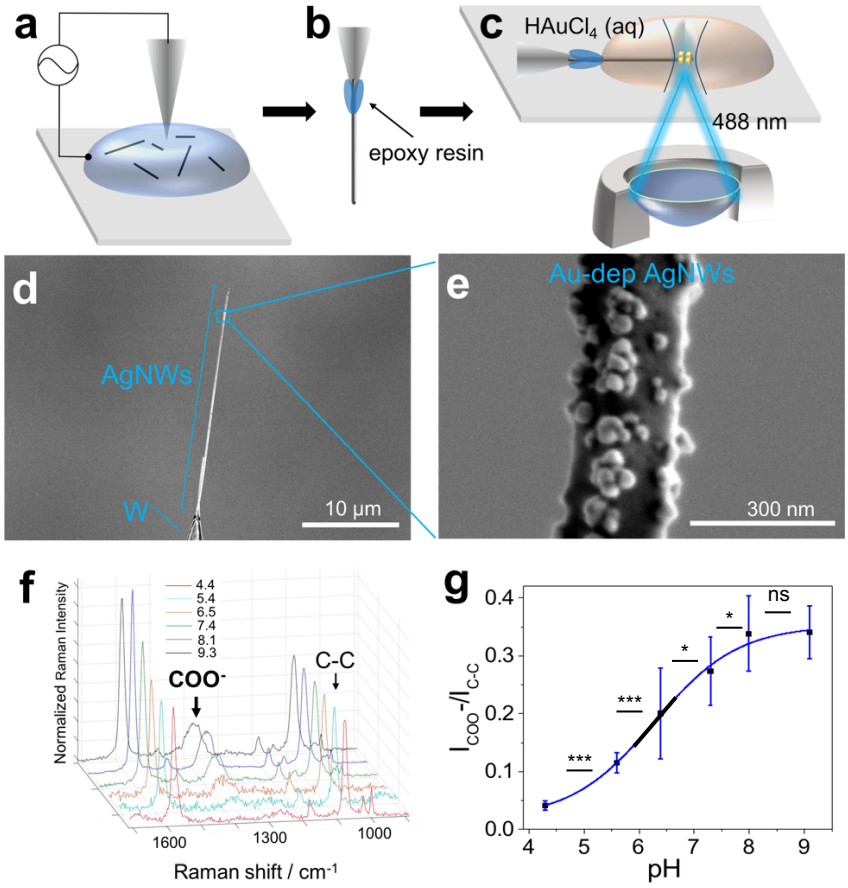

Figure 3.3. Schematic illustration of the fabrication of the Au-dep AgNW endoscopic probe: AgNW attachment to the tungsten tip via AC dielectrophoresis (a), gluing of the tip with epoxy resin (b), and Au deposition by laser irradiation (c). SEM images of the Au-dep AgNW probe at different magnifications (d, e). SERS spectra of 4-MBA on Au-dep AgNW probe in PBS at different pH values (f) (the spectra were normalized to the peak at 1079 cm^{-1}). Related intensity ratio between COO^- and C–C peak (I_{COO^-} / I_{C-C}) as a function of pH (g), with the black line representing the calibration curve obtained by Boltzmann fitting. (Error bars indicate mean ±SD. *** stands for $p < 0.001$; ** stands for $p < 0.01$; * stands for $p < 0.05$; ns stands for $p > 0.05$)

Fabrication and Characterization of Au-dep AgNW endoscopic probes. To investigate the intracellular pH of living cells via endoscopy, Au-dep AgNW endoscopic probes were prepared

as previously reported (Figure 3.3a-c).[31, 48] Briefly, AgNWs were firstly attached to sharpened tungsten (W) tip via alternating current (AC) dielectrophoresis (Figure 3.3a). Afterwards, AgNWs were fixed on the W tip by gluing the junctions with epoxy resin to avoid detachment during the probe insertion into the cell (Figure 3.3b). Finally, the as-obtained AgNW endoscopic probe was immersed into a $HAuCl_4$ aqueous solution and irradiated with a focused 488 nm laser for 120 s to form Au nanostructures (Figure 3.3c).

For the gold deposition on AgNWs attached to the W tip, a slight change in the experimental conditions was required compared to the photo deposition on ITO. Indeed, at pH 11, no clear gold deposition was observed under laser irradiation, most likely due to the higher conductivity of the tungsten compared to ITO. The pH of the $HAuCl_4$ solution was, therefore, decreased to 9.3 in order to slightly increase the reduction potential of $HAuCl_4$. SEM (Figure 3.3d, 3.3e) and EDX measurements (Figure 3.A2) confirm a successful Au photo-deposition. To verify that Au-dep AgNW endoscopic probe (Au-dep AgNW) maintained a high pH sensitivity, SERS spectra were collected from 4-MBA modified probes in PBS solution at different pHs (Figure 3.3f). The corresponding calibration curve gave a slope of 0.1 and a middle point at pH 6.3 (Figure 3.3g), suggesting a high pH sensitivity and a suitable pH-sensitive range (~ pH 5 – 8) for intracellular pH sensing. The as-obtained Au-dep AgNW probes were then applied for endoscopic SERS measurements of pH in live HeLa cells.

Cytosolic and nuclear pH sensing. To evaluate the performance of the endoscopic probes for intracellular pH sensing, the 4-MBA functionalized Au-dep AgNW was specifically inserted either into the cytosol or into the nucleus of a living HeLa cell (schematic illustrations and transmission images in Figure 3.4a-d). More specifically, the 4-MBA functionalized Au-dep AgNW probe gradually approached the cells at an angle of about 30° using a motorized four-axis micromanipulator. Due to the high rigidity and small diameter, the Au-dep AgNW probe could be easily inserted into the area of the nucleus or cytosol of a living HeLa cell. The laser was then focused on the Au deposited position using an objective lens, and Raman spectrum was recorded from the same focal point to estimate the cytosolic or nuclear pH (Figure 3.A3), respectively. The estimated pH values were stable over time (Figure 3.4e), with a mean value of ~ 7.3 both for the cytosol (black line) and for the nucleus (red line). The pH values obtained are in agreement with those reported in the literature for untreated cancer cells,[29, 49] proving that our technique is suitable for intracellular pH sensing. As a comparison, the same endoscopic experiment was performed by using Au-etched AgNW as a probe. The pH values obtained

were fluctuating over time either in the nucleus or in the cytosol (Figure 3.A4), confirming the lower pH accuracy of the smooth probe (Figure 3.1c).

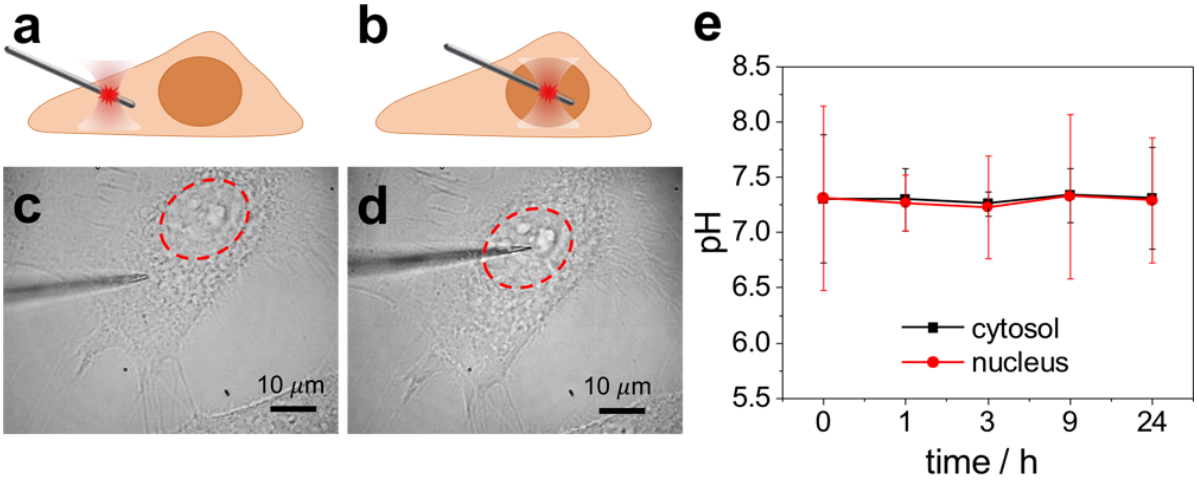

Figure 3.4. Endoscopic pH sensing in a single living cell. Schematic illustration (a, b) and optical transmission images (c, d) of the probe insertion into the cytosol and into the nucleus of a HeLa cell, respectively, with the dashed red circle representing the nucleus. Estimated pH values in the cytosol (black) and in the nucleus (red) of untreated HeLa cells over time obtained by 4-MBA modified Au-dep AgNW (e). (Error bars indicate mean ± SD. 3 cells were used.)

pH changes upon $CoCl_2$ treatment. Cobalt chloride ($CoCl_2$) is a hypoxia-mimetic agent known to affect intracellular pH homeostasis. $CoCl_2$ exposure increases the expression of hypoxia inducible factor-1α (HIF-1α), which regulates Na^+/H^+ exchanger isoform 1 (NHE1) activity (one of the main membrane pH regulators).[50-53] To verify if our probes could detect $CoCl_2$-mediated pH changes, the endoscopic pH sensing was performed on HeLa cells treated with 100 μM of $CoCl_2$ at various incubation time. The plot of the pH values obtained from the 4-MBA modified Au-dep AgNW in the nucleus and in the cytosol of a $CoCl_2$-treated HeLa cell shows a defined curve with a clear time-dependent trend (Figure 3.5a) (corresponding SERS spectra of 4-MBA in Figure 3.A5). A slight decrease of the cytosolic pH from 7.3 to 6.9 was already observed during the first hour of incubation (Figure 3.5a, black line). Afterwards, an increase of 0.6 pH units was detected from 3 to 24 h of incubation with $CoCl_2$. According to previous studies, the early pH decrease corresponds to the downregulation of NHE1, caused by $CoCl_2$ exposure, which is then followed by a subsequent re-activation, most likely triggered by the intracellular acidosis.[53, 54] Although the initial and final pH values were similar between

the cytosol and the nucleus (at 0 and 24 h, respectively), in the time-lapse between 1 and 9 h of incubation with $CoCl_2$, the nuclear pH detected was 0.3 to 0.8 pH units lower than the one in the cytosol (Figure 3.5a, red line). This difference might indicate that $CoCl_2$ has an additional independent effect on nuclear pH regulation, but further studies are needed to confirm and understand this phenomenon. The overall trend of the cytosolic pH measured with Au-dep AgNW endoscopic probe is consistent with the literature,[53] indicating that our technique enables the detection of intracellular pH changes caused by $CoCl_2$ exposure.

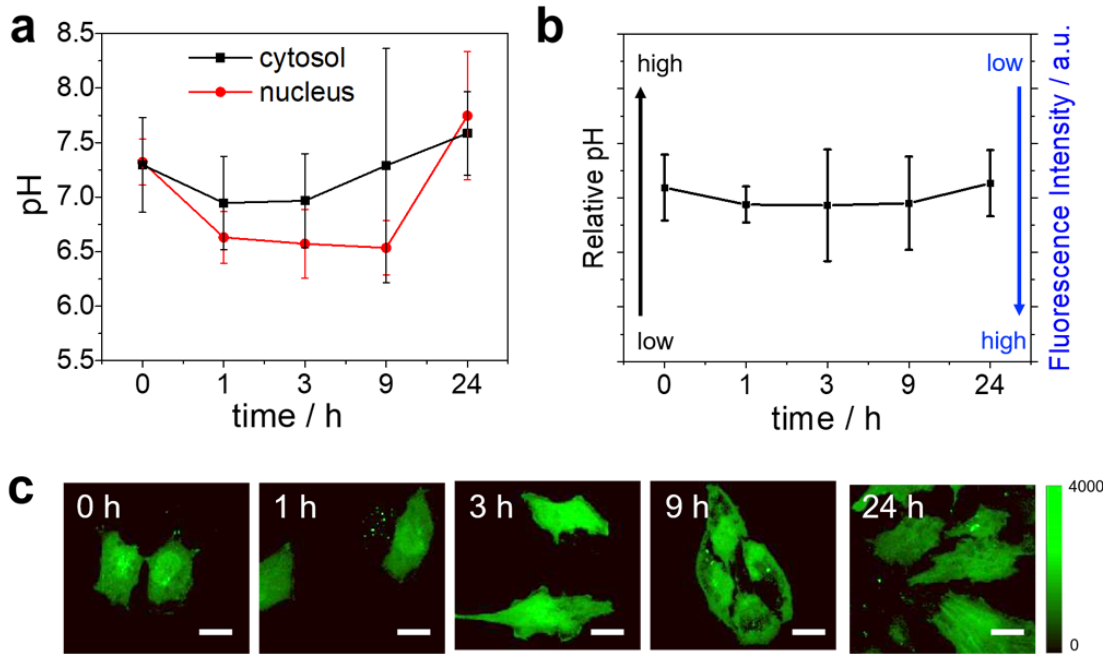

Figure 3.5. Intracellular pH variations in $CoCl_2$-treated HeLa cells obtained by 4-MBA modified Au-dep AgNW probes over time (a). Fluorescence intensity variations of pHrodo green AM in HeLa cells upon $CoCl_2$ treatment over time (b) and representative confocal fluorescence images obtained at 0, 1, 3, 9, and 24 h of incubation with $CoCl_2$ (c) (scale bar: 20 μm). (Error bars indicate mean ± SD. 3 cells were used.)

For comparing the results obtained via endoscopy with those given by fluorescence-based measurements, $CoCl_2$-treated HeLa cells were stained with pHrodo Green AM, a commercially available pH-sensitive dye, and the cytosolic pH variations were estimated from fluorescence intensity changes of the dye (Figure 3.5b). The related fluorescence images at 0, 1, 3, 9, and 24 h of incubation with $CoCl_2$ are depicted in Figure 3.5c. An initial increase within the first hour of incubation and the following decrease of pHrodo Green AM fluorescent intensity were observed, which correspond to an initial pH decrease and an increase afterwards. The pH trend

found via fluorescence measurements was comparable with the one obtained by endoscopy, confirming the reliability of the endoscopic approach. Note that compared to fluorescence-based techniques, our SERS-based endoscopic technique holds the major advantages of providing absolute pH values and having an exclusive spatio-temporal resolution, which enables to site-specifically detect pH values at a certain time point in living cells. A comparison with Au-etched AgNW was carried out for this experiment as well (Figure 3.A6). Once again, the pH monitored by Au-etched AgNW showed pH values largely fluctuating over time for both cytosolic and nuclear pH.

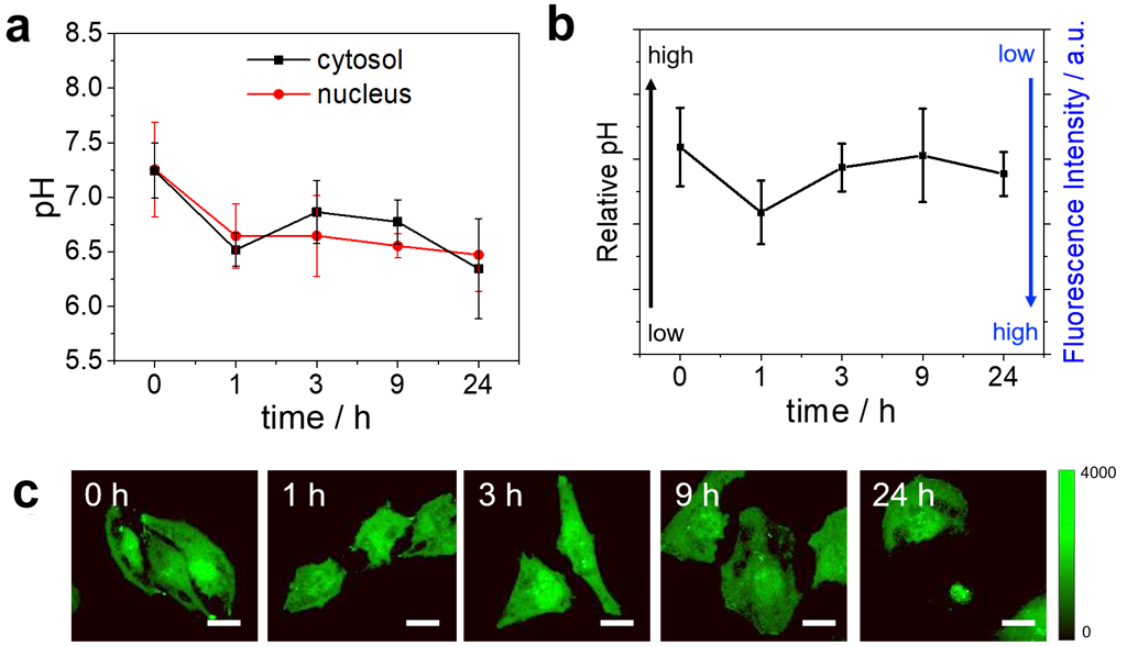

Figure 3.6. Intracellular pH variations in cisplatin-treated HeLa cells obtained by 4-MBA modified Au-dep AgNW probes over time (a). Fluorescence intensity variations of pHrodo green AM in HeLa cells upon cisplatin treatment over time (b) and representative confocal fluorescence images obtained at 0, 1, 3, 9, and 24 h of incubation with cisplatin (c) (scale bar: 20 μm). (Error bars indicate mean ± SD. 3 cells were used.)

pH changes upon cisplatin treatment. Cisplatin is a common chemotherapeutic drug used for treating several types of cancer. Recent studies revealed unexpected cytoplasm acidification during cell apoptosis upon treatment with cisplatin.[55] While the main mechanism of the anticancer action of this drug is associated with DNA damage upon platination, the aforementioned research suggests that other mechanisms might be involved in cell apoptosis. To investigate the cytosolic pH alteration and verify if there is an effect on the nuclear pH upon

cisplatin treatment, HeLa cells were treated with 20 μM of cisplatin and subjected to the endoscopic pH sensing at various incubation time. The cytosolic pH curve (Figure 3.6a, black line) showed a decrease of 0.7 pH units within the first hour of incubation. Subsequently, after a transient pH increase of 0.4 pH unit, the pH continues to decrease, reaching the value of 6.3 at 24 h of incubation (corresponding SERS spectra of 4-MBA in Figure 3.A7).

As performed for $CoCl_2$ treatment, in order to compare the endoscopic results with the ones collected by fluorescence measurements, cisplatin-treated HeLa cells were stained with pHrodo Green AM, and the fluorescence intensity variations were monitored over time. The plot of the pHrodo Green AM fluorescence intensity for cisplatin-treated HeLa cells revealed an initial pH decrease with a subsequent increase between 1 and 3 h of incubation, followed by a decrease within 24 h (Figure 3.6b). The related fluorescence images at 0, 1, 3, 9, and 24 h of incubation with cisplatin are depicted in Figure 3.6c. The pH trend corresponding to the fluorescence intensity change is consistent with the one obtained via SERS signals of 4-MBA in the endoscopy experiments (Figure 3.6a). The transient pH increases between 1 and 9 h of incubation was also confirmed by fluorescence-based measurements. The overall cytosolic pH behavior found with our experiments, including the minor increase between 1 and 9 h of incubation, is consistent with the one reported in a previous work (where cisplatin-responsive pH variations were monitored by a genetically encoded pH sensor).[56] Nonetheless, the cause of this pH acidification is still not well understood. It seems to be independent of the DNA damage and be rather related to the inhibition of NHE1.[55] The transient pH increase between 1 and 9 h of incubation might result from the ability of cells to maintain pH homeostasis at short-term cisplatin exposure.[56] Regarding the nuclear pH variations (Figure 3.6a, red line), no relevant difference was observed compared to the cytosolic pH, with nuclear pH following a more linear acidification trend. For unraveling the specific mechanism involved in the pH alterations detected, further investigation is needed. However, the data reported evidently prove the ability and the accuracy of the Au-dep AgNW for sensing intracellular pH upon drug treatments.

In order to demonstrate the potential of our endoscopy technique over the conventional nanoparticle-based SERS pH sensing, gold-coated silver nanoflowers were synthesized (SEM image in Figure 3.A8) and modified with 4-MBA as previously reported.[38] $CoCl_2$-treated and cisplatin-treated HeLa cells were then incubated with 4-MBA modified gold-coated silver nanoflowers for 1 h to enable the particle uptake, and SERS spectra of 4-MBA were recorded

at different time points (Figure 3.A9). The pH plots obtained from these measurements show a constant pH decrease in time, suggesting that the particles are located in the endo-lysosomal system (where particles are entrapped after endocytosis). No relevant difference was found for the two treatments: none of the pH variations registered via endoscopy was detected, incontestably proving the potential of our technique over NP-based pH sensing.

3.4 Conclusion

In summary, an innovative SERS-based endoscopic technique was proposed for intracellular pH sensing. The endoscopic probe was fabricated via light-induced Au deposition on silver nanowires (Au-dep AgNW), which were then modified with 4-mercaptobenzioc acid. The pH accuracy was proved to be higher than our previously reported Au-etched AgNW obtained via GRR. By inserting Au-dep AgNW in HeLa cells, the intracellular pH was successfully monitored over time. Subsequently, the technique was applied for the detection of pH alterations upon $CoCl_2$ and cisplatin treatments. The results obtained were consistent with previous studies and were additionally confirmed by fluorescence-based pH measurements, proving the accuracy and reliability of our technique. The same experiments for intracellular pH sensing were carried out by using metal nanoparticles. No relevant data on pH variations upon $CoCl_2$ and cisplatin exposure were obtained via NP-based sensing, proving the potential of our endoscopic probe over the standard SERS-based pH sensing. The results reported thereby provide evidence that our endoscopic approach is a powerful strategy for a wide range of pH-sensing investigations toward a better understanding of biochemical events in single living cells.

3.5 Experiment

Reagents. Silver nitrate ($AgNO_3$), tetrachloroauric(III) acid ($HAuCl_4$), cisplatin, and ethylene glycol (anhydrous, 99.8%) were purchased from SIGMA–ALDRICH (Japan). 4-mercaptobenzoic acid (4-MBA) was purchased from Tokyo Chemical Industry Co., Ltd. (TCI). pHrodo Green AM was purchased from Invitrogen (Japan). Ethanol, trisodium citrate dehydrate (Na_3Cit), polyvinylpyrrolidone K30 (PVP), copper chloride ($CuCl_2$), L(+)-ascorbic acid, cobalt(II) chloride hexahydrate ($CoCl_2$), and sodium hydroxide (NaOH) were purchased from FUJIFILM Wako Pure Chemical Corporation. All the reagents were used as received without further purification.

Synthesis of silver nanowires (AgNWs). The AgNWs were synthesized according to the reported method with some modifications.[31, 45] Briefly, 0.3 mM of PVP was dissolved in 9.66 mL of ethylene glycol and heated at 160 °C for 1 h. 80 μL of $CuCl_2$ solution in ethylene glycol (4 mM) was added to this solution. After stirring for 10 min, 100 μL of $AgNO_3$ solution in ethylene glycol (0.12 M) was then added. After the color of the solution turned greenish, 4.9 mL of $AgNO_3$ solution in ethylene glycol (0.12 M) was added drop-wise with a rate of 100 μL / min. After adding the $AgNO_3$ solution, the mixture was further heated at 160 °C for 2 hours. Then the mixture was cooled down to room temperature.

Fabrication of gold deposited AgNWs on indium tin oxide (ITO) substrates. The AgNWs solution was spin-coated on ITO substrates. Then it was heated at 80 °C for 30 min. Afterward, a polydimethylsiloxane (PDMS) frame was sealed to the sample to contain the aqueous solution of $HAuCl_4$. A 488 nm laser polarized perpendicular to the longitudinal axis of AgNW was focused on the AgNW by using an objective lens.

Fabrication of Au-etched AgNW and Au-dep AgNW probes. The Au etching was performed according to the reported method with modification.[48] 15 mL of MilliQ water was heated at 80 °C for 10 minutes. 450 μL of the AgNWs solution was then added, followed by adding 1.8 mL of 0.2 mM of $HAuCl_4$ solution. Then the mixture was heated for 15 minutes. Au-etched AgNW were collected by centrifugations at 1200 rpm (x3). The tungsten tips were prepared by applying a voltage between tungsten wires and a ring-shaped wire electrode in a NaOH solution. To attach the nanowires to the tungsten tip, a voltage with a frequency of 1 MHz was applied between the etched tungsten tip and the ring-shaped wire electrode in an

ethanol solution of AgNWs or Au-etched AgNW. The junction between the nanowires and the tungsten tip was then glued with conductive epoxy under the optical microscope using an additional etched tungsten tip. For preparing Au-dep AgNW, the AgNW on W was inserted into the aqueous solution of $HAuCl_4$ at pH 9.3. Subsequently, a 488 nm laser light, polarized perpendicular to the longitudinal axis of AgNW, was focused on the AgNW to form Au NPs.

Synthesis of gold-coated silver nanoflowers. The silver nanoflowers were synthesized according to the reported method with modification for better dispersity in suspension.[57-59] Briefly, 0.2 mL of 0.1 M $AgNO_3$ in ethylene glycol and 2.0 mL of 1.36 mM Na_3Cit solution were added to 10 mL of MilliQ water (18 MΩ cm, Milli–Q System, Millipore) and stirred for 5 minutes at room temperature. Then, 0.8 mL of 0.1 M NaOH and 1.0 mL of 0.1 M L(+)-ascorbic acid were added and stirred to the mixture, which was again stirred for 15 minutes. The silver nanoflowers were collected by centrifugation**.** The Au coating was performed according to the reported method with modification.[59, 60] 0.1 mL of a mixed solution prepared from 0.5 mL of 0.5 M NaOH and 1.0 mL of 0.1 M L(+)-ascorbic acid was added to 0.8 mL of silver nanoflowers dispersed in water. Then 0.1 mL of 1 mM $HAuCl_4$ solution was added, and the mixture was stirred for 1 h. The excess of gold ions was removed by centrifugation at 5000 rpm (x3).

SERS pH calibration curve. Au deposited AgNW or Au etched AgNW were modified with 4-MBA (0.2 mM, in ethanol) prior to the calibration measurements. Afterwards, the 4-MBA modified probes were immersed in PBS solutions at different pHs (4.4, 5.4, 6.5, 7.4, 8.1, and 9.3) and the SERS spectra were collected (1 s exposure time, 633 nm excitation). 5 spectra for each pH value were used to construct the calibration curves. To get the exact peak intensities, for each spectrum, the peaks at around 1400 cm^{-1} and 1079 cm^{-1} were fitted using Gaussian Fitting. Finally, the intensity ratio between these peaks (I_{COO^-} / I_{C-C}) was then calculated for each spectrum at every pH value. The plots of I_{COO^-} / I_{C-C} as a function of pH were fitted using Boltzmann Fitting in order to obtain a calibration curve. For intracellular pH sensing, 5 spectra were used to calculate the mean value of each time point.

Characterization. The morphology of nanowires was characterized by scanning transmission electron microscopy (STEM, HITACHI HD–2000), and scanning electron microscopy (SEM, JEOL JSM-6700FT) equipped with energy dispersive X-ray spectroscopy (EDX). Raman spectroscopy was conducted using an inverted optical microscope (TiU, Nikon) equipped with

a piezoelectric positioning stage operated with Omega software (Combiscope, AIST–NT/HORIBA). Continuous wave 633 nm laser light (LGK–7665 P18, LASOS) was reflected by a dichroic mirror (Z633RDC, Chroma) and was then focused onto the sample by an objective lens (PlanFluo x60, N.A. 0.85, Nikon). Raman scattering light from the sample was collected by the same objective and was guided to the spectrograph (iHR320, Horiba) equipped with a CCD detector (Newton DU920P–BEX2–DD, Andor) after passing through a confocal pinhole and longpass filters (HQ645LP, Chroma). A motorized four-axis micromanipulator with stepper motor and piezoelectric translation, PCS–6000CR (Thorlabs), which provides smooth and precise movement of the endoscopy probe, is used to glue the AgNW-W probes and manipulate the endoscopy probe to perform the intracellular measurements.

Cell culture. HeLa cells were cultured in 60 mm cell culture dishes at 37 ˚C under humidified 5% CO_2 atmosphere. Once the confluency reached around 80%, the cells were passaged via trypsinization. The cells were maintained in Dulbecco's modified Eagle medium (DMEM) containing 10% of FBS, 1% of L-glutammax, and 0.1% of gentamicin. For the SERS measurements, the medium was replaced with fresh medium (1 mL) and $CoCl_2$ or cisplatin was added into the culture. Then the same culture was further incubated at 37 °C under humidified 5% CO_2 for different time intervals.

Living Cells SERS Endoscopy measurements. The cell culture dish was put on an inverted microscope equipped with a piezoelectric stage. The endoscopy probe was gradually managed to approach the cells with an angle of about 30° using a motorized four-axis micromanipulator with stepper motor and piezoelectric translation, which allows manipulating the endoscopy probe with very high precision, following by slowly inserting into the area of nucleus or cytosol of a living HeLa cell. The laser was then focused on the probe by an objective lens, and Raman signals were collected from the same focal point. After the measurement, the cells were kept at 37 ˚C under humidified 5% CO_2 atmosphere for the measurement at other time points. For the analysis, after subtracting the background of the obtained SERS spectra, the peaks at around 1400 cm^{-1} and 1079 cm^{-1} were fitted using Gaussian Fitting. Then, the intensity ratio between these peaks (I_{COO^-} / I_{C-C}) was calculated at the current time point. Finally, the pH was calculated using the previous calibration curve shown in Figure 3.3g.

Fluorescence-based pH sensing. After the addition of $CoCl_2$ or cisplatin, the cells at different time points were stained with pHrodo Green AM (0.01 mM) which is a pH-sensitive dye for

30 min and washed with Hanks' Balanced Salt Solution (HBSS). Confocal fluorescence images were then collected for these samples at 0, 1, 3, 9 and 24 h with Nikon inverted microscope Ti-E using 60x objective and 488 nm laser excitation. The mean intensity in the cytosolic area of 5 cells for each time point was calculated and plotted as mean value ± SD as a function of time. The exact corresponding pH was not calculated.

3.6 Appendix

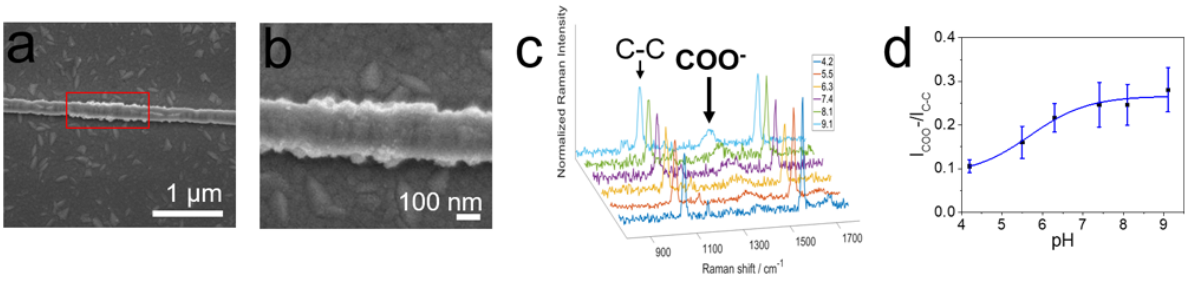

Figure 3.A1. SEM images of Au-dep AgNW under 60 s irradiation (a, b), related SERS spectra of 4-MBA in PBS solutions at varied pH values (c) and pH calibration curve (d).

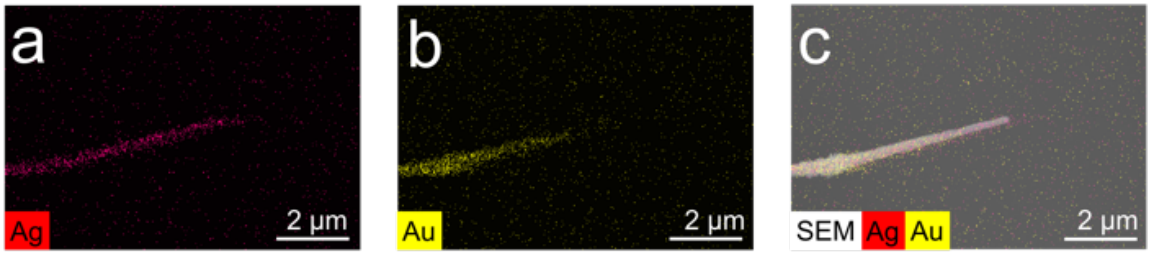

Figure 3.A2. EDX mappings of Au-dep AgNW: Ag (a), Au (b), and overlay of Ag, Au and SEM image (c).

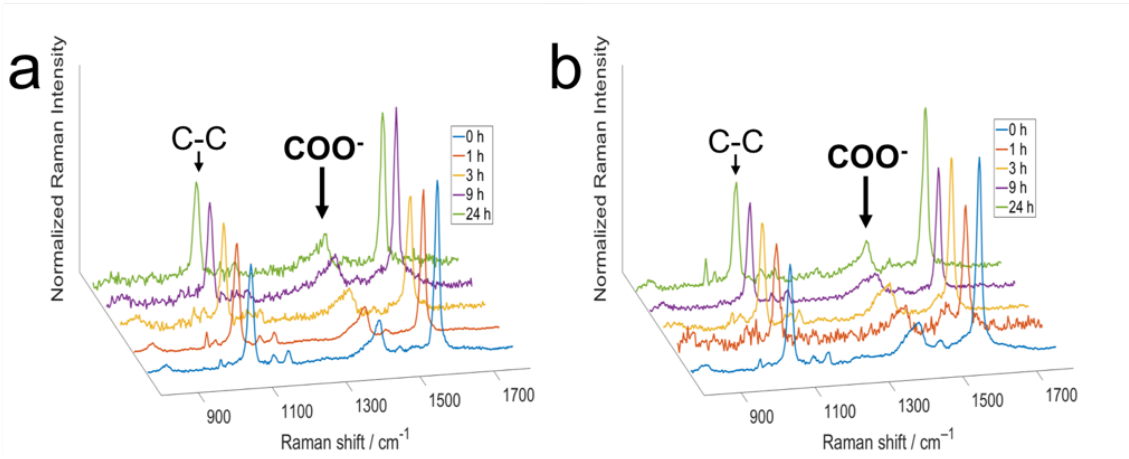

Figure 3.A3. SERS spectra of 4-MBA obtained from Au-dep AgNW inserted in the cytosol (a) and in the nucleus (b) of untreated HeLa cells at different time points (the spectra were normalized to the peak at 1079 cm^{-1}).

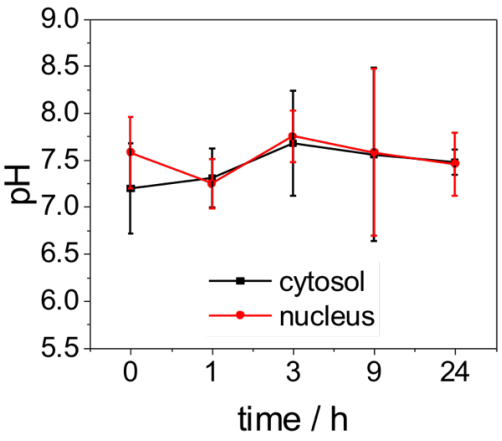

Figure 3.A4. Intracellular pH in untreated HeLa cells measured by 4-MBA modified Au-etched AgNW over time. (Error bars indicate mean ± SD.)

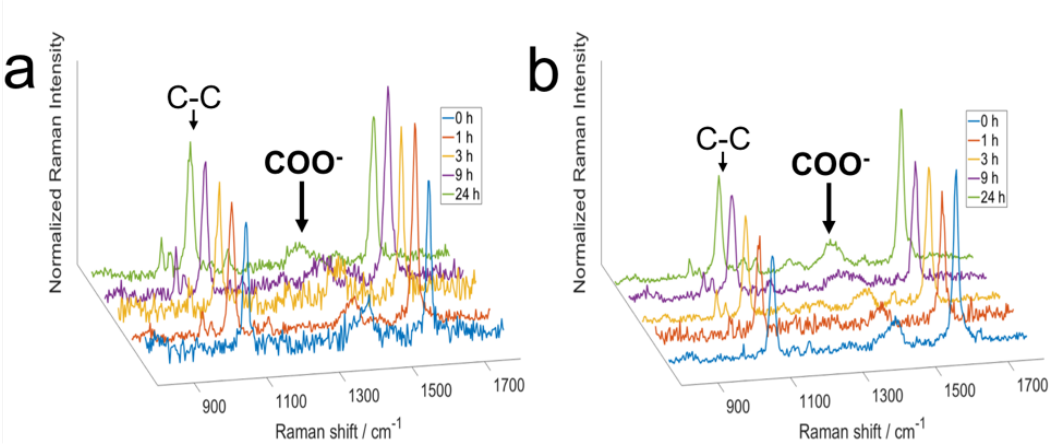

Figure 3.A5. SERS spectra of 4-MBA obtained from Au-dep AgNW inserted in the cytosol (a) and in the nucleus (b) of $CoCl_2$-treated HeLa cells at different incubation time (the spectra were normalized to the peak at 1079 cm^{-1}).

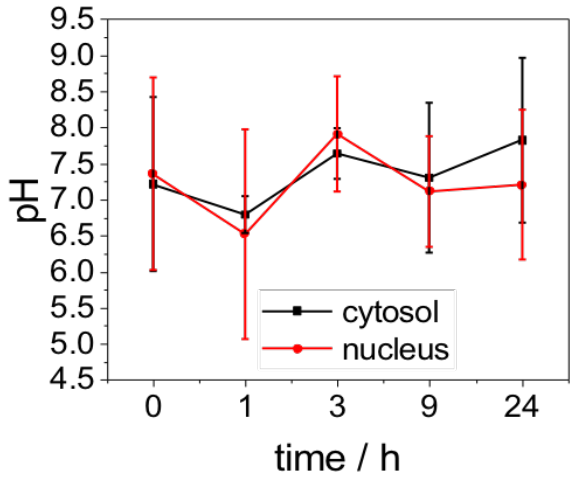

Figure 3.A6. Intracellular pH variations in $CoCl_2$-treated cells measured by 4-MBA modified Au-etched AgNW over time. (Error bars indicate mean ± SD.)

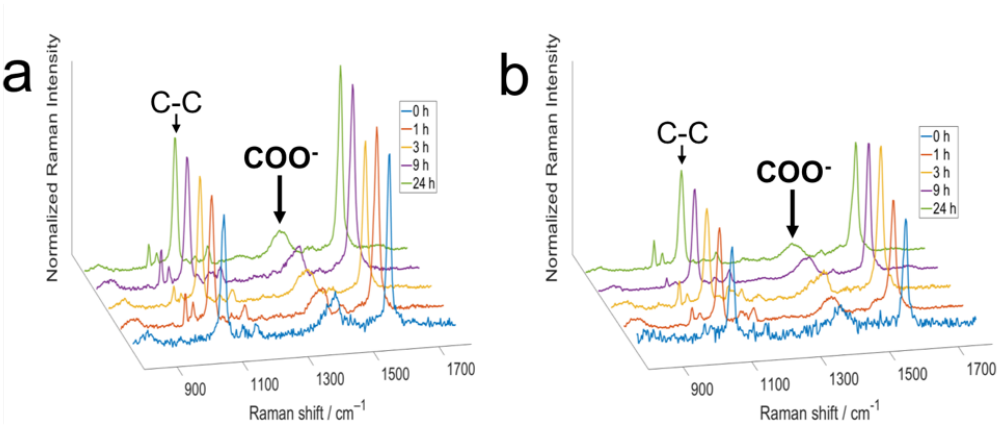

Figure 3.A7. SERS spectra of 4-MBA obtained from Au-dep AgNW inserted in the cytosol (a) and in the nucleus (b) of cisplatin-treated HeLa cells at different incubation time (the spectra were normalized to the peak at 1079 cm^{-1}).

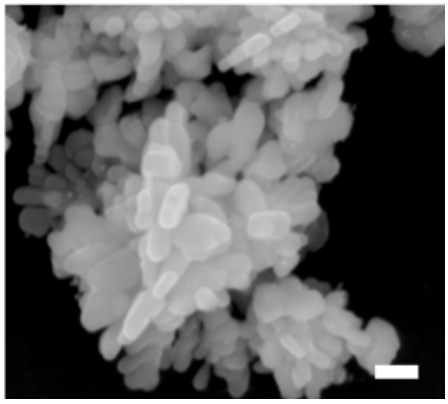

Figure 3.A8. SEM image of gold-coated silver nanoflowers. Scale bar: 100 nm.

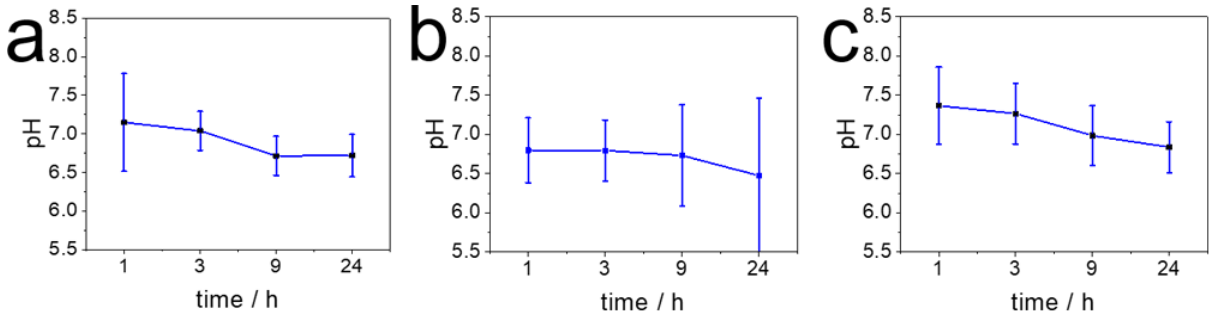

Figure 3.A9. Intracellular pH evaluations in untreated (a), $CoCl_2$-treated (b), and cisplatin-treated (c) HeLa cells measured by 4-MBA modified gold-coated silver nanoflowers over time. (Error bars indicate mean ± SD.)

3.7 References

1. Koch, L. M.; Birkeland, E. S.; Battaglioni, S.; Helle, X.; Meerang, M.; Hiltbrunner, S.; Ibáñez, A. J.; Peter, M.; Curioni-Fontecedro, A.; Opitz, I.; Dechant, R., Cytosolic pH regulates proliferation and tumour growth by promoting expression of cyclin D1. *Nat. Metab.* **2020,** *2* (11), 1212-1222.

2. Webb, B. A.; Chimenti, M.; Jacobson, M. P.; Barber, D. L., Dysregulated pH: a perfect storm for cancer progression. *Nat. Rev. Cancer* **2011,** *11* (9), 671-7.

3. Asgharzadeh, M. R.; Barar, J.; Pourseif, M. M.; Eskandani, M.; Jafari Niya, M.; Mashayekhi, M. R.; Omidi, Y., Molecular machineries of pH dysregulation in tumor microenvironment: potential targets for cancer therapy. *Bioimpacts* **2017,** *7* (2), 115-133.

4. Damaghi, M.; Wojtkowiak, J. W.; Gillies, R. J., pH sensing and regulation in cancer. *Front Physiol* **2013,** *4* (370), 370.

5. Korenchan, D. E.; Flavell, R. R. J. C., Spatiotemporal pH heterogeneity as a promoter of cancer progression and therapeutic resistance. *CANCERS* **2019,** *11* (7), 1026.

6. Pérez-Sala, D.; Collado-Escobar, D.; Mollinedo, F. J. J. o. B. C., Intracellular alkalinization suppresses lovastatin-induced apoptosis in HL-60 cells through the inactivation of a pH-dependent endonuclease. *J. Biol. Chem.* **1995,** *270* (11), 6235-6242.

7. Al-Hilli, S. M.; Willander, M.; Öst, A.; Strålfors, P., ZnO nanorods as an intracellular sensor for pH measurements. *J. Appl. Phys.* **2007,** *102* (8), 084304.

8. Han, J.; Burgess, K., Fluorescent indicators for intracellular pH. *Chem. Rev.* **2010,** *110* (5), 2709-28.

9. Wencel, D.; Abel, T.; McDonagh, C., Optical chemical pH sensors. *Anal. Chem.* **2014,** *86* (1), 15-29.

10. Zong, C.; Xu, M.; Xu, L. J.; Wei, T.; Ma, X.; Zheng, X. S.; Hu, R.; Ren, B., Surface-Enhanced Raman Spectroscopy for Bioanalysis: Reliability and Challenges. *Chem. Rev.* **2018,** *118* (10), 4946-4980.

11. Cialla-May, D.; Zheng, X. S.; Weber, K.; Popp, J., Recent progress in surface-enhanced Raman spectroscopy for biological and biomedical applications: from cells to clinics. *Chem. Soc. Rev.* **2017,** *46* (13), 3945-3961.

12. Zheng, X. S.; Hu, P.; Cui, Y.; Zong, C.; Feng, J. M.; Wang, X.; Ren, B., BSA-coated nanoparticles for improved SERS-based intracellular pH sensing. *Anal. Chem.* **2014,** *86* (24), 12250-7.

13. Jaworska, A.; Jamieson, L. E.; Malek, K.; Campbell, C. J.; Choo, J.; Chlopicki, S.; Baranska, M., SERS-based monitoring of the intracellular pH in endothelial cells: the influence of the extracellular environment and tumour necrosis factor-alpha. *Analyst* **2015,** *140* (7), 2321-9.

14. Luo, R.; Li, Y.; Zhou, Q.; Zheng, J.; Ma, D.; Tang, P.; Yang, S.; Qing, Z.; Yang, R., SERS monitoring the dynamics of local pH in lysosome of living cells during photothermal therapy. *Analyst* **2016,** *141* (11), 3224-7.

15. Zong, S.; Wang, Z.; Yang, J.; Cui, Y., Intracellular pH sensing using p-aminothiophenol functionalized gold nanorods with low cytotoxicity. *Anal. Chem.* **2011,** *83* (11), 4178-83.

16. Kneipp, J.; Kneipp, H.; Wittig, B.; Kneipp, K., Following the Dynamics of pH in Endosomes of Live Cells with SERS Nanosensors. *J. Phys. Chem. C* **2010,** *114* (16), 7421-7426.

17. Pallaoro, A.; Braun, G. B.; Reich, N. O.; Moskovits, M., Mapping local pH in live cells using encapsulated fluorescent SERS nanotags. *Small* **2010,** *6* (5), 618-22.

18. Behzadi, S.; Serpooshan, V.; Tao, W.; Hamaly, M. A.; Alkawareek, M. Y.; Dreaden, E. C.; Brown, D.; Alkilany, A. M.; Farokhzad, O. C.; Mahmoudi, M., Cellular uptake of nanoparticles: journey inside the cell. *Chem. Soc. Rev.* **2017,** *46* (14), 4218-4244.

19. Salatin, S.; Maleki Dizaj, S.; Yari Khosroushahi, A., Effect of the surface modification, size, and shape on cellular uptake of nanoparticles. *Cell Biol. Int.* **2015,** *39* (8), 881-90.

20. Zhang, Z.; Bando, K.; Mochizuki, K.; Taguchi, A.; Fujita, K.; Kawata, S., Quantitative Evaluation of Surface-Enhanced Raman Scattering Nanoparticles for Intracellular pH Sensing at a Single Particle Level. *Anal. Chem.* **2019,** *91* (5), 3254-3262.

21. Cvetković, D. M.; Živanović, M. N.; Milutinović, M. G.; Djukić, T. R.; Radović, M. D.; Cvetković, A. M.; Filipović, N. D.; Zdravković, N. D., Real-time monitoring of cytotoxic effects of electroporation on breast and colon cancer cell lines. *Bioelectrochemistry* **2017,** *113*, 85-94.

22. Remaut, K.; Oorschot, V.; Braeckmans, K.; Klumperman, J.; De Smedt, S. C., Lysosomal capturing of cytoplasmic injected nanoparticles by autophagy: an additional barrier to non viral gene delivery. *J. Control. Release* **2014,** *195*, 29-36.

23. Yan, R.; Park, J. H.; Choi, Y.; Heo, C. J.; Yang, S. M.; Lee, L. P.; Yang, P., Nanowire-based single-cell endoscopy. *Nat. Nanotechnol.* **2011,** *7* (3), 191-6.

24. Cheemalapati, S. V.; Winskas, J.; Wang, H.; Konnaiyan, K.; Zhdanov, A.; Roth, A.; Adapa, S. R.; Deonarine, A.; Noble, M.; Das, T.; Gatenby, R.; Westerheide, S. D.; Jiang, R. H.; Pyayt, A., Subcellular and in-vivo Nano-Endoscopy. *Sci Rep* **2016,** *6* (1), 34400.

25. Wang, J.; Geng, Y.; Shen, Y.; Shi, W.; Xu, W.; Xu, S., SERS-active fiber tip for intracellular and extracellular pH sensing in living single cells. *Sens. Actuators B Chem.* **2019,** *290*, 527-534.

26. Guo, J.; Sesena Rubfiaro, A.; Lai, Y.; Moscoso, J.; Chen, F.; Liu, Y.; Wang, X.; He, J., Dynamic single-cell intracellular pH sensing using a SERS-active nanopipette. *Analyst* **2020,** *145* (14), 4852-4859.

27. Zhao, X.; Campbell, S.; Wallace, G. Q.; Claing, A.; Bazuin, C. G.; Masson, J. F., Branched Au Nanoparticles on Nanofibers for Surface-Enhanced Raman Scattering Sensing of Intracellular pH and Extracellular pH Gradients. *ACS Sens* **2020,** *5* (7), 2155-2167.

28. Yum, K.; Wang, N.; Yu, M. F., Nanoneedle: a multifunctional tool for biological studies in living cells. *Nanoscale* **2010,** *2* (3), 363-72.

29. Casey, J. R.; Grinstein, S.; Orlowski, J., Sensors and regulators of intracellular pH. *Nat. Rev. Mol. Cell Biol.* **2010,** *11* (1), 50-61.

30. Keminer, O.; Peters, R., Permeability of single nuclear pores. *Biophys. J.* **1999,** *77* (1), 217-28.

31. Lu, G.; De Keersmaecker, H.; Su, L.; Kenens, B.; Rocha, S.; Fron, E.; Chen, C.; Van Dorpe, P.; Mizuno, H.; Hofkens, J.; Hutchison, J. A.; Uji-i, H., Live-Cell SERS Endoscopy Using Plasmonic Nanowire Waveguides. *Adv. Mater.* **2014,** *26* (30), 5124-5128.

32. Ricci, M.; Fortuni, B.; Vitale, R.; Zhang, Q.; Fujita, Y.; Toyouchi, S.; Lu, G.; Rocha, S.; Inose, T.; Uji-i, H., Gold-Etched Silver Nanowire Endoscopy: Toward a Widely Accessible Platform for Surface-Enhanced Raman Scattering-Based Analysis in Living Cells. *Anal. Chem.* **2021,** *93* (12), 5037-5045.

33. Xie, M.; Li, F.; Gu, P.; Wang, F.; Qu, Z.; Li, J.; Wang, L.; Zuo, X.; Zhang, X.; Shen, J. J. C. p., Gold nanoflower-based surface-enhanced Raman probes for pH mapping of tumor cell microenviroment. *Cell Prolif.* **2019,** *52* (4), e12618.

34. Park, J. E.; Yonet-Tanyeri, N.; Vander Ende, E.; Henry, A. I.; Perez White, B. E.; Mrksich, M.; Van Duyne, R. P., Plasmonic Microneedle Arrays for in Situ Sensing with Surface-Enhanced Raman Spectroscopy (SERS). *Nano Lett.* **2019,** *19* (10), 6862-6868.

35. Gonzalez Solveyra, E.; Szleifer, I., What is the role of curvature on the properties of nanomaterials for biomedical applications? *Wiley Interdiscip. Rev. Nanomed. Nanobiotechnol.* **2016,** *8* (3), 334-54.

36. Villarreal, E.; Li, G. G.; Zhang, Q.; Fu, X.; Wang, H., Nanoscale Surface Curvature Effects on Ligand-Nanoparticle Interactions: A Plasmon-Enhanced Spectroscopic Study of Thiolated Ligand Adsorption, Desorption, and Exchange on Gold Nanoparticles. *Nano Lett.* **2017,** *17* (7), 4443-4452.

37. Walker, D. A.; Leitsch, E. K.; Nap, R. J.; Szleifer, I.; Grzybowski, B. A., Geometric curvature controls the chemical patchiness and self-assembly of nanoparticles. *Nat. Nanotechnol.* **2013,** *8* (9), 676-81.

38. Zhang, Q.; Wen, H.; Watanabe, K.; Kotani, I.; Ricci, M.; Fortuni, B.; Dao, A. T. N.; Masuhara, A.; Hirai, K.; Kasai, H.; Inose, T.; Uji-i, H., Low-Cytotoxic Gold-Coated Silver Nanoflowers for Intracellular pH Sensing. *ACS Appl. Nano Mater.* **2020,** *3* (8), 7643-7650.

39. Toyouchi, S.; Wolf, M.; Nakao, Y.; Fujita, Y.; Inose, T.; Fortuni, B.; Hirai, K.; Hofkens, J.; De Feyter, S.; Hutchison, J.; Uji, I. H., Controlled Fabrication of Optical Signal Input/Output Sites on Plasmonic Nanowires. *Nano Lett.* **2020,** *20* (4), 2460-2467.

40. Dzięcielewski, I.; Krajczewski, J.; Dzwolak, W., pH-Responsive mixed-thiol-modified surface of roughened GaN: A wettability and SERS study. *Appl. Surf. Sci.* **2020,** *502*, 144108.

41. Wang, D.; Nap, R. J.; Lagzi, I.; Kowalczyk, B.; Han, S.; Grzybowski, B. A.; Szleifer, I., How and why nanoparticle's curvature regulates the apparent pKa of the coating ligands. *J. Am. Chem. Soc.* **2011,** *133* (7), 2192-7.

42. da Silva, A. G. M.; Rodrigues, T. S.; Haigh, S. J.; Camargo, P. H. C., Galvanic replacement reaction: recent developments for engineering metal nanostructures towards catalytic applications. *Chem. Commun.* **2017,** *53* (53), 7135-7148.

43. Au, L.; Lu, X.; Xia, Y., A Comparative Study of Galvanic Replacement Reactions Involving Ag Nanocubes and $AuCl_2^-$ or $AuCl_4^-$. *Adv. Mater.* **2008,** *20* (13), 2517-2522.

44. Yang, M.; Hood, Z. D.; Yang, X.; Chi, M.; Xia, Y., Facile synthesis of Ag@Au core-sheath nanowires with greatly improved stability against oxidation. *Chem. Commun.* **2017,** *53* (12), 1965-1968.

45. Korte, K. E.; Skrabalak, S. E.; Xia, Y., Rapid synthesis of silver nanowires through a CuCl- or CuCl2-mediated polyol process. *J. Mater. Chem.* **2008,** *18* (4), 437-441.

46. Ahn, J.; Wang, D.; Ding, Y.; Zhang, J.; Qin, D., Site-Selective Carving and Co-Deposition: Transformation of Ag Nanocubes into Concave Nanocrystals Encased by Au-Ag Alloy Frames. *ACS Nano* **2018,** *12* (1), 298-307.

47. Sun, X.; Yang, Y.; Zhang, Z.; Qin, D., Mechanistic Roles of Hydroxide in Controlling the Deposition of Gold on Colloidal Silver Nanocrystals. *Chem. Mater.* **2017,** *29* (9), 4014-4021.

48. Ricci, M.; Fortuni, B.; Vitale, R.; Zhang, Q.; Fujita, Y.; Toyouchi, S.; Lu, G.; Rocha, S.; Inose, T.; Uji-i, H., Gold-Etched Silver Nanowire Endoscopy: Toward a Widely Accessible Platform for Surface-Enhanced Raman Scattering-Based Analysis in Living Cells. *Anal. Chem.* **2021**, 93(12), 5037–5045

49. Harguindey, S.; Arranz, J. L.; Polo Orozco, J. D.; Rauch, C.; Fais, S.; Cardone, R. A.; Reshkin, S. J., Cariporide and other new and powerful NHE1 inhibitors as potentially selective anticancer drugs--an integral molecular/biochemical/metabolic/clinical approach after one hundred years of cancer research. *J. Transl. Med.* **2013,** *11* (1), 282.

50. Huang, Y.; Du, K. M.; Xue, Z. H.; Yan, H.; Li, D.; Liu, W.; Chen, Z.; Zhao, Q.; Tong, J. H.; Zhu, Y. S.; Chen, G. Q., Cobalt chloride and low oxygen tension trigger differentiation of acute myeloid leukemic cells: possible mediation of hypoxia-inducible factor-1alpha. *Leukemia* **2003,** *17* (11), 2065-73.

51. Hirsila, M.; Koivunen, P.; Xu, L.; Seeley, T.; Kivirikko, K. I.; Myllyharju, J., Effect of desferrioxamine and metals on the hydroxylases in the oxygen sensing pathway. *FASEB J.* **2005,** *19* (10), 1308-10.

52. Teti, G.; Focaroli, S.; Salvatore, V.; Mazzotti, E.; Ingra, L.; Mazzotti, A.; Falconi, M., The Hypoxia-Mimetic Agent Cobalt Chloride Differently Affects Human Mesenchymal Stem Cells in Their Chondrogenic Potential. *Stem Cells Int* **2018,** *2018*, 3237253.

53. Wang, P.; Li, L.; Zhang, Z.; Kan, Q.; Gao, F.; Chen, S. J. M. m. r., Time-dependent activity of Na^+/H^+ exchanger isoform 1 and homeostasis of intracellular pH in astrocytes exposed to $CoCl_2$ treatment. *Mol. Med. Rep.* **2016,** *13* (5), 4443-4450.

54. Wu, D.; Kraut, J. A., Role of NHE1 in the cellular dysfunction of acute metabolic acidosis. *Am. J. Nephrol.* **2014,** *40* (1), 36-42.

55. Raudenska, M.; Balvan, J.; Fojtu, M.; Gumulec, J.; Masarik, M., Unexpected therapeutic effects of cisplatin. *Metallomics* **2019,** *11* (7), 1182-1199.

56. Shirmanova, M. V.; Druzhkova, I. N.; Lukina, M. M.; Dudenkova, V. V.; Ignatova, N. I.; Snopova, L. B.; Shcheslavskiy, V. I.; Belousov, V. V.; Zagaynova, E. V., Chemotherapy with cisplatin: insights into intracellular pH and metabolic landscape of cancer cells in vitro and in vivo. *Sci Rep* **2017,** *7* (1), 8911.

57. Zheng, H.; Ni, D.; Yu, Z.; Liang, P.; Chen, H., Fabrication of flower-like silver nanostructures for rapid detection of caffeine using surface enhanced Raman spectroscopy. *Sens. Actuators B Chem.* **2016,** *231*, 423-430.

58. Hong, L.; Li, Q.; Lin, H.; Li, Y., Synthesis of flower-like silver nanoarchitectures at room temperature. *Mater. Res. Bull.* **2009,** *44* (6), 1201-1204.

59. Fortuni, B.; Inose, T.; Uezono, S.; Toyouchi, S.; Umemoto, K.; Sekine, S.; Fujita, Y.; Ricci, M.; Lu, G.; Masuhara, A.; Hutchison, J. A.; Latterini, L.; Uji-i. H., In situ synthesis of Au-shelled Ag nanoparticles on PDMS for flexible, long-life, and broad spectrum-sensitive SERS substrates. *Chem. Commun.* **2017,** *53* (82), 11298-11301.

60. Yang, Y.; Liu, J.; Fu, Z. W.; Qin, D., Galvanic replacement-free deposition of Au on Ag for core-shell nanocubes with enhanced chemical stability and SERS activity. *J. Am. Chem. Soc.* **2014,** *136* (23), 8153-6.

Summary and perspective

In summary, in this thesis, firstly, we investigated the correlation between the apparent pKa behavior of 4-MBA and the SERS intensity change of COO^- stretching mode upon pH change. We compared the pH response of the 4-MBA immobilized on AuAgNPs and AuAgNFs. Anisotropic AuAgNFs featured two equivalence points, while nearly spherical AuAgNPs showed one in their pH titrations. The pH value of one equivalence point for AuAgNFs agreed with the middle point of its SERS-based pH calibration, which was attributed to the SERS enhancement mainly from the edges of AuAgNFs. The pH-dependence of the COO^- stretching SERS peak consists of one broad component at low pH (1370 ~ 1380 cm-1) and an additional relatively sharp component at high pH (1420 cm^{-1}). We found that the SERS pH calibration curve from the peak around 1370 ~ 1380 cm^{-1} provided a higher sensitivity to pH change. Viability tests revealed that the Au coating on AgNFs drastically reduces their cytotoxicity, as well as their photocytotoxicity, while keeping high enhancement in SERS. Taking advantage of the high pH sensitivity obtained from 4-MBA-AuAgNFs, we have successfully performed pH sensing measurements inside endolysosomes of A549 cells. This result indicates the pH sensitivity of the SERS probe could be controlled by the regulation of the nanomaterials.

Secondly, applying this finding, an innovative SERS-based endoscopic technique is proposed for cytosolic and nuclear pH sensing. The endoscopic probe was constructed through fabricating Au by light-deposition on silver nanowires, following by modification with 4-mercaptobenzioc acid. (Au-dep AgNW) Au-dep AgNW showed higher pH accuracy than our previously reported Au-etched AgNW obtained via GRR. By inserting Au-dep AgNW in HeLa cells, the cytosolic and nuclear pH were successfully monitored over time. Therewith, the pH variation upon $CoCl_2$ and cisplatin treatments were monitored by this technique. The results obtained were consistent with previous studies and were additionally confirmed by fluorescence-based pH measurements, proving the accuracy and reliability of our technique. The results reveal that our endoscopic approach is a powerful strategy for a wide range of pH-sensing investigations.

Our results reported provide a method to design and optimize the SERS probe on-demand. And we provide a powerful strategy using this method for cytosolic and nuclear pH sensing, which would boost the study of a wide range of pH-sensing investigations. These findings would

boost the better development of the SERS probe, thus, contributing to a better understanding of biochemical events in single living cells.

Publications

Publications related to this dissertation:

[1] Q. Zhang, H. Wen, K. Watanabe, I. Kotani, M. Ricci, B. Fortuni, A.T.N. Dao, A. Masuhara, K. Hirai, H. Kasai, T. Inose, H. Uji-i, Low-Cytotoxic Gold-Coated Silver Nanoflowers for Intracellular pH Sensing, ACS Appl. Nano Mater., 3 (2020) 7643-7650.

[2] Q. Zhang, T. Inose, M. Ricci, J. Li, Y. Tian, H. Wen, S. Toyouchi, E. Fron, A.T.N. Dao, H. Kasai, S. Rocha, K. Hirai, B.Fortuni, H. Uji-i, Gold-Photodeposited Silver Nanowire Endoscopy for Cytosolic and Nuclear pH Sensing, ACS Appl. Nano Mater. (accepted）

Other publication:

[1] M. Ricci, B. Fortuni, R. Vitale, Q. Zhang, Y. Fujita, S. Toyouchi, G. Lu, S. Rocha, T. Inose, H. Uji-i, Gold-Etched SilverNanowire Endoscopy: Toward a Widely Accessible Platform for Surface-Enhanced Raman Scattering-Based Analysis in Living Cells, Anal. Chem., 93 (2021) 5037-5045.

Conferences

[1] 2019.9.18-21, The 80th Japan Society of Applied Physics (JSAP) Autumn Meeting. (oral)

[2] 2019.10.28-31, 32nd International Microprocesses and Nanotechnology Conference (MNC 2019). (poster)

[3] 2019.12.2-3, The 20th RIES-HOKUDAI International Symposium. (poster)

[4] 2019.12.2-3, 2019 International Symposium of Research Institute for Electronic Science (RIES), Hokkaido University & Center for Emergent Functional Matter Science (CEFMS), National Chiao Tung University. (poster)

[5] 2021.3.19-22, The 101st Chemical Society of Japan(CSJ) Annual Meeting. (oral)